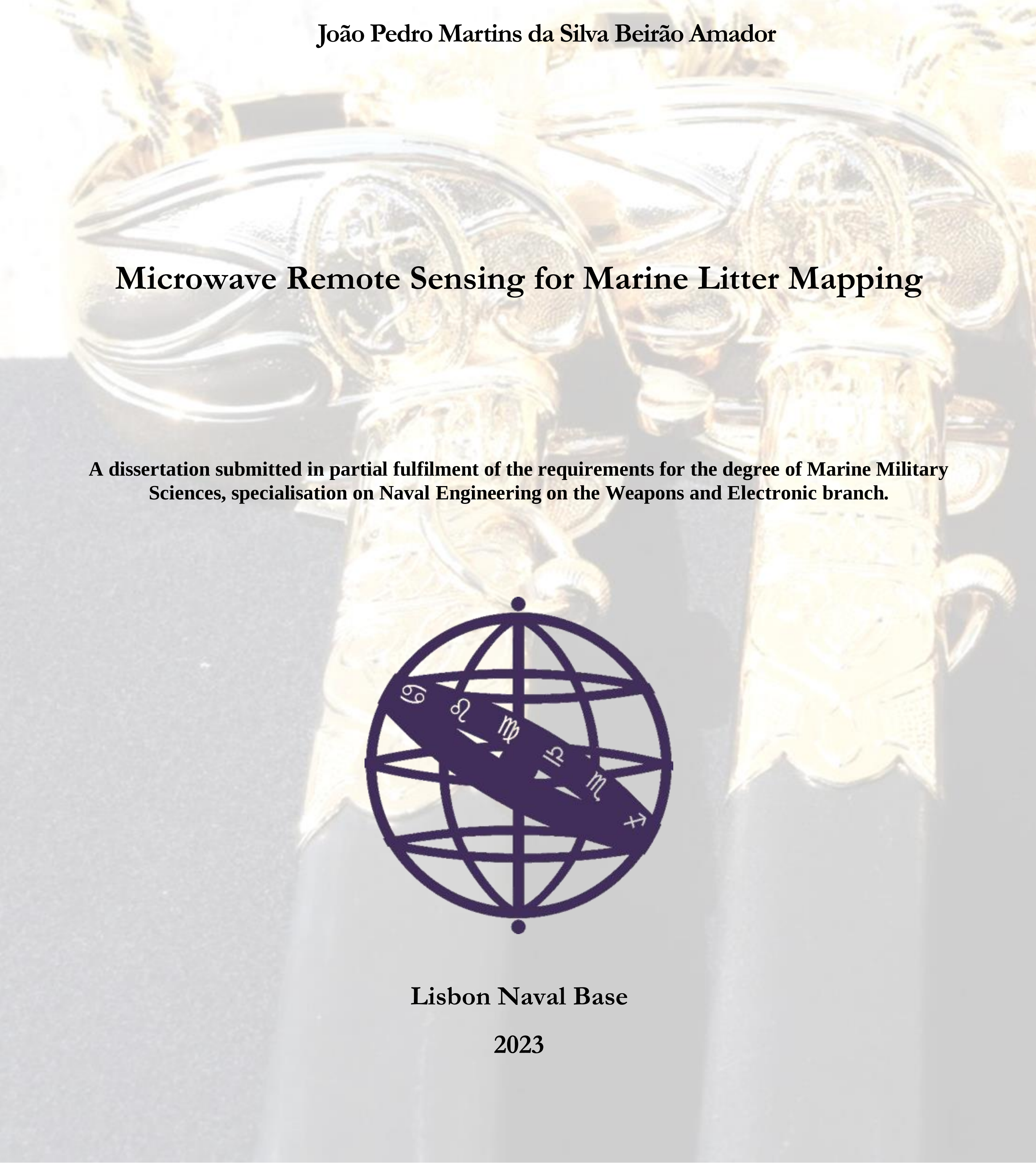

ESCOLA NAVAL

talant de bien faire

João Pedro Martins da Silva Beirão Amador

# Microwave Remote Sensing for Marine Litter Mapping

**A dissertation submitted in partial fulfilment of the requirements for the degree of Marine Military Sciences, specialisation on Naval Engineering on the Weapons and Electronic branch.**

Lisbon Naval Base

2023

ESCOLA NAVAL
talant de bien faire

**João Pedro Martins da Silva Beirão Amador**

# *Microwave Remote Sensing for Marine Litter Mapping*

A dissertation submitted in partial fulfilment of the requirements for the degree of Marine Military Sciences, specialisation on Naval Engineering on the Weapons and Electronic branch.

Supervisor: João Manuel de Almeida Monteiro Felício
Co-Supervisors: Carlos António Cardoso Fernandes and Sérgio de Almeida Matos

Examination Committee
Chairperson: Prof. Bruno Damas
Supervisor: Prof. João Felício
Member of the Committee: Prof. Paulo Marques

**The Master's Student**

Assinado por: **João Pedro Martins da Silva Beirão Amador**
Num. de Identificação: 30235785
Data: 2023.08.27 10:30:34 +0100

**João Beirão Amador**

**The Supervisor**

Assinado por : **João Manuel de Almeida Monteiro Felício**
Num. de Identificação: 13726816

**João Monteiro Felício**

**Lisbon Naval Base**
**2023**

*If we were logical, the future would be bleak, indeed.*
*But we are more than logical. We are human beings, and we*
*have faith, and we have hope, and we can work.*

Jacques Yves Cousteau

# ACKNOWLEDGMENTS

This work was promoted and supported by Instituto de Telecomunicações (IT), under the project “MARES” 2021/2023, coordinated by professor Carlos António Cardoso Fernandes. IT provided the tools needed, including the computational and laboratory resources. I would, in first place, express my gratitude to my supervisors professors João Felicio, Carlos Fernandes and Sérgio Matos, who guided me along the stages of this thesis, with advice and insightful knowledge. Also, a special thanks to my college Tomás Soares da Costa, PhD student on IT, who never refused to give me a hand; and to my navy friend and counterpart Bon de Sousa for sharing his oceanographic knowledge with me.

I find the area of wireless energy propagation fascinating; therefore, it was a pleasure to finalize my degree with a dissertation regarding this theme.

To my family, I own the greatest appreciation, to my grandparents Avô Beto, Avó Mimi and Avó Teté, my father Papá Tó and mother, Mamã Isa. Also, my gorgeous girlfriend Catarina who believed in my value as a person and fulfilled the void in my soul.

# RESUMO

Anualmente toneladas de macro plásticos entram no ambiente marinho ameaçando o bem-estar das espécies no oceano. A remoção deste plástico é uma prioridade máxima, e a sua deteção antecipada é um fator determinante para a sua mitigação e limpeza. O oceano é todavia muito vasto e apenas através de satélites poderá o lixo ser identificado globalmente num curto período temporal. Recentemente surgem estudos sobre tecnologias de micro-ondas que ainda assim carecem de pesquisa em muitos aspetos. Este estudo pretende melhorar a deteção de lixo marinho utilizando técnicas de Radar, especialmente na banda X, a qual apresenta os melhores resultados de deteção. Foram analisadas medidas geradas numericamente bem como medidas experimentais para detetar lixo em várias condições, tais como sobre a influência do efeito de Bragg. Para alem disso foram analisadas várias concentrações e sub-bandas de frequência, indicando que mesmo nas condições para o efeito de Bragg é possível detetar o lixo. O estudo também recorre a antenas multipolarizadas para detetar lixo. Em termos de polarimetria, a análise de Pauli é conclusiva para o número de reflexões que os raios refletidos sofrem.

**Termos Índice:** Decomposição de Pauli, Efeito de Bragg, Lixo marinho, Macro plásticos, Observação remota, polarimetria micro-ondas, Poluição, Reflexões micro-ondas.

# ABSTRACT

Each year tons of macro plastics enter the marine environment menacing the wellbeing of ocean’s species. The removal of these plastics is a top priority, and its early detection is a key factor for its mitigation and cleaning. The ocean is however very vast, and only trough satellites can the litter be globally identified in a short time. Studies are recently surging regarding microwave technology; however, in many aspects still lack research. This study intent is to improve marine litter detection regarding Radar techniques mainly in the X-band, which enhanced detection. Numerically generated measurements and experimental measurements are analysed to detect litter under various conditions such as under the influence of Bragg effect. Also, different concentrations and frequency sub-bands are examined which indicate that litter is still detectable even under Bragg’s conditions. The study also uses multi-polarised antennas to detect litter. Regarding polarimetry, the Pauli analysis is conclusive on the backscattered ray bounce number.

**Index Terms:** Bragg effect, Macro plastics, Marine litter, Microwave backscattering, Microwave polarimetry, Pauli decomposition, Pollution, Remote sensing

# CONTENTS

# LIST OF TABLES

# LIST OF FIGURES

# ACRONYMS

| | | |
|---|---|---|
| 3D | Three dimensional | 7,12,23,24 |
| BSA | Bistatic Backscatter Alignment | 19,20,21,48 |
| CDF | Cumulative distribution function | 22,57,58,59 |
| CST | Computer Simulation Technology | 23,25,26,28,61 |
| ESA | European Space Agency | 6,7,10 |
| HH | Horizontal-Horizontal Polarisation | 19,24,48,49,51,52,53 |
| HV | Horizontal-Vertical Polarisation | 19,24,48,49,51,52,53 |
| InSAR | Interferometric Synthetic Aperture Radar | 9 |
| JPSEmbed | Joint Plastic Spectral Embedding | 7 |
| LIDAR | Light Detection and Ranging | 7,8 |
| NASA | National Aeronautics and Space Administration | 10 |
| PDF | Probability density function | 22,57,58,59 |
| PE | Polyethylene | 48,49,50,51,52,53, 54,55,56,57,58,59 |
| PEC | Perfect Electric Conductor | 25,26,27 |
| PolSAR | Polarimetric Synthetic Aperture Radar | 8,9 |
| PRISMA | (PRecursore IperSpettrale della Missione Applicativa) | 7 |
| Radar | Radio Detecting and Ranging | 5,8,9,10 |
| RGB | Red-Green-Blue | 20,21,52,53,54,56,57 |
| SAR | Synthetic Aperture Radar | 8,9,10,36,61 |
| SNR | Signal to Noise Ratio | 17 |
| VH | Vertical-Horizontal Polarisation | 19,24,48,49,51,52,53 |
| VV | Vertical-Vertical Polarisation | 19,24,48,49,51,52 |

# 1. INTRODUCTION

## 1.1. MOTIVATION

Environmental awareness has recently increased in every sector of our society. From international organizations to national governments, from local communities to individual households, environment awareness is an important topic that is on everyone’s mind.

Today, the environment is being constantly harmed by industries, such as the fossil fuel industry that produces energy, animal farming and waste management, just to name a few. And a major part of the problem is Plastic: Although a versatile material which was revolutionary to the industry, not only its production has a significant environment impact, but their disposal, when not made correctly, has a devastating impact on the planet, an impact that led to the death of several species. On a global scale, only 9% of plastic waste is recycled and 22% is mismanaged, OECD countries are responsible by 14% of overall plastic leakage which 11% are microplastics and 35% microplastics. With the COVID-19 pandemic, the plastic use dropped 2.2%, however its consumption resumed in 2021. (Organisation for Economic Co-operation and Development, 2022) (OECD iLibrary, 2023)

Fortunately, every sector of the society is making an effort to fight back plastic pollution and improve waste management. Correct disposal of plastic residues has an enormous impact on marine environments. All sectors are responsible for correct garbage disposal, and when done improperly, it is their responsibility to remove them from the environment. Such responsibility involves the social sector, the government, the economic and industrial sectors, and the technological sector. When garbage is introduced in the sea, a country’s navy may have a key role on its recover, detection, and monitoring.

When contaminated, sea cleaning must be a top priority as the implications are always disastrous. Every year, millions of tons of plastic garbage enter the sea from a variety of sources, poisoning the sea waters and its creatures, contributing to a faster planet degradation and live degeneration. In 2019, the world produced 368 million tonnes of plastic garbage, 57.9 million tonnes produced in Europe alone (PlasticsEurope, 2020).

Within 2016, 19 to 23 million metric tons of plastic litter entered in the sea, leading to an estimation that, if the current trend does not suffer an alteration, by 2030, plastic emissions will rise around 53 million metric tons per year (Borrelle, et al., 2020). Another study showed thar if humans do not change their ecologic behaviour, it is predicted that by 2050 the plastic weight in the ocean will be greater than all living beings weight combined (Tekman, Walther, Peter, Gutow, & Bergmann, 2022). According to the World Economic Forum, takes about 141 billion pounds each year so that humanity can protect the oceans correctly, however between 2015 and 2019, the amount invested on this matter did not reach the 10 billion pounds (Boyle, 2023)

Plastic waste in the ocean emerges from various sources. The main root of oceanic pollution is litter from land carried by rivers and streams into the ocean, contributing 70% to 80% of the ocean plastic litter. Waste generated by ships and offshore platforms and waste from aquaculture and mariculture operations, provides 20% to 30% of ocean plastic contamination, such as fishing nets, lines, ropes, and abandoned vessels (Ritchie, 2021).The problem of plastic pollution in the ocean is global, as every country contributes to ocean plastic litter spread. Each year is estimated that 4.8 to 12 million metric tons of land-based plastic enter the oceans (Jambeck, 2015) and therefore efforts are made to develop technology aiming for plastic detection at the ocean. Figure 1 is a representation of the world with the amount of plastic released into the ocean in 2019 (Meijer, Emmerik, Der Ent, Schmidt, & Lebreton, 2021).

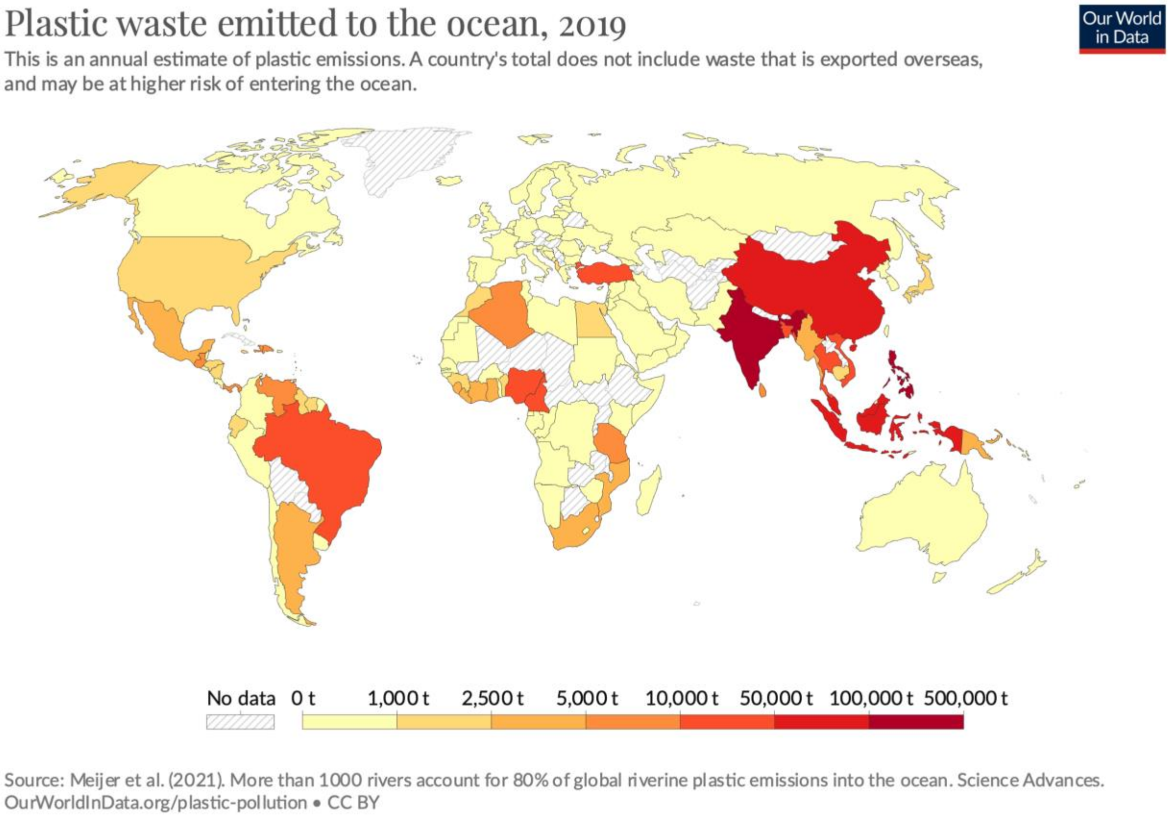
Plastic waste emitted to the ocean, 2019

This is an annual estimate of plastic emissions. A country's total does not include waste that is exported overseas, and may be at higher risk of entering the ocean.

Source: Meijer et al. (2021). More than 1000 rivers account for 80% of global riverine plastic emissions into the ocean. Science Advances.
OurWorldInData.org/plastic-pollution • CC BY

Figure 1 - Plastic waste emitted to the ocean, 2019. Taken from (Meijer, Emmerik, Der Ent, Schmidt, & Lebreton, 2021)

As plastic suffers degradation while on the ocean, microplastics are detached from the main body. Those components easily enter the food chain leading to a lower life expectancy and quality of life degeneration as humans consume seafoods that have already been infected with synthetic materials. Microplastic particles were found in human food as fish, shellfish, sea salt, bear, and honey (Gamarro, Ryder, Elvevoll, & Olsen, 2020).

Plastic ingestion is not the only cause of animal death as it just counts for 5% of the sea animals' death. The most common cause of death from plastic debris are suffocation, and entanglement. From all the causes of death by plastic pollution, entanglement is responsible for 80% of delayed deaths as an entangled animal might see its ability to escape from predators significantly reduced. Additionally, plastic entanglement can prevent breastfeeding in mammals risking the wellbeing of its offspring (Werner, et al., 2016). Another noteworthy impact of plastic concerns animals such as loggerhead sea turtles, which mistake plastic bags with jellies that make part of their food; albatrosses mistake plastic resin pellets with fish eggs which they catch to feed their offspring's; and as referred before, marine mammals can get entangled and prevented to feed their progenies (NOAA, 2023).

Another issue that has been concerning experts, is the plastic accumulation on some Earth locations due to significant ocean currents named gyres. These currents are formed by several factors such as wind, sea water temperature, salinity and by the physical influence of Earth tides. From a great number of oceanic gyres, most of them not even identified, five blazing litter motion on the sea. Those are the North Atlantic Gyre, the South Atlantic Gyre, the South Pacific Gyre, the Indian Ocean Gyre, and the North Pacific Gyre, being the latest the one which has most influence on plastic cumulation. The North Pacific Gyre is responsible for the accumulation of tons of plastic objects, mostly microplastics[1] covering 20 million square kilometres of sea surface (Evers, 2023). The Pacific Gyre is formed by four clockwise-rotating currents, including the California current, North Equatorial current, Kuroshio current, and North Pacific current. The accumulation sight is known as The Great Pacific Garbage Patch, the biggest garbage patch identified until now (Cassidy, 2021). The Pacific Patch is surrounded by the North Pacific Subtropical Gyre, between California and Hawaii, which is also referred to as another vortex of plastic waste, leading to more plastic accumulation on that place. The 79.000 tons of plastic litter swirling, contributes for a vast environment of floating pieces covering the ocean's surface, twice the size of Texas, where creatures live in (Boyle, 2023). A study shows the rise of costal species' communities mostly composed by organisms with direct development or asexual reproduction, which makes possible for a long-term sustainable persistence on rafts. This event largely contributes for an alteration of ocean's ecosystems, which can lead for the species distribution and for biogeography alterations (Haram, et al., 2023).

---

[1] A plastic object is considered a microplastic if it sizes less than five millimetres (National Oceanic and Atmosferic Administration, 2023).

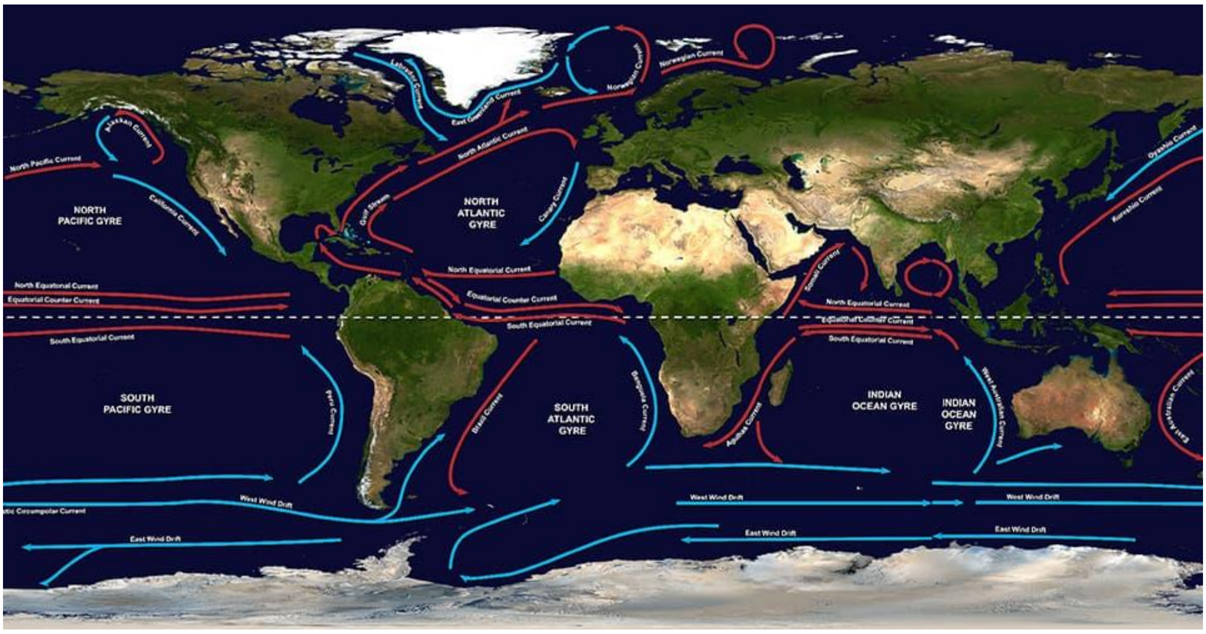

Figure 2 - The major gyres on the planet (National Oceanic and Atmospheric Administration, 2023)

As discussed before, gyres motion led to plastic accumulation in some areas on Earth, and most of those locations are remote and of difficult access. It is crucial to keep researching for new remote sensing techniques, that can track and detect plastic waste from a distance without on-sight human intervention. It is also necessary to ensure permanent surveillance, therefore these processes should not be dependent on atmospheric conditions nor on daylight and need to be robust to the changing colours and sizes of plastic waste, as it interacts over time with marine life, which make the detection more challenging and irregular. In Figure 2 is a map from (National Oceanic and Atmospheric Administration, 2023) identifying the most relevant gyres around the globe.

This environmental problem calls for a concerted effort from every country's government, industry sector, and individual citizen. Starting by reducing plastic production and improving its disposal, as well rethink existing recycling strategies, and improve waste management. It is important to leverage advances in technology to address current environmental problems to prevent an inhospitable planet. In terms of technology, this calls for global mapping solutions to address the accumulation of plastic waste. Without a clear existing solution, this highlights the need for investment on the research for alternative approaches, such as the potential use of space-based technologies (Martínez-Vicente, et al., 2019). The space industry could offer new opportunities for monitoring plastic pollution from a distance.

This thesis will focus on some methods to identify the floating plastic litter, something that hopefully will turn out to be useful to the Portuguese Navy and Portugal's maritime Authority, Autoridade Marítima Nacional[2]. Future plastic recovery missions will aim to keep

---

[2] The Portuguese department for sea pollution control, Direção de Combate à Poluição do Mar, is a department in the Portuguese Navy created to prevent and control the sea pollution on the Portuguese

the Portuguese coast clean and the ocean fields away from pollution disasters. It is of major importance to protect all beings that live on the vast Portuguese coast, all industries which have the sea as their main resource, and the population that live by the ocean, eat its food and enjoy its beauty. This work will explore and study the enhancement of possible path for a new alternative solution for litter detection through the exploration of satellite capabilities using active microwave sensing techniques.

## 1.2. STATE OF ART

Remote sensing is a technology capable of collecting information of a certain object, or phenomenon occurring on a geographic area from a distance, without physical contact. The use of remote sensing contributes to a large number of applications including agriculture, forestry, environmental monitoring, climate, science, disaster response, resource management, and military surveillance (Woodhouse, 2006). This might be applied to a great number of platforms and places, however, for sea litter surveillance application, the sensors are usually installed on drones, aircrafts, or satellites because, generally, having the sensors installed on platforms working on high altitudes allow an observation of a larger area, known as the sensor footprint. The collected data might take from many formats, depending on the installed sensor. Therefore, techniques for remote sensing are very dependent on which band of the electromagnetic spectrum is being used and based on the objective of the system.

As this thesis is focusing on oceanic environmental concerns and it will study a technological approach to eventually build a more sophisticated solution, this chapter will cover the main remote sensing techniques, the currently developed work on this field, and the latest works being held at the time of writing which are related to the matter. Some relevant techniques used on marine remote sensing include Optical Remote Sensing, remote sensing through Radar (Radio Detecting and Ranging), LiDAR (Light Detection and Ranging) and Multispectral and Hyperspectral Remote Sensing. Each of the following topics of this Section 1.2 is dedicated to one of the previous referred technologies, where those advantages and disadvantages will be discussed.

### 1.2.1. OPTICAL AND INFRARED REMOTE SENSING

Optical remote sensing uses visible and infrared radiation to capture images of the Earth's surface, detecting the electromagnetic radiation reflected or emitted by the Earth's surface and atmosphere. Optical sensors, mounted on airborne platforms as aircraft or satellites, are suitable not only for environmental monitoring, but also other applications as natural resource management and agriculture to monitor vegetation growth and health (HALL, LAMB, HOLZAPFEL, & LOUIS, 2002), urban planning (Shi, Goodchild, Batty, Kwan, & Zhang, 2021), and disaster response (Eguchi, Huyck, Ghosh, & Adams, 2008).

---

jurisdiction zone. The department was establish the necessary technical procedures to survey and control sea pollution (Autoridade Marítima Nacional, 2023).

From the several types of optical sensors used in remote sensing, multispectral sensors can capture images in several specific wavelength bands and, hyperspectral sensors are capable of capturing images in many narrow and contiguous wavelength bands while panchromatic images use a single band usually resulting on grey scale images. Panchromatic sensors can capture high-resolution grayscale images across a broad range of wavelengths (Dalponte, Bruzzone, & Gianelle, 2012). However, those techniques are going to be addressed on a distinct section as they have significant differences from the conventional optical remote sensing methods.

Optical remote sensing is clearly superior in terms of resolution, allowing to capture of high-resolution and high-quality images. However, optical remote sensing is limited by cloud cover and atmospheric conditions, which will reduce the image quality significantly under those conditions. Furthermore, optical remote sensing does not work during night-time or sees it capacity very limited as the sensing requires a light source, which is usually the sunlight during the day for airborne sensors. The optical sensors are also sensible to the sun orientation angle which makes data acquisition during the day more inconsistent, leading to a complex post processing and data interpretation. Furthermore, certain types of materials have a less sensitive response, such as bare soil or rocks, which can make it difficult to distinguish between different land cover types with similar optical back responses.

Satellites such as the European Space Agency (ESA) Copernicus Sentinel deliver optical data image with a 10 meter resolution, enabling the detection of plastic on water surface while the limitations of optical remote sensing are met (Biermann, Clewley, Martinez-Vicente, & Topouzelis, 2020). WorldView-2, a commercial high-resolution satellite operated by Digital Globe, which has a multispectral sensor that can capture images with a spatial resolution of up to 0.5 meters, is well-suited for detecting small objects such as marine litter. Also, Planet, a private American Earth-imaging company that operates the largest constellation of Earth-observing satellites providing daily, global imaging of the Earth's surface at a high resolution, is essential for collecting optical information useful for sea sensing (Topouzelis, Papageorgiou, Suaria, & Aliani, 2021). Moreover, Unmanned Aerial Vehicles (UAVs) equipped with cameras, sensors, and other imaging devices have great potential for oceanic litter optical sensing, involving the use of sensors and cameras to detect and monitor litter in water and along beaches or shoreline as a rapid and cost-effective mean of collecting high-resolution imagery and data of litter from remote and hard-to-reach areas that are difficult or dangerous to access (Topouzelis, Papageorgiou, Suaria, & Aliani, 2021), (Topouzelis, Papageorgiou, Karagaitanakis, Papakonstantinou, & Ballesteros, 2020).

Besides the conventional optical sensing, Multispectral, Hyperspectral and Panchromatic remote sensing make use of antennas to capture scattered or emitted radiation from the Earth's surface across a specific range of wavelengths. These technologies differ on the bands of the electromagnetic spectrum which their sensors use. Panchromatic remote sensing allows the creation of images by observing only one band. The image is usually on greyscale with the pixel colour related to the radiation intensity backscattered from sunlight. A panchromatic image could be similarly interpreted as a black-and-white aerial photograph of the sensor’s footprint area. The recent launched[3] PRecursore IperSpettrale della Missione Applicativa (PRISMA) hyperspectral satellites, from ESA (ESA, 2012) together with Machine Learning algorithms can be a possible path to detect marine litter, however this method needs further improvement and search (Taggio, et al., 2022). Multispectral sensors can detect litter on the sea surface with a great amount of detail as the images are sourced in several spectral bands, usually between 3 and 10 wavebands which are selected depending on the material properties of the observed object and surrounding environment. Hyperspectral remote sensing might be seen as a more complex version of Multispectral sensors, providing information on a larger number of wavebands, typically from 100 to 200, more suitable to detect microplastics (ESA, 2020). The ESA project Detection of Ocean Plastics with Hyper-to-multispectral infrared neural networks aims on effectively mitigate marine litter damage, accurate mapping of ocean borne plastics across the globe. The measurements performed by satellite systems are a great aid under needs to survey remote locations where humans cannot reach by foot and where line of sight observation from earth is far from possible. As current multispectral sensors have limited capability to detect plastic, it is pioneer to improve their capacity through the development of a novel neural network called Joint Plastic Spectral Embedding (JPSEmbed). Testing with simulated and real Sentinel-2 data shows that JPSEmbed detects land-based plastics significantly better than traditional methods and has the potential to detect plastic concentration with a 20% error margin. The approach can be expanded to other sensor types for more widespread coverage and global plastic detection and concentration maps (ESA, 2020). These techniques can be mounted on aerial platforms as airplanes, drones, or satellites. The satellites from PRISMA, a program of the Italian Space Agency, develop hyperspectral imaging and data processing, leading to some studies are based their data, enabling the capacity of plastic litter detection on the marine environment (Kremezi, et al., 2022).

The sensors later addressed on this section are more expensive than traditional optical sensors referred beforehand, furthermore more complex computational tools are also required for processing the acquired data with Machine Learning algorithms. As we saw previously on conventional optical methods, multispectral, hyperspectral, and panchromatic technology are also affected by weather conditions, such as cloud cover or rough seas, having a great impact on the usability of the data collected the same way as the conventional optical systems. As these sensors do not have their own source of light, they are dependent on the sunlight making it impossible to operate during all the 24 hours of the day.

### 1.2.1. LIGHT DETECTION AND RANGING

Light Detection and Ranging (LIDAR) principle is to measure distance with an active source of laser light, which allows the creation of three-dimensional (3D) images by measuring the time delay between the laser emission instant and the scattered light receiving instant. LIDAR sensors can only, however, cover a few kilometres which makes this technology not suitable for satellite installation. Also, LIDAR can only measure distances on its antennas line of sight. Alike optical remote sensing, LIDAR systems are vulnerable to weather conditions

---

[3] PRISMA is a medium-resolution hyperspectral imaging satellite launched on 22 March 2019, developed by Agenzia Spaziale Italiana.

and when affected the information might appear disrupted or scattered by events as fog, rain, or snow, sometimes disrupting the correct procedure of collecting the data. On the other hand, as LIDAR sensors request active devices as the system produces its own laser light, they can operate in the dark.

In 2016 a report was published stating that through LIDAR sensing, would be possible to identify and classify the type of litter on beaches into plastic, paper, cloth, or metal. The tests were carried out on the beach of Beihai in Guangxi province, China, but just under fair weather (Ge, Shi, Mei, Dai, & Li, 2016). A more recent study carried out in a laboratory refers the capability of LIDAR detecting plastic submerged on the water. The results showed the capacity of detecting fluorescence features of several types of plastics and distinguish plastic from other sorts of marine debris (Palombi & Raimondi, 2022).

### 1.2.2. RADAR IMAGING TECHNIQUES

Radar is the latest remote sensing technique being presented on this chapter which underlying principle is to transmit an electromagnetic wave from an antenna that backscatters on a surface to either the same antenna or to a separate antenna, depending on the radar configuration. By measuring the time interval between the transmitted and received signals, or its phase variation, it is possible to calculate the distance to the object, speed, direction, and shape depending on the system characteristics (Richards, Scheer, & Holm, 2010). On marine litter remote sensing, is important to cover large areas of the ocean and for this reason, the most suitable platforms to install the antennas are space crafts and aircrafts, which allow a greater antenna footprint and by consequence, more area of sea is being surveyed. In these section two aspects are going to be addressed due to their relevance on the field of remote sensing imaging techniques. First polarimetry techniques and then Synthetic Aperture Radar (SAR) technology. Will also be addressed Polarimetric SAR (PolSAR), which is a technique that combines both SAR and Polarimetric methods.

Polarization is an important field of radar imaging techniques allowing the exploration of the hidden object’s scattering properties which, when combined with SAR techniques lead to PolSAR systems. Polarization, as a characteristic of the electric flux lines orientation in an electromagnetic field, suffer most of the times, alterations when backscattered from complex surfaces. Those alterations are different depending on the object shape, orientation, and material characteristics. For this reason, analysing different polarizations or more than one combined on the receiver antenna might lead to new conclusions and contribute for the object characterization. The study of polarization has many remote sensing applications, especially when one of the objectives is processing the backscatter to create polarimetric images (Boerner, 2004). Polarimetric scattering can be measured with other techniques besides SAR, as those saw on previous sections, such as a simple antenna or optical sensor capable to transmit and receive polarized energy, depending on the antenna characteristics, measuring the polarization properties (Hajnsek & Desnos, 2021). Polarimetry is used on weather meteorological radars, where polarimetry allows more precise forecasts and identification of severe conditions, important to early warn communities in affected areas from possible disasters as tornadoes or thunderstorms. Polarimetry can also enhance airborne remote sensing performance, as it allows to distinguish Earth surface materials with a similar shape, an important task both on land and on the sea. Activities as agriculture, urban planning, military surveillance, and oil detection on sea surface take advantage of this based on different scattering properties of the materials (Boerner, 2004) (Kampes, 2006).

Most spaceborne and airborne applications aim to create images of the land to describe the presence of a specific material. There are artificial mechanisms to cover a bigger area of land just by adding computational processing complexity without the need for bigger antennas. Radar imaging is the process of creating those images. Polarimetry techniques combined with Synthetic Aperture Radar (SAR) techniques lead to Interferometric Synthetic Aperture Radar (InSAR), and PolSAR, which are some of the radar imaging methods that enhance the physical antennas limitations. SAR utilizes a single antenna mounted on a moving aircraft to transmit and receive signals, producing high resolution images across the flight direction. InSAR uses two antennas to measure the phase difference between signals; this way it is also possible to measure the altitude variations through more computational efforts. Polarimetric Synthetic Aperture Radar (PolSAR) makes use of polarized signals to obtain information on the scattering properties of objects due to the distinct backscatter response of certain materials after receiving the same emitted energy waves. As SAR systems uses active antennas is possible to create high-resolution images of the Earth's without daylight and since it’s a microwave frequency band, weather conditions do not create a significant effect on the operation. Careful selection of the frequencies of observation can also help to minimize atmospheric interference, making it possible for Earth-orbiting satellites to achieve continuous surface coverage. The backscatter is recorded and processed to create an image which requires complex algorithms which uses the time delay and phase differences between the transmitted and received microwave signals to construct an image by combining multiple samples from slightly different angles, creating a synthetic aperture much larger than the physical antenna of the radar, allowing very high-resolution observation of the Earth's surface even on locations which are not visible to other remote sensing technologies ( Lopez-Sanchez & Fortuny-Guasch, 2000).

Is also important not to forget SAR downsides. SAR systems are not able to differentiate small marine objects easily (e.g., differentiate plastic from organic matter), and that is something worth working as SAR is mandatory, for litter remote detection, to have a sensitive enough system to detect smaller items. SAR resolution is especially poor when analysing crossed range information lacking the necessary detail to accurately identify and locate the objects such as floating plastic bottles. As referred before, PolSAR adds more complexity to its original predecessor, providing the same data but making possible to analyse through different polarimetric configurations, allowing airborne radars the acquisition of more detailed information about the Earth's surface unlike traditional SAR, which uses a single polarization state (either vertical or horizontal) (Hajnsek & Desnos, 2021). However, PolSAR calls for at least twice the power of an average SAR system resulting in higher energy consumption and increased operational costs due to the diversity of polarized waves and the swath width of the sensor might be halved, which can reduce the area that can be covered by a single scan. Besides if a dual-pol antenna is being used, there is a significant increment of complexity as phase differences are introduced due to the shift of polarization states both on the transmitter and on the receiver (Hajnsek & Desnos, 2021).

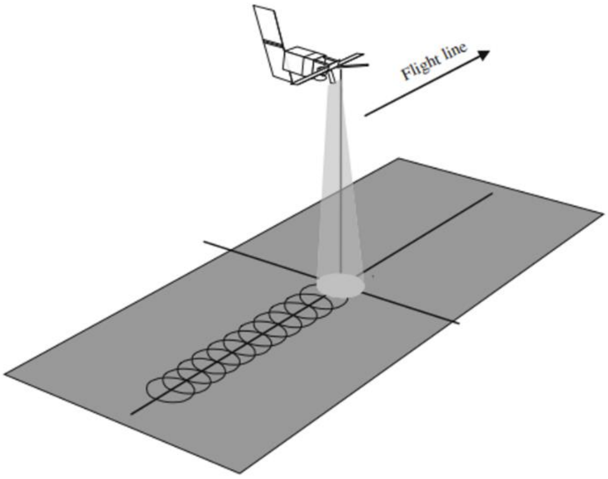

Figure 3 - Synthetic Aperture Radar (Woodhouse, 2006)[4]

SAR systems take a great role on oil spill detection due to the huge difference on characteristics between oil and sea water (Chaturvedi, Banerjee, & Lele, 2019), however, as stated before, SAR is not the most suitable method to detect small objects with little noticeable scattering characteristics such as plastic litter floating above the ocean.

### 1.2.3. RECENT DEVELOPMENTS ON MARINE LITTER REMOTE SENSING

As mentioned earlier, the primary focus of plastic remote sensing research is to identify litter in the ocean. The preceding sections will explore the various technologies that facilitate plastic detection already developed or under research, therefore delve into the most significant studies and projects that have been published thus far.

On the space research from western countries, both National Aeronautics and Space Administration (NASA) and ESA are currently pursuing solutions for oceanic plastic litter detection through remote sensing, so they can explore furthermore its satellites capacities. At the University of Michigan, a novelty method for mapping microplastics present in the ocean with the aid of satellite data was published. The project collect data from eight microsatellites that are part of NASA’s Cyclone Global Navigation Satellite System mission (National Aeronautics and Space Administration, 2019) (Sun, Bakker, Ruf, & Pan, 2023). It is believed that these satellites on constellation are able to measure the presence of microplastics and surfactants when compared to the roughness of the sea differences over time, accounting the wind influence and map litter concentration throughout the seas. The microplastics dataset has been published at NASA’s Physical Oceanography Distributed Active Archive Centre (Earth Data, NASA, 2021) (Cassidy, 2021). In addition to gyres being recognized as the reason for plastic build-up in isolated regions of the planet, there exist other natural occurrences that complicate the task of remote sensing of human-generated plastic waste. Another recent study

---

[4] Adapted

suggests that the presence of microplastics and surfactants in seawater has a considerable impact on wave generation suppression. Also reduce the impact caused by the wind stress on the surface tension exponentially (Sun, Bakker, Ruf, & Pan, 2023). Since nano-plastic is a source of oceanic pollution, it is valuable to undertake future experiments to gauge their influence on wave damping for remote sensing purposes. Spaceborne bistatic radar measurements is also believed to be a possible answer for measurements of the ocean allowing the detecting and imaging the global distribution of ocean microplastics. The method analyses the ocean surface roughness acquired by the radars, relying on an assumed reduction in responsiveness due to wind-driven roughening caused by surfactants acting as tracers for microplastics near the surface ( Evans & Ruf, 2022).

Prior to this thesis, several groups, including “MARES”, conducted experiments at the DELTARES wave facility in Delft (Delft, 2022). A report from researchers from the Universitat Politècnica de Catalunya is also trying to prove that the use of land navigation satellites might be a possible solution to track sea litter. They conducted their tests on Delft (Delft, 2022). The setup recreates various scenarios that simulate the Global Navigation Satellite Systems reflectometry emissions to a water flume with sinusoidal and JONSWAP spectrum waves with significant wave heights, types of plastics, and marine litter. Some conclusions point that the standard deviation of the estimated reflectivity increases slightly in the presence of capillary waves, and in general it increases furthermore in the presence of litter. On the statistical field of data analysis, according to the study, the standard deviation of the phase suffers some variations, and measures of Skewness and Kurtosis in the field of statistics showed, also, significant variation (Gonga, et al., 2023). Another worth to name group, which also conducted its experiments at Deltares, researched a about the influence of plastic components presents on the water surface. The study tests their antennas on C-band and X-band, comparing both frequency bands and determining which are the minimum quantities which are necessary to the plastic detection. Conclusions point that X-band frequencies outperformed the C-band frequencies, X-band detecting significant differences in backscattering in 37 cases, whereas C-band detected differences in only 10, both under a set of the same 60 cases. Is also possible to affirm that differences in backscattering from litter cases and non-litter cases were dependent on the size and shape of the plastic object, as well as water waves conditions under which the test was being conducted (Simpson, et al., 2023).

“MARES” had also published an article in the 17th European Conference on Antennas and Propagation, 2023. The article results from the campaigns in Deltares and measurements in IT to evaluate the microwave response of floating (Costa T. S., et al., 2023).

## 1.3. OBJECTIVES

The objective of this thesis is to further explore the feasibility of detecting plastic waste floating on the water's surface using microwave technology. This research is being conducted as part of the “MARES” project by IT, “MARES” 2021/2023 and builds upon a previously written master’s degree thesis (Figueira, 2021) and articles (Felício, et al., 2023) (Costa T. S., et al., 2023) (Costa T. S., Felício, Matos, & Fernandes, 2023). Therefore, this thesis will investigate alternative methods, newer setups and novelty situations to enhance the detection of plastic litter in the ocean. The work developed during the thesis aims to answer if it is still possible to detect litter under simulations of exquisite effects, as the Bragg effect, and in larger areas and using different antennas' combinations and polarimetry enhance litter detection.

## 1.4. THESIS STRUCTURE

To address the points previously referred on Section 1.3, during this thesis will be studied different subjects regarding the theme of remote sensing. During the work, both simulation environments, such as Computer Aided Design models created through a 3D simulating software (Dassault Systèmes, 2002 - 2023), and real live scenarios, where the data was collected on a facility from the research centre of Deltares (Delft, 2022) were analysed.

The following thesis is structured into five chapters. After the introduction on Chapter 1, Chapter 2 gives a theoretical context of the problem, foreseeing the analytical framework required to comprehend the outcomes. Chapter 3 analyses and discusses the results obtained with the analytic methods and outlined in the previous chapter. Chapter 4 is dedicated to the experimental setup, analysing, and discussing its results similarly to what was done previously on Chapter 4. Finally, Chapter 5 provides conclusions and recommendations for future work.

# 2. FORMULATION AND METHODS

This chapter aims in describing the theoretical framework and necessary metrics for the understanding of the followed path along the thesis.

First in this chapter is Section 2.1, where the wave generation mechanism is explored. Next, in Section 2.2, the Bragg effect is introduced. In Section 2.3, a walkthrough the inverse problem formulation is made. At Section 2.4 the metrics are introduced. Section 2.5 addresses the necessary polarimetry matters, while in Section 2.6 insights about the statistic distribution used in the analysis.

## 2.1. ORIGIN AND GENERATION OF SEA WAVES

The rise and fall of ocean water caused by the gravitational pull of the sun and moon generates sea swell, originating tides, while waves are formed by the action of blowing wind over the surface of the ocean. Sea waves can be classified due to its period, Table 1 refers to that classification.

| **Classification** | **Period** |
|---|---|
| **Capillary waves** | **< 0.1 s** |
| **Ultra-gravity waves** | **0.1 s – 1 s** |
| **Ordinary gravity waves** | **1 s – 30 s** |
| **Infra-gravity waves** | **30 s – 5 min** |
| **Long-period waves** | **5 min – 12 h** |
| **Ordinary tides** | **12 h – 24 h** |
| **Trans-tidal waves** | **> 24 h** |

Table 1 - Sea waves spectrum (Munk, 1951)[5]

Capillary waves are the small waves generated by the wind and may appear on the top of gravity waves. These waves have a short wavelength with a rounded crest, having a similar representation alike simple sinusoidal wave. The maximum period of a capillary wave is 1 second, which from it on, are considered gravity waves. Contrary to gravitational waves,

---

[5] Adapted

velocity of capillary waves increases with decreasing wavelength. Gravity waves have a minimum velocity of 23.1 centimetres per second.

Joint North Sea Wave Project (JONSWAP) waves profiles shape the real-world waves by an approximated spectrum, accounting all the components of the water dislocation, both gravitational factors of their formation and capillary waves within a shorter period formed on a "fetch zone" caused by wind. There is an experimental relation between wind dynamics and the wave elevation and behaviour (Takagaki, Komori, Iwano, Suzuki, & Kumamaru, 2018) (Hasselmann, et al., 1973).

Small fetch waves appear in the nature, on lakes and on top of gravitational waves, formed by the wind action. Capillary waves are mostly formed by the effect of surface tension, without a significant effect from gravity. Roughly the capillary waves are characterized by a period under 0.1 seconds and a wave speed of 0.2 meters per second, as seen on Table 1, however these values are most sensible to the wind conditions and floating components such as microplastics or surfactants (Munk, 1951) (Gade, Alpers, Ermakov, Hühnerfuss, & Lange, 1998).

About the drift of the materials floating on the water, many factors are at stake, including currents, wind, swell and others. The Stokes drift can explain the movement of an object due to the wave's behaviour (Van den Bremer & Breivik, 2017).

## 2.2. THE BRAGG EFFECT

The Bragg-Scattering law (Bragg, Bragg, & Wolff, 1912) explains the effect of backscattering on identical and repeated structures such as the waves crests. According to this effect, the place in the frequency spectrum, $f_{Bragg}$, will suffer from constructive interference due to coherent superposition of reflections, because of the surface geometry. This effect is translated by equation [1], where $d$ is the distance of the reflective sub-surfaces, between water waves crests in this scenario; $\lambda_t$ is the transmitted wavelength, which is the speed of light divided by the frequency, $f_{Bragg}$; and $\theta$ is the incident angle (Bragg angle) of the electromagnetic waves:

$$d^{crests} = \frac{\lambda_t}{2\cos\theta} \qquad [1]$$

Through equation [1] is possible to predict the frequency where the Bragg peak appearance is estimated, where there is constructive interference, $f_{Bragg(predicted)}$, which, in some testes differ from the experimental result, $f_{Bragg}$. Whenever $f_{Bragg(predicted)}$ is not distinguished from $f_{Bragg}$, $f_{Bragg(predicted)} = f_{Bragg}$.

The Bragg Effect is an odd phenomenon that can either be advantageous or unsatisfactory for remote sensing, depending on its application. The existence of an effect, that vary with wind conditions, can be useful to estimate meteorologic phenomena. Also, can facilitate the detection of objects which cause perturbance on those meteorologic phenomena. On the other hand, when sensing targets on the water surface, as this thesis intent to, if waves' arrangement matches the requirements for this effect, it can lead to the impair of the antennas, backscattering a powerful lobe that saturates all the useful information of waves reflection. On Section 3.4 a series of tests will be conducted to assess if the Bragg phenomenon will negatively influence the detection (Chaturvedi, Banerjee, & Lele, 2019).

## 2.3. INVERSE PROBLEM FORMULATION

The description in this section was based on the "MARES"' project problem formulation (Felício, et al., 2023).

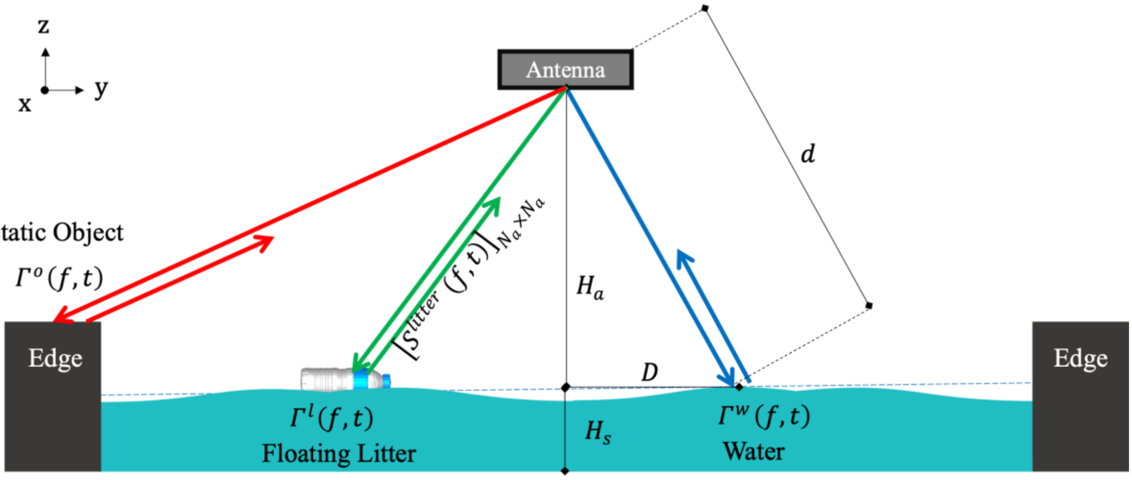

Figure 4 - Schematic for the problem formulation. In red, the antenna's ray is backscattered from a static object, in green, the antenna's ray is backscattered from floating litter, in blue the antenna's ray is backscattered from water.

The image labelled as Figure 4, shows the configuration of the studied scenario, which will serve for this problem's explanation. Foremost, the coordinate system will be set at the mean water level where $z = 0$. The length of the flume defines the $x$ axis with the waves propagating along it's positive direction. The $x$ axis is the antenna's range and $y$ axis, the antenna's cross range. The wave significant height is represented by $H_s$, and the average wave' period by $T$. Broadbands' devices are set at a height above the average water level, $H_s$, illuminating a footprint on the water surface with an inclination angle $\theta$. The look angle will therefore depend on the location on the surface, which is being considered, that angle is given by equation [2].

$$\Psi = \arctan\left(\frac{D}{H_a}\right) \qquad [2]$$

$\Psi$ equals the tilt angle $\theta$ when pointing to on the higher radiation point $(x_0, y_0, z_0 = 0)$, as the ray is emitted directly and backscattered to the antenna. $D$ is the horizontal distance between an antenna and the surface point on a specific water height $(x_0, y_0, z_0)$. $N_a$ is the number of broadband antennas that are connected to the Vector Network Analyser (VNA) that retrieves the $N_a \times N_a$ complex scattering matrix, whose elements are represented by $S_{ij}(f,t)$, at $N_f$ frequencies, swept in the desired band $\Delta f = [f_{min}; f_{max}]$, stepping $f_{step}$ Hz, $N_t$ times. Each sweep therefore considered a time sample $t$, while on the scattering matrix $S_{ij}$, "i" stands for the i^th^ antenna that is transmitting, while "j" stands for the j^th^ antenna which is receiving, which sample.

The received signal is the contribution of the $N_a$ antennas radiation, which collect the contribution of three categories of objects. Static objects $N_o$, which distances $a_o$ from the antenna, have a scattering coefficient of $\Gamma^o(f,t)$. Floating $N_l$ litter objects, which distances $a_l$ from the antenna, have a scattering coefficient of $\Gamma^l(f,t)$. The receiving signal from water requires a conceptual mesh which covers its surface, containing $N_w$ infinitesimal "mirrors" with an area of $\delta A$, which has a scattering coefficient of $\delta\Gamma^w(f,t)$, each "mirror" distancing $a_w$ from the antenna.

Therefore, detecting litter requires two distinct measurements. $S_{ij}^{litter}(f,t)$, [3], containing the samples with litter, and $S_{ij}^{ref}(f,t)$, [4], containing the samples without litter.

$$S_{ij}^{litter}(f,t) = \sum_{w=1}^{N_w} a_w\,\delta\Gamma_w(f,t) + \sum_{l=1}^{N_l} a_l\,\Gamma_l(f,t) + \sum_{o=1}^{N_o} a_o\,\Gamma_o(f) \qquad [3]$$

$$S_{ij}^{ref}(f,t) = \sum_{w=1}^{N_w} a_w\,\delta\Gamma_w(f,t) + \sum_{o=1}^{N_o} a_o\,\Gamma_o(f) \qquad [4]$$

Both the plastic and water contributions are dynamic, and just the surrounding objects contribution is constant. To analyse the backscatter contribution without unwanted clutter, it is necessary to establish calibrated measurements.

In equation [5], $S_{ij}^{cal,litter}$ are the elements from the $N_a \times N_a$ complex scattering matrix, with litter, after its calibration. In equation [6], $S_{ij}^{cal,ref}$ are the elements from the $N_a \times N_a$ complex scattering matrix, without litter, after its calibration. $t$ represents one time sample and $\langle\cdot\rangle$ the time- average over all $N_t$ time samples from the reference.

$$S_{ij}^{cal,litter}(f,t) = S_{ij}^{litter}(f,t) - \langle S_{ij}^{ref}(f,t)\rangle \qquad [5]$$
$$S_{ij}^{cal,ref}(f,t) = S_{ij}^{ref}(f,t) - \langle S_{ij}^{ref}(f,t)\rangle \qquad [6]$$

Sometimes, if the measurements are from a simulated environment where the water contribution is exactly the same on $S_{ij}^{litter}(f,t)$ and $S_{ij}^{ref}(f,t)$, the extraction of the values, without preforming an average over time, is helpful to identify litter. The following equation [7] shows the procedure with $S_{ij}^{ideal,litter}(f,t)$.

$$S_{ij}^{ideal}(f,t) = S_{ij}^{litter}(f,t) - S_{ij}^{ref}(f,t) \qquad [7]$$

To create images, designated as waterfalls, it is necessary to post process the calibrated $S_{ij}^{cal,litter}(f,t)$ and $S_{ij}^{cal,ref}(f,t)$ matrices. In some situations, also $S_{ij}^{ideal}(f,t)$. The matched filter is a technique for improving the Signal to Noise Ratio (SNR) and probability of detection when additive Stochastic noise[6] is present. MATLAB offers a range of tools for improving the SNR and, therefore creating a better waterfall (MathWorks, 2019/2023).

$k_{0,f}$ is the wavenumber, $k_{0,f} = \frac{2\pi \cdot \mathrm{f}}{\lambda}$ $[rad.m^{-1}]$, $d$ is the distance between the antenna and the surface of the water. All frequencies are then summed up on the desired sub band. $I_{ij}^{litter}(d,t)$ from [8] is the Intensity matrix for the calibrated measurement with litter. $I_{ij}^{ref}(d,t)$ from [9] is the Intensity matrix containing the calibrated reference measurement. $I_{ij}^{ideal}(d,t)$ contains the Intensity of ideal litter measurement [10].

$$I_{ij}^{litter}(d,t) = \left| \frac{1}{N_f} \sum_{f=1}^{N_f} S_{ij}^{cal,litter}(f,t) e^{j \cdot k_{0,f} \cdot 2d} \right|^2 \qquad [8]$$

$$I_{ij}^{ref}(d,t) = \left| \frac{1}{N_f} \sum_{f=1}^{N_f} S_{ij}^{cal,ref}(f,t) e^{j \cdot k_{0,f} \cdot 2d} \right|^2 \qquad [9]$$

$$I_{ij}^{ideal}(d,t) = \left| \frac{1}{N_f} \sum_{f=1}^{N_f} S_{ij}^{ideal}(f,t) e^{j \cdot k_{0,f} \cdot 2d} \right|^2 \qquad [10]$$

To create a waterfall, the square value of the absolute $I_{ij}^{litter}(t,d)$, $I_{ij}^{ref}(t,d)$ or $I_{ij}^{ideal}(t,d)$ is plotted in logarithmic units. Those waterfalls, contain a colour bar which identifies the energy level of each pixel. The vertical scale is named “Samples”. The “samples” are taken each time instant $t$. The horizontal axis is the “distance”, in meters, $d$.

The waterfall generation process under experimental conditions uses an outlier remotion function, native to MATLAB. The aim of this process is due to imprecisions on real life antennas or anormal factors (as wind shaking the antenna stand) which does not exist under a

---

[6] Stochastic noise is caused by a Stochastic resonance which is present on weaker signals difficult to detect. Therefore, their detection can be boosted by adding white noise.

simulated environment. For this reason, the outlier remotion process is applied just under experimental data, and not under numeric results.

| **Frequency band designation** | $f_{min}$ **[GHz]** | $f_{max}$ **[GHz]** |
|---|---|---|
| **S-band** | **2** | **4** |
| **“C-under” band (Cu)** | **4** | **6** |
| **“C-above” band (Ca)** | **6** | **8** |
| **“X-under” band (Xu)** | **8** | **10** |
| **“X-above” band (Xa)** | **10** | **12** |
| **“Ku-under” band (Kuu)** | **12** | **15** |
| **“Ku-above” band (Kua)** | **15** | **18** |
| **K band (K)** | **18** | **20** |
| **Ultrawideband (UWB)** | **3.1** | **10.6** |

Table 2 - Non-standard frequency bands under study

# 2.4. METRICS

The objective of this section is to introduce all metrics used through the study. First the quality metric related to the energy is introduced at Topic 2.4.2, then metrics related to the reduction of the Bragg peak at Topic 2.4.3.

## 2.4.1. NORMALIZED ENERGY

The energy level contained in a waterfall is useful to compare experiments between each other. This metric in, therefore normalized to the number of points in the waterfall, in equation [11], originating $E_{ij}$, or E. Depending on the litter concentration, $E_{ij}^{litter}$ or $E_{ij}^{ref}$ in the absence of litter

$$E_{ij} = \frac{\sum_{t=1}^{t_{max}} \sum_{d=d_{min}}^{d_{max}} I_{ij}^{litter}(d,t)}{t \cdot d} \qquad [11]$$

## 2.4.2. ENERGY RATIO COEFFICIENT

To compare measurements, we propose a metric designated as Energy Ratio coefficient (EnR) (Felício, et al., 2023). The EnR manifest the quality of each measurement, helping to decide which parameters and methods need to be adjusted in order to improved results. Whenever $EnR$ > 1 there is a positive detection of floating litter. If $EnR$ < 1 there is no detection.

The EnR coefficient is calculated with equation [12].

$$\mathrm{EnR_{ij}} = \frac{E_{ij}^{litter}}{E_{ij}^{ref}} \qquad [12]$$

### 2.4.3. BRAGG PEAK METRICS

Another important metric to introduce is Peak Reduction Metric, measured by a number, the Peak Reduction Coefficient (PR). This coefficient indicates by how much the Bragg effect is reduced when the concentration of floating objects is increased. The coefficient is defined in Equation [13]. $\mathrm{E}_{f_{Bragg}}^{ref}$ stands for the energy, in dB, of a measure without litter, and $\mathrm{E}_{f_{Bragg}}^{litter}$ for a measure with litter, at the Bragg Peak.

$$PR\ [dB] = \mathrm{E}_{f_{Bragg}}^{ref} - \mathrm{E}_{f_{Bragg}}^{litter} \qquad [13]$$

## 2.5. POLARIMETRIC ANALYSIS

As discussed in Section 1.2.2, distinct polarization perspectives lead to different results depending on the object characteristics and position (Hajnsek & Desnos, 2021). To identify the pairs of polarization H states for Horizontal polarization and V for vertical. The first letter of the pair stands for the i$^{th}$ antenna which is transmitting, and the second for the j$^{th}$ antenna which is receiving. Throughout the polarimetric analysis, Bistatic Backscatter Alignment (BSA) convention is considered, meaning that there is reciprocity, equation [14].

$$S_{HV_{BSA}} = S_{VH_{BSA}} \qquad [14]$$

Diverse polarimetry data can serve different purposes depending on its processing. In this thesis two ways of decomposing and interpret the polarimetric date are proposed. A Linear Decomposition, in Topic 2.5.1 and a Pauli Decomposition in Topic 2.5.2. To visualize the results, waterfalls were created with the polarimetric information from each antenna, associated with a colour. The chosen colours are red, green, and blue, the primary colours from the visible light spectrum.

### 2.5.1. LINEAR DECOMPOSITION

The first proposed interpretation of the polarimetric data is a decomposition in a linear basis. This decomposition permits a visually identification of the predominant polarimetric antenna on a certain location of the waterfall.

Cross-polarization as Vertical-Horizontal Polarisation (VH) or Horizontal-Vertical Polarisation (HV), contain halt the energy of co-polarization, as Vertical-Vertical Polarisation (VV) or Horizontal-Horizontal Polarisation (HH). For this reason, they are added to one another and not average, or for instance one of them ignored, due to BSA convention.

Red was the chosen colour to identify HH, $I_{HH}^{litter}(d,t)$. Green identifies and cross-polarization, $I_{HV+VH}^{litter}$. Blue identifies VV, $I_{VV}^{litter}(d,t)$. If desired, in a same manner $I_{HH}^{ref}(d,t)$, $I_{HV+VH}^{ref}$ and $I_{VV}^{ref}(d,t)$ can be processed. Overlapping $I_{HH}^{litter}(d,t)$, $I_{HV+VH}^{litter}$, and $I_{VV}^{litter}(d,t)$ in their corresponding colours creates an RGB waterfall.

Some other combinations will also be addressed, such as the intensity from all antennas, $I_{ALL}^{litter}(d,t) = I_{S_{11}+S_{12}+\cdots+S_{1j}+\cdots S_{ij}}^{litter}(d,t)$; intensity from full polarimetry, $I_{POL}^{litter}(d,t) = I_{S_{HH}+S_{HV}+S_{VH}+S_{VV}}^{litter}(d,t)$ and $I_{ALL_{VV}}^{litter}(d,t) = I_{S_{VV_1}+S_{VV_2}+\cdots+S_{VV_n}}^{litter}(d,t)$, where $n$ is the number of VV antennas. The same combinations can also be applied to energy. Energy from all antennas, $E_{ALL} = E_{S_{11}+S_{12}+\cdots+S_{1j}+\cdots S_{ij}}$; energy from full polarimetry, $E_{POL} = I_{S_{HH}+S_{HV}+S_{VH}+S_{VV}}$ and $E_{ALL_{VV}} = E_{S_{VV_1}+S_{VV_2}+\cdots+S_{VV_n}}$, where $n$ is the number of VV antennas. Note that the energy levels are normalized to the number of considered antennas and not only to the number of the waterfall points.

### 2.5.2. PAULI DECOMPOSITION

The polarimetric data can lead to diverse interpretations besides the representation of each polarimetric component individual or all together. Another form to analyse polarimetric data is through the existence of the polarimetric coherency matrix, $K$ matrix in equation [15], which will be used on the Pauli decomposition to characterize distributed scatterers performed through the coherency (Hajnsek & Desnos, 2021).

$$K = \begin{bmatrix} |S_{HH}+S_{VV}|^2 & (S_{HH}+S_{VV})(S_{HH}-S_{VV})^* & (S_{HH}+S_{VV})(S_{HV}+S_{VH})^* & (S_{HH}+S_{VV})\big(j(S_{HV}-S_{VH})\big)^* \\ (S_{HH}-S_{VV})(S_{HH}+S_{VV})^* & |S_{HH}-S_{VV}|^2 & (S_{HH}-S_{VV})(S_{HV}+S_{VH})^* & (S_{HH}-S_{VV})\big(j(S_{HV}-S_{VH})\big)^* \\ (S_{HV}+S_{VH})(S_{HH}+S_{VV})^* & (S_{HV}+S_{VH})(S_{HH}-S_{VV})^* & |S_{HV}+S_{VH}|^2 & (S_{HV}+S_{VH})\big(j(S_{HV}-S_{VH})\big)^* \\ j(S_{HV}-S_{VH})(S_{HH}+S_{VV})^* & j(S_{HV}-S_{VH})(S_{HH}-S_{VV})^* & j(S_{HV}-S_{VH})(S_{HV}+S_{VH})^* & |S_{HV}-S_{VH}|^2 \end{bmatrix} \qquad [15]$$

As we are considering BSA convention $T$ matrix can be simplified to equation [16].

$$K = \begin{bmatrix} |S_{HH}+S_{VV}|^2 & (S_{HH}+S_{VV})(S_{HH}-S_{VV})^* & 2(S_{HH}+S_{VV})(S_{HV})^* \\ (S_{HH}-S_{VV})(S_{HH}+S_{VV})^* & |S_{HH}-S_{VV}|^2 & 2(S_{HH}-S_{VV})(S_{HV})^* \\ 2(S_{HV})(S_{HH}+S_{VV})^* & 2(S_{HV})(S_{HH}-S_{VV})^* & 4|S_{HV}|^2 \end{bmatrix} \qquad [16]$$

Unlike linear basis, which is typically used to compare Horizontal and Vertical polarized pairs, the Pauli basis $\{\boldsymbol{S_a}, \boldsymbol{S_b}, \boldsymbol{S_c}, \boldsymbol{S_d}\}$ is composed of four 2 x 2 matrices (Hajnsek & Desnos, 2021), equations [17], [18], [19] and [20], respectively.

$$\boldsymbol{S_a} = \frac{1}{\sqrt{2}}\begin{bmatrix} 1 & 0 \\ 0 & 1 \end{bmatrix} \qquad [17]$$

$$\boldsymbol{S_b} = \frac{1}{\sqrt{2}}\begin{bmatrix} 1 & 0 \\ 0 & -1 \end{bmatrix} \qquad [18]$$

$$\boldsymbol{S_c} = \frac{1}{\sqrt{2}}\begin{bmatrix} 0 & 1 \\ 1 & 0 \end{bmatrix} \qquad [19]$$

$$\boldsymbol{S_d} = \frac{1}{\sqrt{2}}\begin{bmatrix} 0 & -1 \\ 1 & 0 \end{bmatrix} \qquad [20]$$

Due to BSA convention, the Pauli basis is composed just by $\{\boldsymbol{S_a}, \boldsymbol{S_b}, \boldsymbol{S_c}\}$. Therefore, a scattering matrix S can be expressed in equation [21]:

$$\mathbf{S} = \begin{bmatrix} \mathrm{S_{HH}} & \mathrm{S_{HV}} \\ \mathrm{S_{HV}} & \mathrm{S_{VV}} \end{bmatrix} = \mathrm{a}\mathbf{S_a} + \mathrm{b}\mathbf{S_b} + \mathrm{c}\mathbf{S_c} \qquad [21]$$

Where the coefficients $a$ is given by [22], $b$ is given by [23] and $c$ is given by [24].

$$a = \frac{S_{HH} + S_{VV}}{\sqrt{2}} \qquad [22]$$

$$b = \frac{S_{HH} - S_{VV}}{\sqrt{2}} \qquad [23]$$

$$c = \sqrt{2} S_{HV} \qquad [24]$$

Each matrix has different physical significance. $\mathbf{S_a}$ pertains to a single bounce, an odd bounce scattering mechanism; $\mathbf{S_b}$ double bounce, an even bounce; and $\mathbf{S_c}$ scattering mechanisms which involves multiple reflections, for more than two bounces, as illustrated in Figure 5.

Following the analysis for Linear Decomposition in Topic 2.5.1, is possible to associate the Pauli basis coefficients $\{\boldsymbol{S_a}, \boldsymbol{S_b}, \boldsymbol{S_c}\}$ as scattering matrixes from new antennas. Therefore $I_{\mathrm{S_a}}^{litter}(d,t)$ is represented in red, $I_{\mathrm{S_b}}^{litter}(d,t)$ in green and $I_{\mathrm{S_c}}^{litter}(d,t)$ in blue (Hajnsek & Desnos, 2021). Overlapping $I_{\mathrm{S_a}}^{litter}(d,t)$, $I_{\mathrm{S_b}}^{litter}(d,t)$, and $I_{\mathrm{S_c}}^{litter}(d,t)$ in their corresponding colours creates an RGB waterfall. Also, with the necessary adaptations, metrics from Topic 2.4.1 and Topic 2.4.2 such as the E and EnR can be calculated for this purpose.

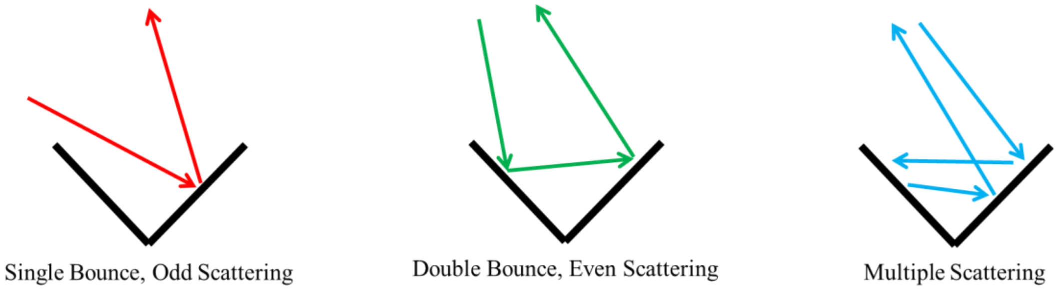

Figure 5 - Physical interpretation of the scattering mechanism identified by each colour (RGB). Single bounce in red, double bounce in green and multiple bounces in blue.

## 2.6. BURR TYPE XII DISTRIBUTION

In 1942 Irving Wingate Burr introduced a wide range of distributions (Burr, 1942) which can fit a wide range of empirical observations, some in the field of mobile communications. Burr Type XII Cumulative Distribution Function (CDF) is in equation [25]. *c* and *k* are the shape parameters and α is the scale parameter.

$$F(|a,c,k) = 1 - \frac{1}{\left(1+\left(\frac{x}{a}\right)^{c}\right)^{k}}, x > 0, a > 0, c > 0, k > 0 \qquad [25]$$

The Probability Density Function (PDF) is in equation [26].

$$f(|a,c,k) = 1 - \frac{\frac{kc}{a}\left(\frac{x}{a}\right)^{c-1}}{\left(1+\left(\frac{x}{a}\right)^{c}\right)^{k+1}}, x > 0, a > 0, c > 0, k > 0 \qquad [26]$$

# 3. NUMERICAL ANALYSIS AND DISCUSSION

In this chapter the results are numeric generated from Computer Simulation Technology (CST) Studio Suite® (Dassault Systèmes, 2002 - 2023) and therefore post processed in MATLAB (MathWorks, 2019/2023) according to the formulation and methodology in Chapter 2. First, in Section3.1, verifications and setup validations are performed as an introduction to this chapter. After that, Section 3.2 discusses the behaviour of the Bragg peak under different observation angles. Section 3.3 studies the Bragg Peak under a variety of plastic concentrations. Section 3.4, studies the plastic detection under the Bragg effect presence. Finally, Section 3.5 closes the chapter with wider JONSWAP simulations.

## 3.1. NUMERICAL ANALYSIS INTRODUCTION

This section is an introduction to Chapter 3, where the steps to create the final models are described. CST was the tool of choice due to its 3D simulations of high performance, adequate to analyse electromagnetic components and systems. The intention is to simulate seawater in the presence of floating litter to afterwards take conclusions on a variety of aspects. The prime objective is to log environments with huge dimensions to be as close as the real ocean, which bring concerns about this software's limitations and about the limitations of the available computational resources.

The following topics concern the various steps into the creation of the simulations. In Topic 3.1.1 the main setting to be carried out through all simulations are enumerated. In Topic 3.1.2 a verification of the model with the Bragg effect is performed. Topic 3.1.3 explains the reason for the CST solver choice. To Topic 3.1.4 concern the object's material choice. Topic 3.1.5 defines the ray density choice and the reasons behind. In Topic 3.1.6 different concentrations of plastic are introduced. In Topic 3.1.7 the Sinusoidal Model Setup is explained, while on Topic 3.1.8 the JONSWAP Model Setup is introduced.

### 3.1.1. NUMERICAL SETUP

The setup consists of a surface with floating bottles. The surface consists either on a Sinusoidal Model Setup (later described in Topic 3.1.7) or on a JONSWAP Model Setup (later described in Topic 3.1.8). The dimensions used are one square meter for the tests, 1.5 square meter for a smaller setup and 100 square meter for the wider setup.

The simulations frequency band, $\Delta f$, ranges from $f_{min} = 4\ GHz$ to $f_{max} = 12\ GHz$, with a step of $f_{step} = 0.04$ Hz. The simulation band contains all sub bands that will be analysed. The intent is to simulate an antenna installed in a hovering platform aiming 45 degrees to the ground. The transmitted wave is, therefore, an infinite monostatic plane wave with $\theta = 45°$. The azimuth $\varphi$ can take tree angles. When not mentioned $\varphi = 0°$ (in figures $\varphi$ is referred as "phi"). If $\varphi = 0°$, the observation is facing the crests of the waves with the bottles closing on the observer. As the angle increase, the observer will rotate until $\varphi = 90°$. The wave is single polarized, VV. The water significant height on the Sinusoidal Model Setup is $H_s = 3\ cm$, and on the JONSWAP Model Setup $H_s = 9\ cm$.

### 3.1.2. SIMULATION ENVIROMENT

An efficient way of validating the setup is verifying the Bragg effect, referred before in Section 2.2. Through Figure 6 it is possible to validate the general configurations, as the analytic calculations for the Bragg peak are consistent to those that display on the simulation.

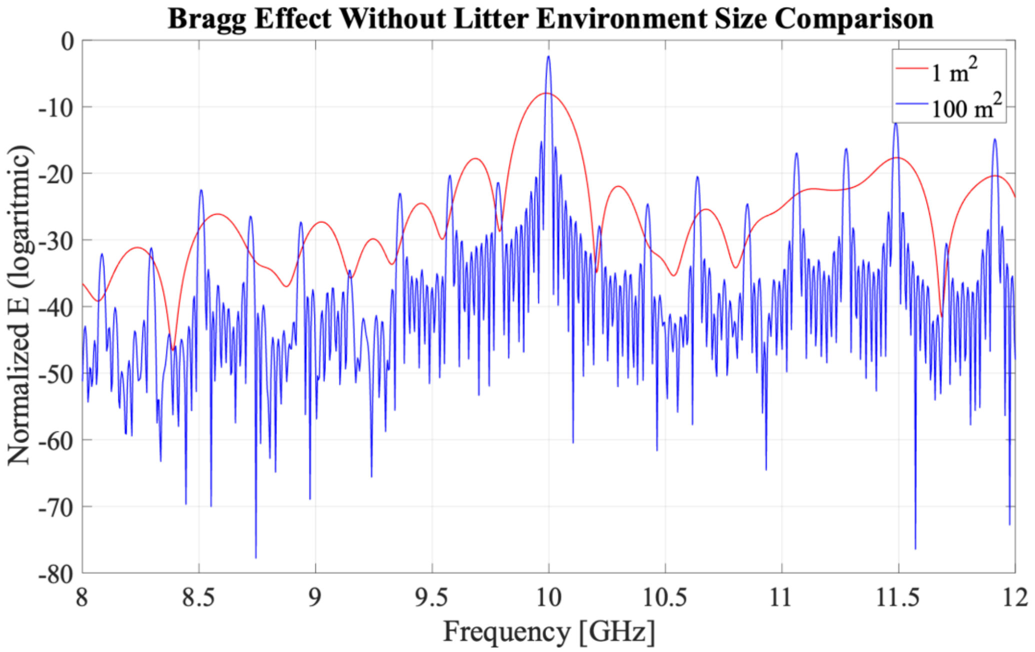

Figure 6 - Scattered energy by incident plane wave showing the $f_{Bragg} = 10$ GHz for two different sized models.

The distance between wave crests used to generate Figure 6 is $d^{crests} = 20\ mm$, and the angle between the incident wave and the sea surface is $\theta = 45°$. The azimuth angle $\varphi = 0°$. According to equation [1], the frequency where the back scattering is most significant is $f_{Bragg} = 10$ GHz, as shown in Figure 6. When comparing two different sized 3D models is possible to conclude that the one square meter model has the peaks on the same location as the 100 square meter model. The 100 square meter model is "sharper", with more frequency discrimination, appearing to have more points along the frequency.

### 3.1.3. SOLVER

The CST software has multiple available options for solving the problems, leading to different computational efforts. The selected solver must be accurate and performing simulations at a lower computational demand.

The Integral Equation Solver is a full-wave solver that uses the method of moments technique (Sheng & Song, 2012) with multilevel fast multipole method. This solver uses just the object surfaces, which is much lighter than volumetric methods. However, this solver is fairly intensive as it discretizes all the integral equations of the electromagnetic field. A possible solution would be the use of an Asymptotic Solver which is more suitable for extremely large structures on which a full-wave solver, such as the Integral Solver, shows unnecessary. This solver uses a Shooting Bouncing Ray method which performance can be enhanced through hardware tunning (Shi, Tang, & Wang, 2017).

The asymptotic solver appears more attractive; however, the use of this solver implies making an approximation of the problem which needs to be validated before used. As the objective at this point is to validate the solver, one square meter of water with a sinusoidal wave is considered enough to be logged, otherwise, a bigger surface will lead to an overcharge of the hardware available, and therefore interrupt the simulation while running the integral solver. The material used for the sea is a Perfect Electric Conductor (PEC). In Topic 3.1.4 will be discussed why PEC can replace seawater. The two scenarios, one with the Integral Equation Solver, and the other with the Asymptotic Solver are compared, after normalized. After testing both solvers under the same conditions, the results were plotted in Figure 7, confirming that both solvers response are approximately the same. Therefore, the Asymptotic Solver will be used to represent the sea surface as it delivers accurate results at a much faster result rate while compared to the Integral solver.

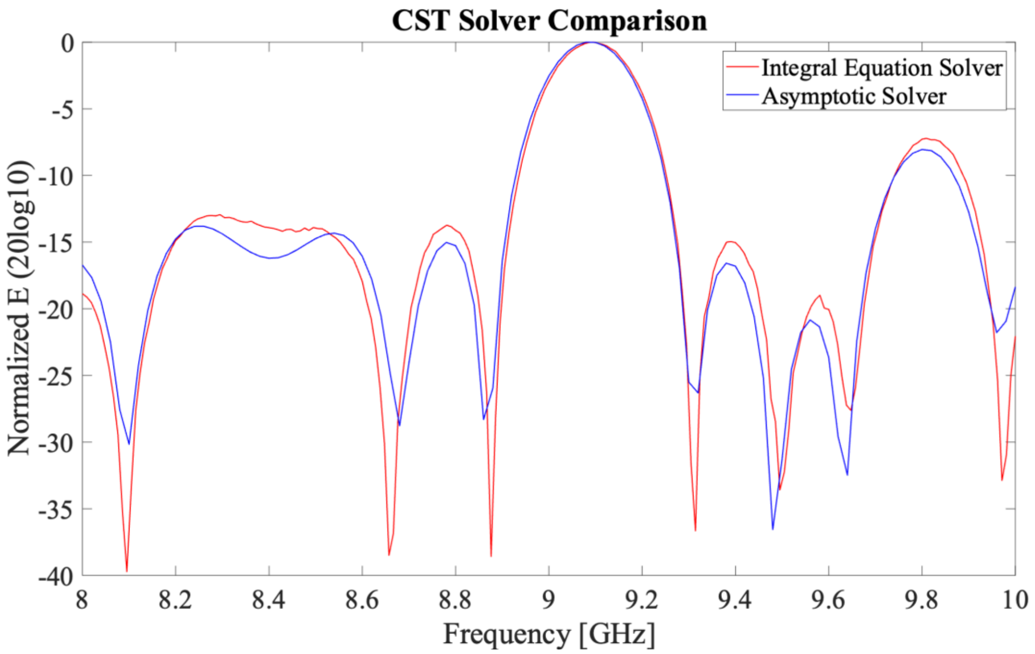

Figure 7 - Solver Comparison, comparing the Asymptotic solver to the Integral solver.

### 3.1.4. MATERIALS

As seawater can be replaced with a PEC material and plastic bottles by its indentation on the water (Martins, Felício, Matos, da Costa, & Fernandes, 2021) (Felício, et al., 2023) (Costa T. S., Felício, Matos, & Fernandes, 2023) (Costa T. S., et al., 2023) those simplification will be tested as they save computational effort. Salt water and fresh water will also be compared on a 100 square meter with sinusoidal waves environment.

In CST, simulating sea water is more computationally intensive than simulating a PEC. The scattered energy on the water behaves differently depending on the frequency in use. A PEC is less computationally intensive and therefore quicker to simulate. To simulate water in CST, a PEC was coated with the salt and fresh water. The coating layer need to be thick enough, so that PEC surface properties does not influence the water properties. Figure 8 contains the real and imaginary values of both salt and freshwater permittivity which allow the calculation of penetration depth of electromagnetic waves through the surface (Meissner & Wentz, 2004).

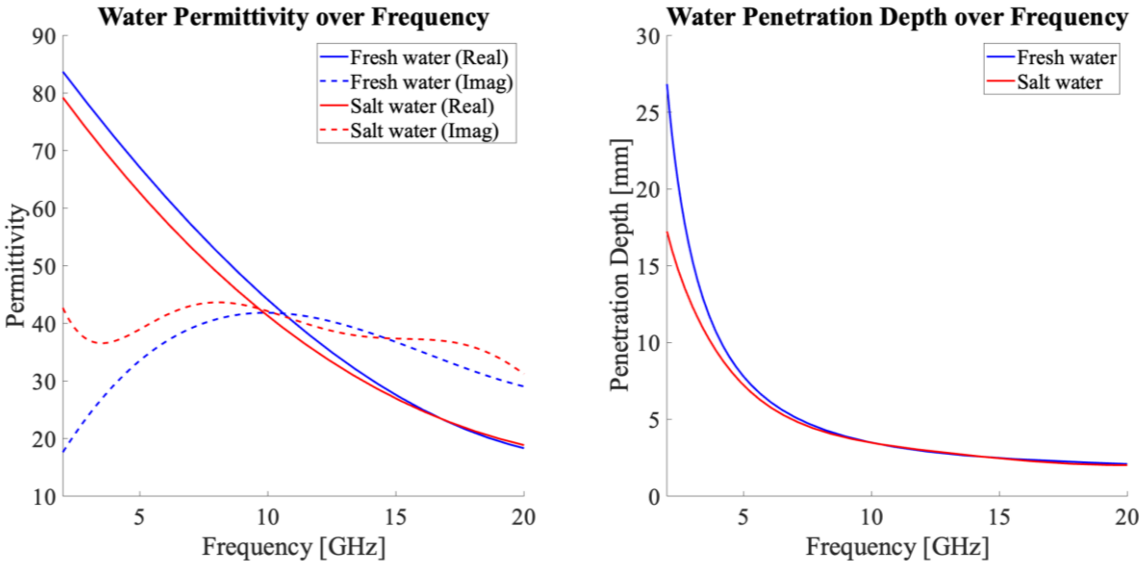

(a) (b)

Figure 8 – Study of water penetration depth. (a) Water permittivity over frequency (Pozar, 2011); (b) Water Penetration Depth over Frequency.

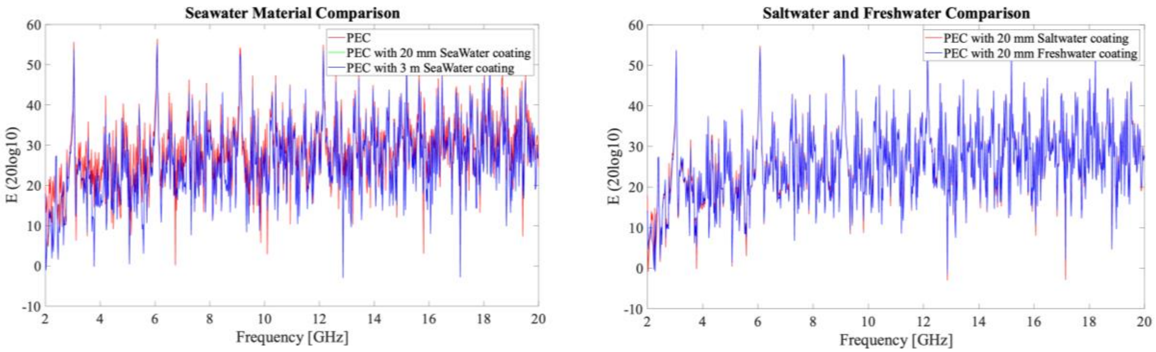

(a) (b)

Figure 9 - Backscattered energy along frequency to compare different the seawater materials. (a) Comparing PEC seawater coated PEC; (b) comparing PEC coated with saltwater to PEC coated with freshwater.

Figure 9(a) proves that the frequency is similar on all three materials. The figure also proves that a PEC material coated by 20 centimetres of water is enough thickness for the material to be considered as just a water surface, as Figure 8(b) states. In terms of salinity, Figure 9(b) shows that the differences between salt and fresh water are not significant, what is in line with the similarities between salt water permittivity and fresh water permittivity on Figure 8(a).

In the simulations, the litter elements introduced on the water are plastic bottles based on a 33 centilitres commercial mineral water bottle. Figure 10 and Figure 11 contains the measurements for the plastic object, which is shaped as cylinders that measure 16,4 centimetres height by 5,3 centimetres diameter. Each bottle creates an indentation area of 0.22 square meters while partially submerged 2.5 centimetres. The weight considered for each bottle is 12 grams.

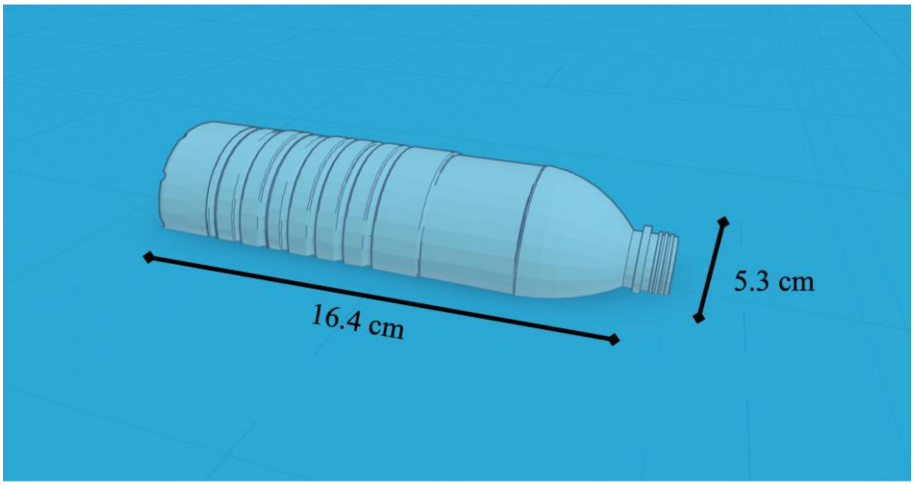

Figure 10- Plastic bottle dimensions, surface view

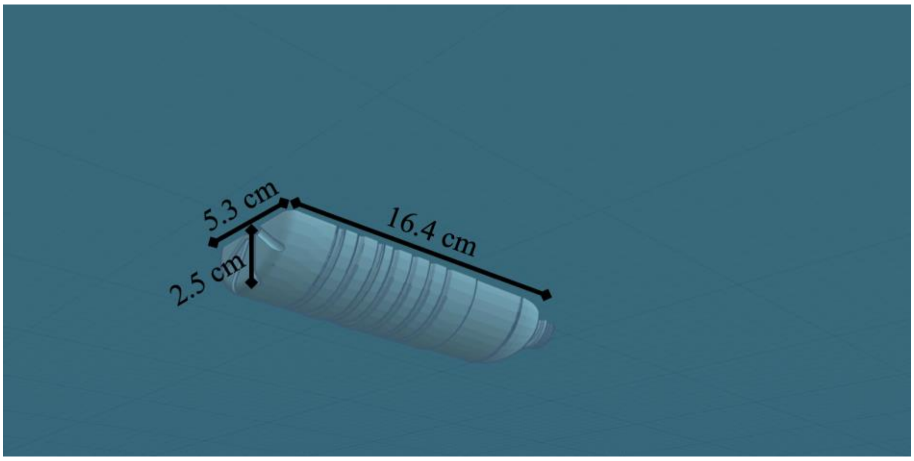

Figure 11 - Plastic bottle dimensions, underwater view

Figure 12(b) compares the response of floating plastic bottles to the response of just its indentation on Figure 12(a). Figure 12(b) confirms that both simulations lead to the exact same results as both lines of the graphs are coincident what went according to the previous research mentioned in the beginning of this topic.

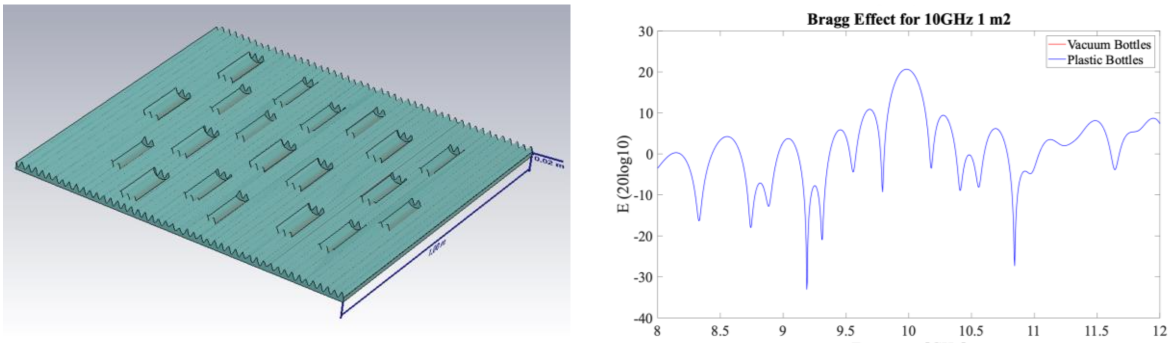

(a)

(b)

Figure 12 - CST test model. (a) Plastic bottles indentation; (b) Energy over frequency comparison between plastic bottles and only its indentation.

### 3.1.5. RAY DENSITY

As there is a limited computational resource, it is important to have a mindful tuning of the CST settings. The ray density is a very important setting of those, as it places a huge role in hardware demand. However, to correctly see the Bragg effect, the ray density had to be increased, but just the necessary, to ensure that the backscatter suffers alterations with the irregular surface and that the rays fill all wave "gaps" between crests. Figure 13 is an example of the default CST ray density[7] which will lead to a result where the Bragg effect don't behave as predicted. To avoid this, the simulations consider up to 2000 ray samples per square meter. These settings assure a faster simulation, that can expand to the desirable 100 square meter environment, still processed under a decent amount of time (around one day for 800 samples of a 100 square meter model).

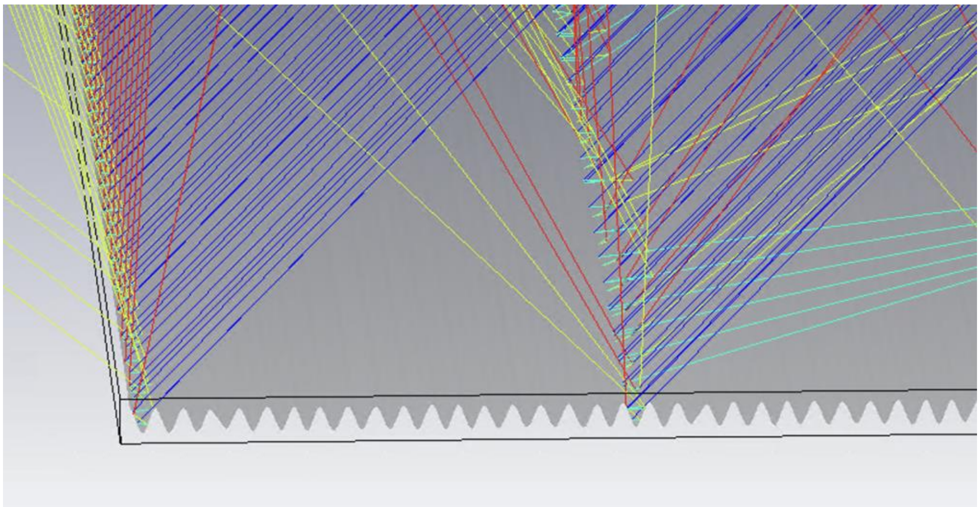

Figure 13 – Incorrect ray density, leading to wrong results.

---

[7] By default, the represented ray number is smaller than the actual rays, in this figure the represented rays equal the default CST ray density.

### 3.1.6. CONCENTRATION

Varying the plastic concentration on the models is an essential study subject. Assuming the bottles dimensions and weight, previously mentioned in Topic 3.1.4, Table 3 quantify the plastic patch depending on the number of bottles.

Sinusoidal Model Setup plastic patches measures 1 square meter independent to the sea model's dimension. The concentration will depend on the sea model dimensions, which also are the antenna footprint's dimensions[8]. In Table 3 the concentrations refer to the plastic concentration in the plastic patch, over a one square meter surface.

| **Number of bottles** | **Plastic concentration on the plastic patch** | **Plastic populated area on the plastic patch** |
|---|---|---|
| **1 bottle** | **12 g/m$^2$** | **0.87 %** |
| **2 bottles** | **24 g/m$^2$** | **1.75 %** |
| **3 bottles** | **36 g/m$^2$** | **2.62 %** |
| **4 bottles** | **48 g/m$^2$** | **3.49 %** |
| **5 bottles** | **60 g/m$^2$** | **4.37 %** |
| **10 bottles** | **120 g/m$^2$** | **8.74 %** |
| **15 bottles** | **180 g/m$^2$** | **13.10 %** |
| **20 bottles** | **240 g/m$^2$** | **17.47 %** |

Table 3 - Quantification of plastic concentration over a one square meter surface.

### 3.1.7. SINUSOIDAL MODEL SETUP

With a sinusoidal surface there are two variations of the sinusoid period and two variations of the size. The smaller model measures 1 meter wide by 1.5 mete long, with a total area of 1.5 square meter. This model is identified in Figure 14. The second model is identical to the first but measures 10 meter by 10 meter, with a total area of 100 square meter. This model is identified in Figure 15.

---

[8] Since the used wave is an infinite plane wave.

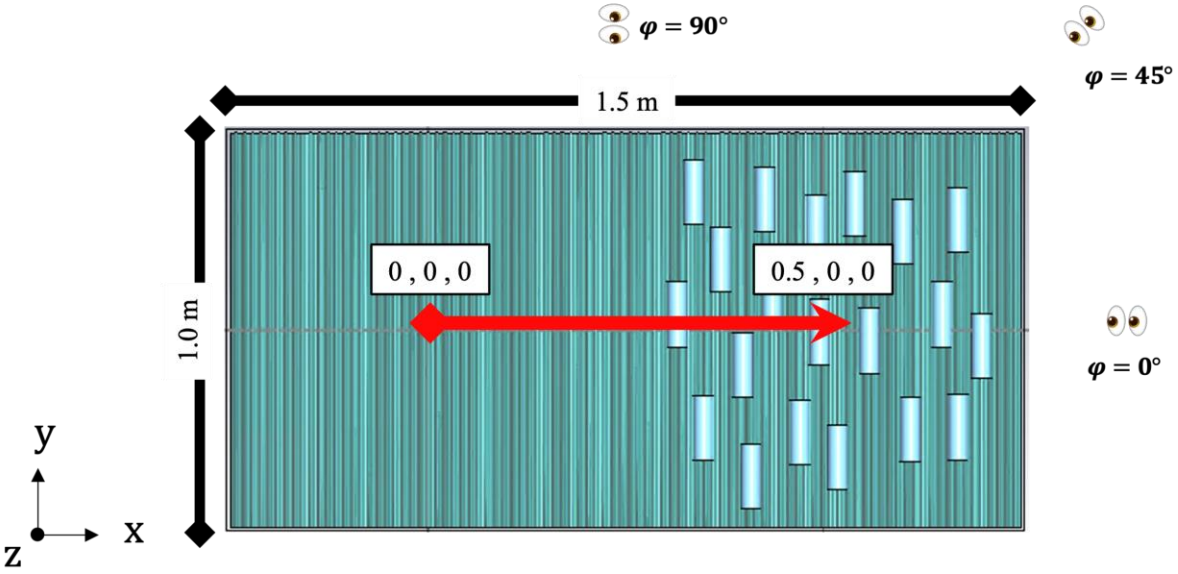

Figure 14 – 1.5 square meter model of the simulated sea with 20 plastic bottles [160 g/m$^2$], $H_s = 3\ cm$. Dimensions are in meters.

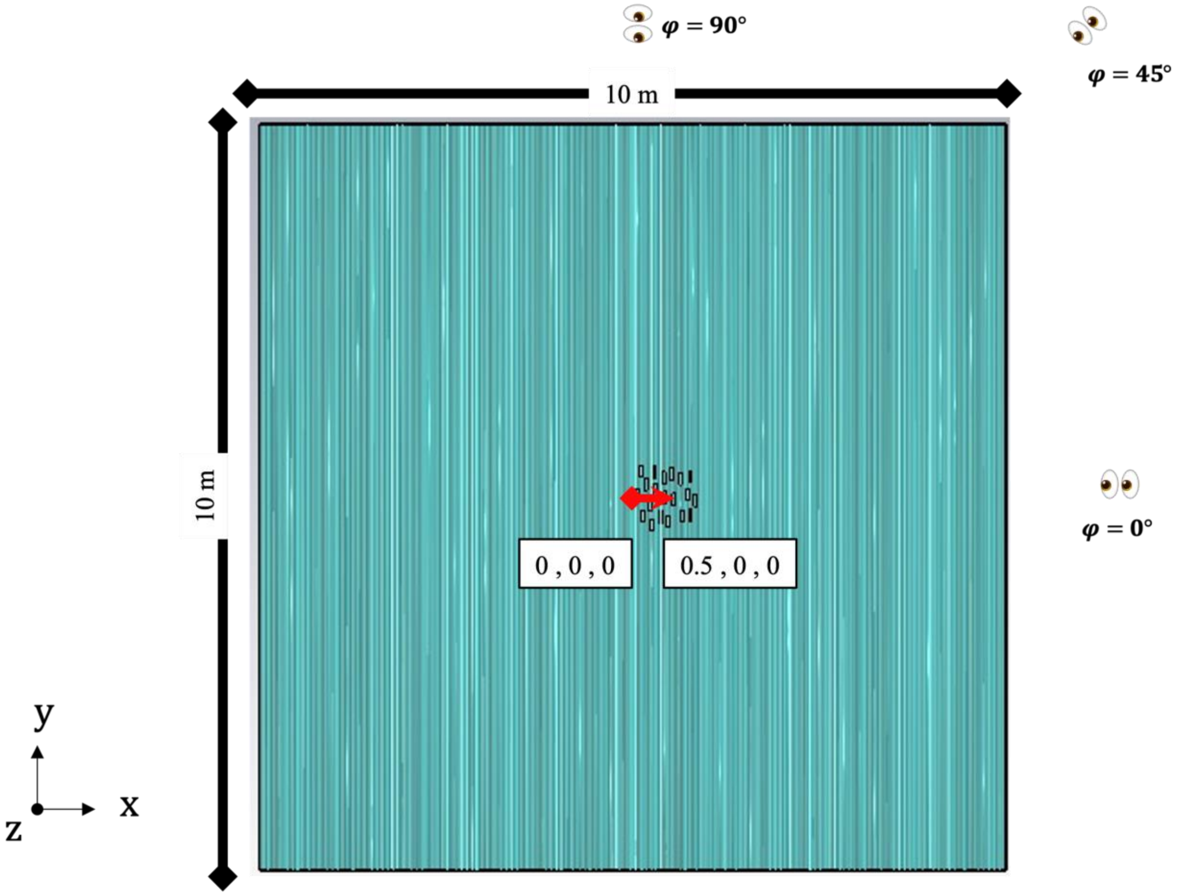

Figure 15 – 100 square meter model of the simulated sea with 20 plastic bottles [2.4 g/m$^2$], $H_s = 3\ cm$. Dimensions are in meters.

On both models the plastic patch measures 1 meter by 1 meter, containing inside the number of bottles that match the desired concentration, without variating its height or relative distance between each other. The plastic patch moves 50 centimetres, while the sea waves move at a different speed. In each simulation 11 samples were performed, allowing the completion of more than one water wave period. The speed of the water waves is 50 times higher than the speed of the bottles. The route of the plastic patch is a straight line across the $x$ axis, as in Figure 14 and Figure 15. Sampling the models also grants the use of the metrics introduced on Section 2.4.

Figure 16 contains two particular simulation cases of sinusoidal models. In Figure 16(a) there is an absence of waves, $H_s = 0$. Here the bottles movement towards the observation antenna is clearly visually identified. The reason for the appearance of vertical lines on the less scattered part of the image in terms of energy (which represents the sea) is not clear identified. In Figure 16(b), to the litter measurements was subtracted the corresponding references measurements. This subtraction is made through equation [10]. Also, with this method the bottles are clearly identifiable.

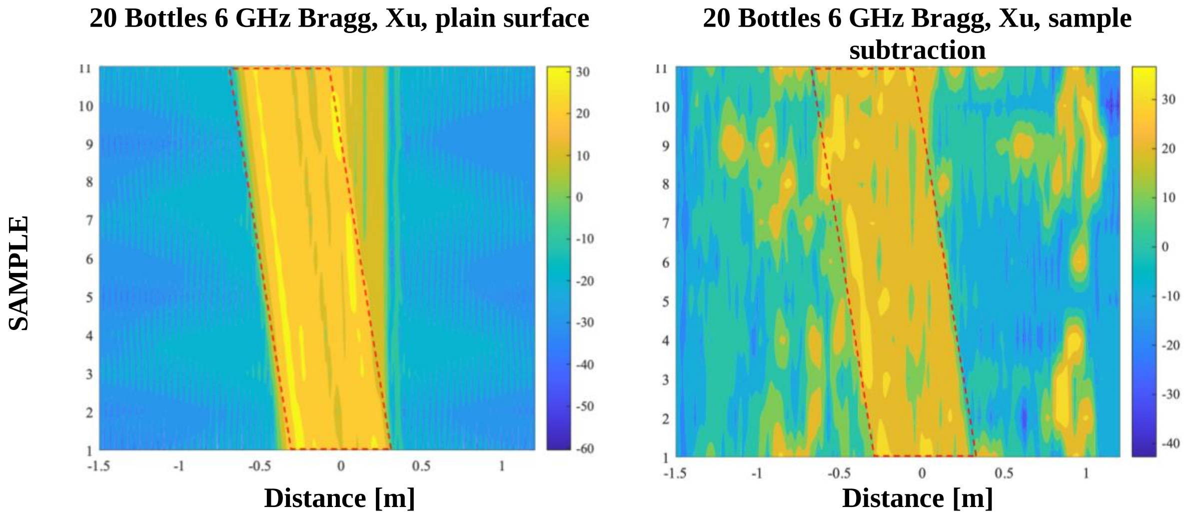
**20 Bottles 6 GHz Bragg, Xu, plain surface**

**20 Bottles 6 GHz Bragg, Xu, sample subtraction**

(a)

(b)

Figure 16 – Particular tests of behaviours to $f_{Bragg} = 6$ GHz on Xu band, in the presence of floating 20 plastic bottles [160 g/m2]. (a) $I_{ij}^{litter}(d,t)$ for $H_s = 0$; (b) An "ideal" subtraction where reference is being subtracted to its corresponding litter measurement, $I_{ij}^{ideal}(d,t)$ for $H_s = 3\ cm$.

Besides testing purposes, Figure 16 situations do not represent experimental scenarios. The absence of waves is not real and to acquire the same exact measurement with and without litter is also unrealistic. While using the Sinusoidal Model Setup two sinusoidal forms were performed, one to match the Bragg criteria to create a peak on $f_{Bragg} = 6$ GHz , and other to match the criteria to create the same peak on $f_{Bragg} = 10$ GHz, predicted according to equation [1] from Section 2.2. Those frequencies were chosen because, since the primary chosen band is the X band, from 8 to 12 GHz. The $f_{Bragg} = 10$ GHz, therefore, appears at the middle of the X band. The $f_{Bragg} = 6$ GHz peak appears outside the band, and it is the second peak at the edge end of the band, at 12 GHz. In Topic 3.1.1 a wider band $\Delta f = [4; 12]\ GHz$ was defined for the simulations allowing the possibility of a more comprehensive analysis of this case of study.

### 3.1.8. JONSWAP MODEL SETUP

The JONSWAP Model Setup is an alternative environment to the previous introduced Sinusoidal Model Setup. The JONSWAP spectrum is inspected in Section 2.1. In this model bottles move away from the observation antenna, contrary to what happen on the sinusoidal model where bottles move towards the observation antenna.

JONSWAP simulations contains 41 samples with litter and 801 reference samples. JONSWAP simulations are generated by the program SeaGen (Costa T. S., Felício, Matos, & Fernandes, 2023). Figure 17 is a print screen of the used, 100 square meter JONSWAP model which setup is defined in Figure 18.

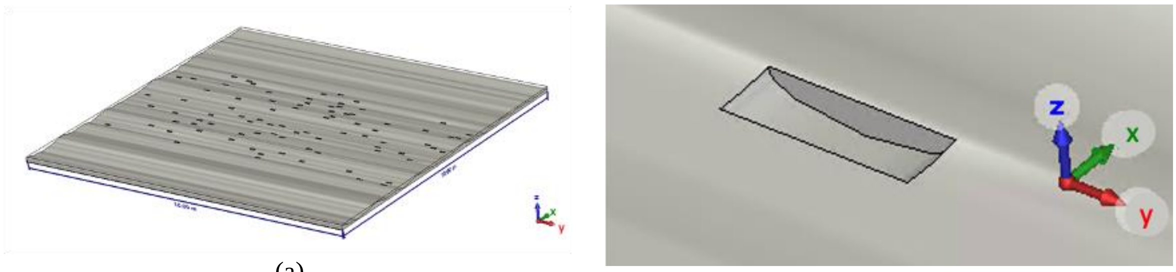

(a) (b)

Figure 17 – 100 square meter JONSWAP model with 84 bottles [10 g/m$^2$], $H_s = 9\ cm$. (a) JONSWAP Model Setup measuring 100 square meter; (b) JONSWAP Model Setup bottles indentation.

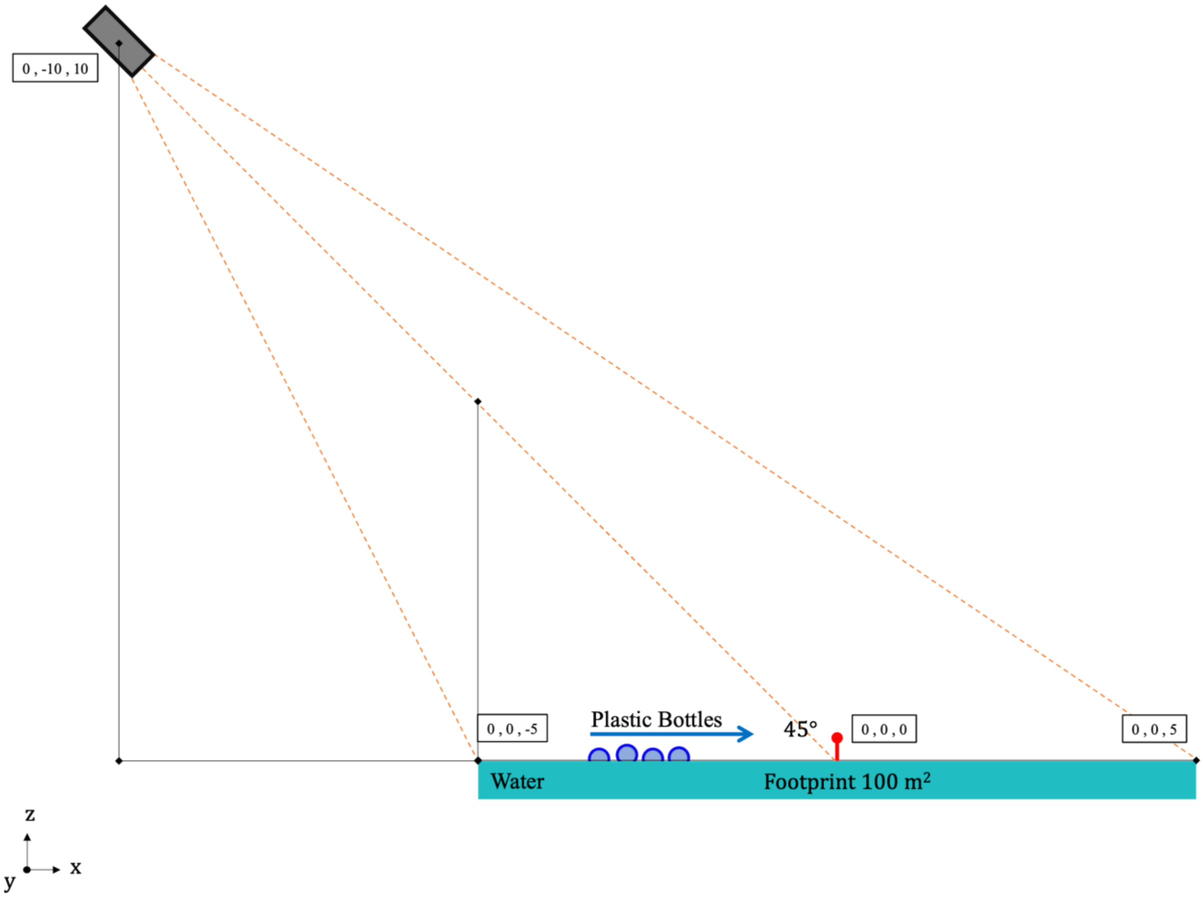

Figure 18 - JONSWAP Model Setup, by SeaGen (Costa T. S., Felício, Matos, & Fernandes, 2023). Dimensions are in meters.

## 3.2. BRAGG PEAK BEHAVIOUR AND OBSERVATION AZIMUTH ANGLE

This section will study the Bragg peak under different observation azimuth angle, $\varphi = 0°$, $\varphi = 45°$ and $\varphi = 90°$. In this study figures were created from Sinusoidal Model Setup with 1.5 square meter and 100 square meter. As mentioned in Section 2.2 $f_{Bragg(predicted)}$ is the frequency where there is a coherent sum of energy acquired by equation [1]. $f_{Bragg} = 6$ GHz is the actual simulated frequency of the coherent sum of energy.

In Figure 19 and also in Figure 20, if $\varphi = 0°$, a peak, which has its location $f_{Bragg} = 6$ GHz, is clear, result in line with equation [1]. $\varphi = 0°$, is the "ideal" condition for the Bragg Effect, where the observation antenna is directly facing the waves crests. Here $f_{Bragg(predicted)} = f_{Bragg} = 6$ GHz. The ray tracing for $\varphi = 0°$ can be seen in Figure 21. If $\varphi = 45°$, instead of a predicted $f_{Bragg(predicted)} = 6$ GHz, based on the conditions from equation [1], the coherent sum appears on a different location, in a higher frequency $f_{Bragg} = 8.5$ GHz. Also, the energy level is much lower than when $\varphi = 0°$. The ray tracing is in Figure 22. With waves facing the model from $\varphi = 90°$, there is an absence of the Bragg effect since there are none repeated wave crests facing the antenna beam. The scattered energy level in this case is, however, closer to $\varphi = 0°$. The plotted wave appears to be a stationary wave. Ray tracing for $\varphi = 90°$ in Figure 22.

According to equation [1], Bragg effect is dependent on the incident angle $\theta$ (Bragg angle), however, according to this analysis the effect also azimuth, $\varphi$, dependent and not exclusively dependent by $\theta$. The peak where the energy coherent sum happens, increased from $f_{Bragg(predicted)} = 6$ GHz to $f_{Bragg} = 8.5$ GHz as the azimuth angle increases from $\varphi = 0°$ to $\varphi = 45°$. Also, with the change of azimuth angle from $\varphi = 0°$ to $\varphi = 45°$ the magnitude of the peak in $f_{Bragg}$ have significantly decreased.

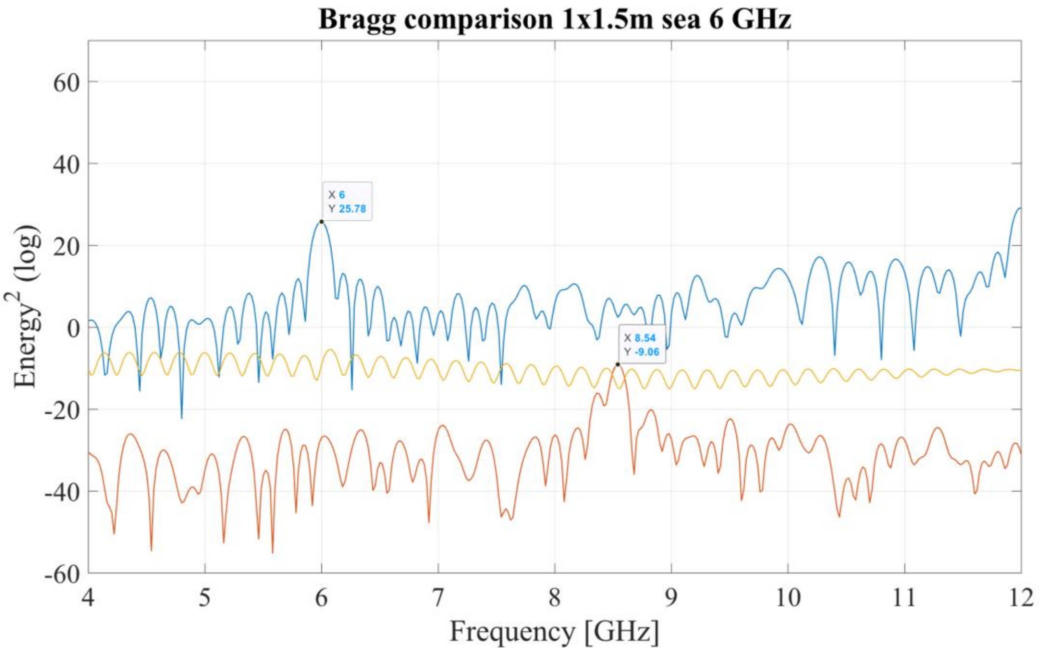

Figure 19 - Energy over frequency for a $f_{Bragg(predicted)} = 6$ GHz in the absence of litter in the Sinusoidal Model Setup with 1.5 square meter for $\varphi = 0$ for $\varphi = 45°$, and for $\varphi = 90°$

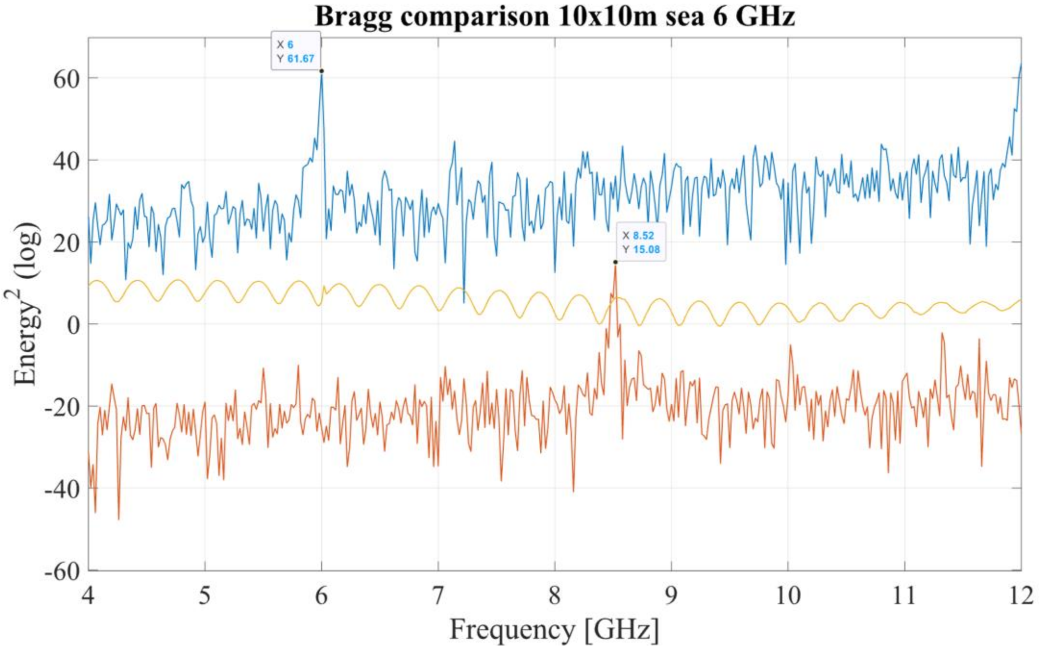

Figure 20 - Energy over frequency for a $f_{Bragg(predicted)} = 6$ GHz in the absence of litter in the Sinusoidal Model Setup with 10 square meter for $\varphi = 0$ for $\varphi = 45°$, and for $\varphi = 90°$

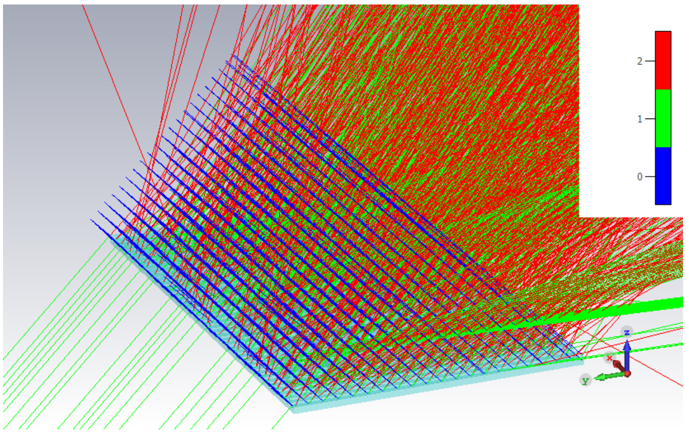

Figure 21 - Bragg peak ray tracing for a $f_{Bragg(predicted)} = 6$ GHz in the absence of litter in the Sinusoidal Model Setup with 1.5 square meter, $\varphi = 0°$ (blue – incident rays, green, single bounced rays, red – double bounced rays).

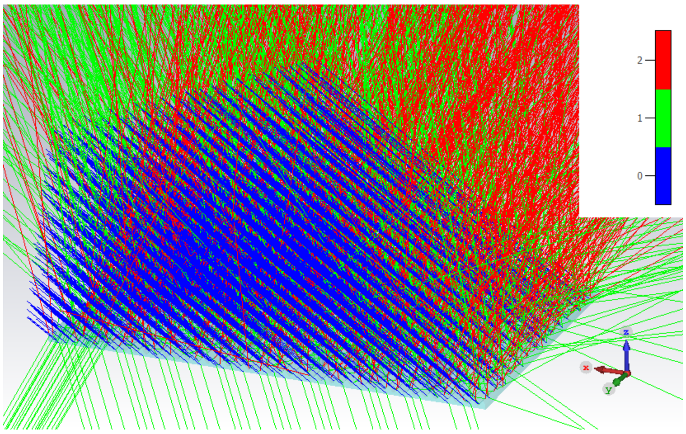

Figure 22- Bragg peak ray tracing for a $f_{Bragg(predicted)} = 6$ GHz in the absence of litter in the Sinusoidal Model Setup with 1.5 square meter, $\varphi = 45°$ (blue – incident rays, green, single bounced rays, red – double bounced rays).

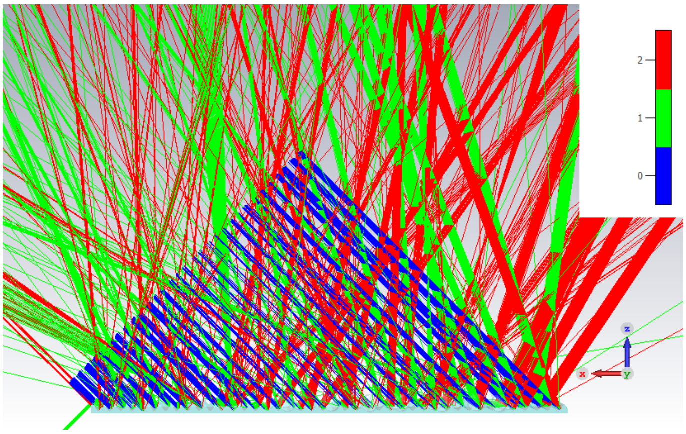

Figure 23 - Bragg peak ray tracing for a $f_{Bragg(predicted)} = 6$ GHz in the absence of litter in the Sinusoidal Model Setup with 1.5 square meter, $\varphi = 90°$ (blue – incident rays, green, single bounced rays, red – double bounced rays).

## 3.3. BRAGG PEAK BEHAVIOUR AND LITTER CONCENTRATION

This section studies the influence of concentration on the Bragg peak, quantified through the metric PR, previously introduced on Section 2.4. Expressing the peak reduction in terms of concentration or populated area is visually the same, because both measures, concentration, and populated area, are proportional to the number of bottles. As the Bragg peak's frequency, $f_{Bragg}$ is difficult to predict at $\varphi = 45°$ and $\varphi = 90°$, this study only addresses the observation azimuth angle, $\varphi = 0°$. To offer a wide range and variety of results the models used models are 100 square meter for $f_{Bragg} = 6$ GHz, 1.5 square meter for $f_{Bragg} = 6$ GHz and 1.5 square meter for $f_{Bragg} = 6$ GHz from the Sinusoidal Model Setup[9].

The results from the tests found a relation between the reduction of the peak, PR and the concentration of the litter. The results were summarised in Figure 24. With an increment of the concentration, the peak reduction increases. The more added bottles, the bigger is the distance between the $f_{Bragg(0\ bottles)}$ and the $f_{Bragg(b\ bottles)}$, where $b$ is the number of bottles from a certain measurement. If comparing PR to plastic bottles concentration, appear to exist a proportional dependence between the number of added bottles and the reduction of Bragg's peak. That relation can be seen in Figure 24, where all lines have a similar slope. For the 100 square meter model, a trendline was added, so that the slopes can be compared despite the scale, due to the huge difference of concentrations.

The concentration increasement appears to be related to Bragg's PR. The greater the concentration, the greater the PR. The PR metric is not, however, clear enough to be used as a litter detection metric as this study is restricted to a very controlled situation. Eventually in some SAR technique this metric might be useful.

---

[9] 100 square meter for $f_{Bragg} = 10$ GHz Sinusoidal Model simulation was not performed due to computational limitations.

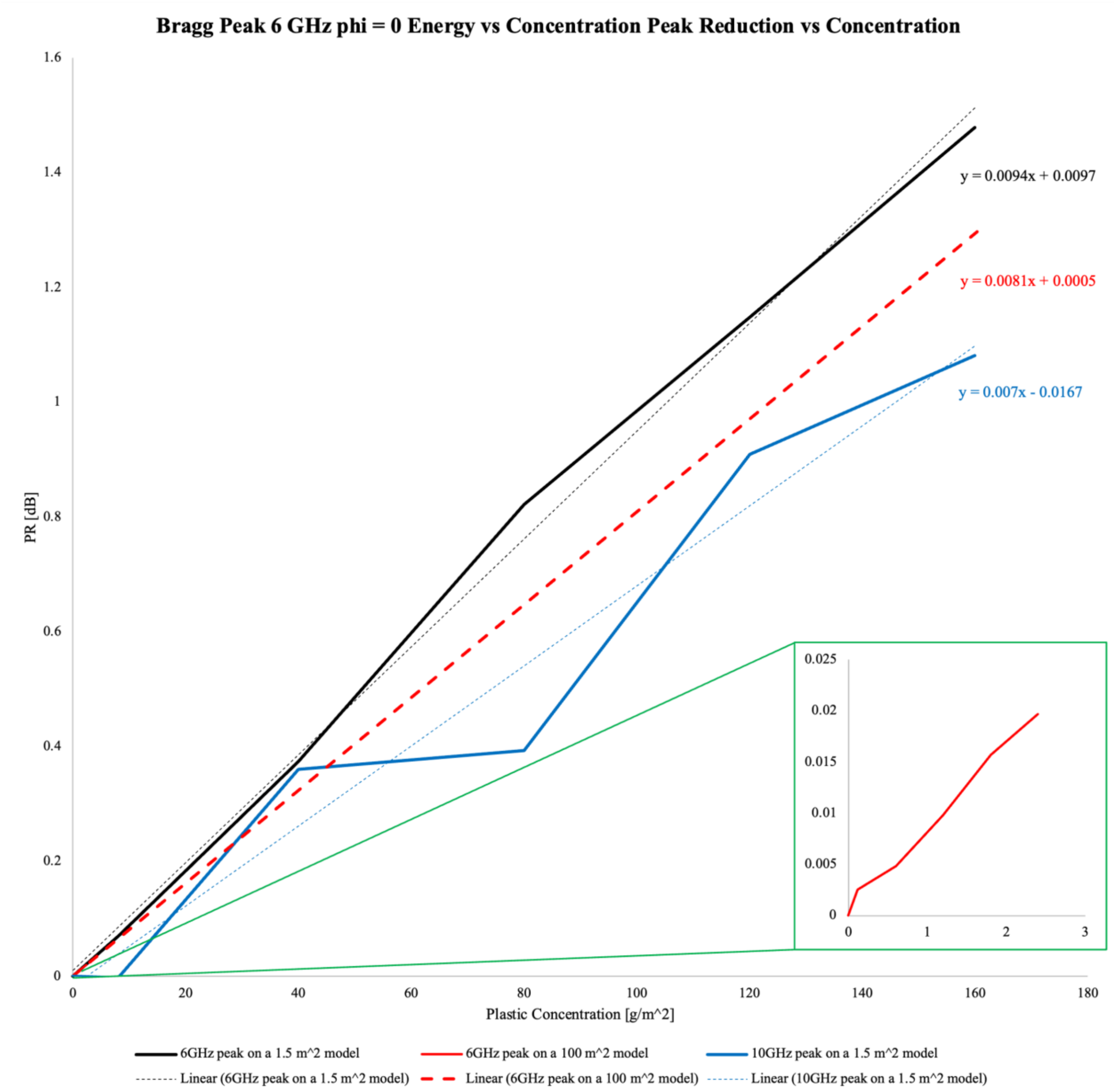

Figure 24 - PR/C relation in a Sinusoidal Model Setup, through different concentrations measurements with deferent $f_{Bragg}$ and model size, $\varphi = 0^{\circ}$[10].

---

[10] The red dashed line is the trendline for 100m$^2$ dataset. This happens because the 100m$^2$ allows much lower concentrations. The actual data for that measurement is in the auxiliary plot with a full red line at the lower right corner of Figure 24.

# 3.4. PLASTIC DETECTION UNDER THE BRAGG EFFECT

In Section 3.2 the was studied behaviour of the Bragg peak under a variation of the azimuth angle, in Section 3.3 Bragg peak was analysed under deferent concentrations. In this section the objective is to identify the level of litter detection under the Bragg effect, varying the litter concentration and the azimuth angle of observation. This section uses the Sinusoidal Model Setup with 1.5 square meter for $f_{Bragg} = 6$ GHz.

Table 4 quantifies the energy in logarithmic units over concentration, for the azimuth angle, $\varphi = 0°$, $\varphi = 45°$ and $\varphi = 90°$ at deferent sub bands. As already referred, a wider band means more energy, and with the increase of concentration, the more energy in scattered too.

However, when comparing sub bands with the same length such as $\Delta f' = [11.5; 12]\ GHz$, $\Delta f'' = [9.75; 10.25]\ GHz$ and $\Delta f''' = [8; 8.5]\ GHz$ the energy level is not the same. An answer for $E'_{\Delta f} > E''_{\Delta f} > E'''_{\Delta f}$ is the Bragg effect's peak. As $f_{Bragg} = 6\ GHz$, the peak is located inside $\Delta f'$ (second peak $f_{Bragg} = 12\ GHz$) which causes the energy increase. Also, $\Delta f''$ is a little closer to $f_{Bragg} = 12\ GHz$ than $\Delta f'''$ is to $f_{Bragg} = 6\ GHz$, wich explains $E''_{\Delta f} > E'''_{\Delta f}$. When $\varphi = 45$ the same happens, however $f_{Bragg} = 8.5\ GHz$ must be considered as observed in Section 3.2. $E''_{\Delta f} < E'''_{\Delta f}$ and $E'_{\Delta f} < E'''_{\Delta f}$ because the peak is now located inside $\Delta f'''$. If $\varphi = 90$ the effect is absent, therefore $E'_{\Delta f} \approx E''_{\Delta f} \approx E'''_{\Delta f}$.

|  |  | **Energy [dB]** |  |  |  |  |  |  |  |  |
|---|---|---|---|---|---|---|---|---|---|---|
|  | Number of Bottles | 0 | 1 | 2 | 3 | 4 | 5 | 10 | 15 | 20 |
|  | Model Area [m^2] | 1.5 | 1.5 | 1.5 | 1.5 | 1.5 | 1.5 | 1.5 | 1.5 | 1.5 |
|  | Concentration [g/m^2] | 0 | 8 | 16 | 24 | 32 | 40 | 80 | 120 | 160 |
|  | Plastic Populated Area | 0.00% | 0.58% | 1.16% | 1.75% | 2.33% | 2.91% | 5.82% | 8.74% | 11.65% |
| phi = 0 | 11.50 - 12.00 GHz | 3.2 | 3.2 | 3.2 | 3.2 | 3.2 | 3.2 | 3.1 | 3.1 | 3.1 |
|  | 9.75 - 10.25 GHz | 2.5 | 2.5 | 2.5 | 2.5 | 2.5 | 2.5 | 2.5 | 2.4 | 2.4 |
|  | 8.00 - 8.50 GHz | 2.2 | 2.2 | 2.2 | 2.2 | 2.2 | 2.2 | 2.2 | 2.2 | 2.2 |
|  | 4.00 - 8.00 GHz | 4.2 | 4.2 | 4.2 | 4.2 | 4.2 | 4.2 | 4.2 | 4.1 | 4.1 |
|  | 8.00 - 12.00 GHz | 3.7 | 3.7 | 3.7 | 3.7 | 3.7 | 3.7 | 3.6 | 3.6 | 3.5 |
|  | 4.00 - 12.00 GHz | 4.1 | 4.1 | 4.1 | 4.1 | 4.0 | 4.0 | 4.0 | 4.0 | 4.0 |
| phi = 45 | 11.50 - 12.00 GHz | -1.2 | -1.0 | -1.0 | -0.8 | -0.8 | -0.8 | -0.7 | -0.6 | -0.5 |
|  | 9.75 - 10.25 GHz | -1.2 | -1.0 | -0.9 | -0.9 | -0.8 | -0.8 | -0.8 | -0.6 | -0.7 |
|  | 8.00 - 8.50 GHz | -0.5 | -0.5 | -0.4 | -0.3 | -0.2 | -0.3 | -0.1 | 0.1 | 0.0 |
|  | 4.00 - 8.00 GHz | -0.5 | -0.4 | -0.3 | -0.2 | -0.2 | -0.1 | 0.1 | 0.3 | 0.3 |
|  | 8.00 - 12.00 GHz | 0.1 | 0.2 | 0.2 | 0.3 | 0.4 | 0.4 | 0.4 | 0.5 | 0.5 |
|  | 4.00 - 12.00 GHz | 1.1 | 1.1 | 1.1 | 1.2 | 1.2 | 1.2 | 1.2 | 1.2 | 1.2 |
| phi = 90 | 11.50 - 12.00 GHz | -1.0 | -0.8 | -0.6 | -0.5 | -0.5 | -0.6 | -0.4 | -0.4 | -0.3 |
|  | 9.75 - 10.25 GHz | -0.9 | -0.9 | -0.7 | -0.7 | -0.4 | -0.4 | -0.2 | -0.2 | -0.4 |
|  | 8.00 - 8.50 GHz | -0.8 | -0.8 | -0.6 | -0.5 | -0.5 | -0.4 | -0.2 | -0.2 | -0.3 |
|  | 4.00 - 8.00 GHz | -0.2 | 0.1 | 0.2 | 0.3 | 0.3 | 0.4 | 0.5 | 0.7 | 0.8 |
|  | 8.00 - 12.00 GHz | -0.8 | -0.4 | -0.2 | 0.0 | 0.2 | 0.2 | 0.5 | 0.5 | 0.7 |
|  | 4.00 - 12.00 GHz | -0.7 | 0.0 | 0.2 | 0.3 | 0.4 | 0.5 | 0.6 | 0.7 | 0.9 |

Table 4 - Energy table under $f_{Bragg(predicted)} = 6$ GHz in Sinusoidal Model Setup with 1.5 square meter under deferent concentrations for $\varphi = 0°$, $\varphi = 45°$, and $\varphi = 90°$

The same collection of results from the previous table can be organized with the EnR coefficient. In Table 5, for $\varphi = 0°$ there is a notorious decrease of the EnR with the increment of concentration. This happens due to the Bragg's effect intensity. For $\varphi = 45°$ and $\varphi = 90°$ that behaviour is not noticeable as the Bragg effect there is less intense, as concluded in Section 3.2. Higher EnR values are linked to a corner effect experienced when the observation angles are $\varphi = 45°$ and $\varphi = 90°$ due to the bottle's indentation cylindrical shape.

| | | | | **EnR** | | | | | |
|---|---|---|---|---|---|---|---|---|---|
| | Number of Bottles | 1 | 2 | 3 | 4 | 5 | 10 | 15 | 20 |
| | Model Area [m^2] | 1.5 | 1.5 | 1.5 | 1.5 | 1.5 | 1.5 | 1.5 | 1.5 |
| | Concentration [g/m^2] | 8 | 16 | 24 | 32 | 40 | 80 | 120 | 160 |
| | Plastic Populated Area | 0.58% | 1.16% | 1.75% | 2.33% | 2.91% | 5.82% | 8.74% | 11.65% |
| phi = 0 | 11.50 - 12.00 GHz | 1.0 | 1.0 | 0.9 | 0.9 | 0.9 | 0.8 | 0.8 | 0.7 |
| | 9.75 - 10.25 GHz | 1.0 | 1.0 | 1.0 | 0.9 | 1.0 | 0.9 | 0.9 | 0.8 |
| | 8.00 - 8.50 GHz | 1.0 | 1.0 | 1.0 | 1.0 | 1.0 | 1.0 | 0.8 | 0.9 |
| | 4.00 - 8.00 GHz | 1.0 | 1.0 | 1.0 | 0.9 | 0.9 | 0.9 | 0.8 | 0.8 |
| | 8.00 - 12.00 GHz | 1.0 | 1.0 | 0.9 | 0.9 | 0.9 | 0.9 | 0.8 | 0.7 |
| | 4.00 - 12.00 GHz | 1.0 | 1.0 | 0.9 | 0.9 | 0.9 | 0.9 | 0.8 | 0.8 |
| phi = 45 | 11.50 - 12.00 GHz | 1.4 | 1.6 | 2.3 | 2.3 | 2.2 | 3.4 | 3.8 | 4.3 |
| | 9.75 - 10.25 GHz | 1.4 | 1.6 | 1.7 | 2.0 | 2.2 | 2.0 | 3.2 | 3.1 |
| | 8.00 - 8.50 GHz | 1.1 | 1.2 | 1.5 | 1.9 | 1.6 | 2.3 | 3.5 | 3.3 |
| | 4.00 - 8.00 GHz | 1.5 | 1.9 | 2.3 | 2.3 | 2.7 | 4.0 | 6.4 | 7.5 |
| | 8.00 - 12.00 GHz | 1.2 | 1.3 | 1.5 | 1.8 | 2.0 | 2.2 | 2.6 | 2.8 |
| | 4.00 - 12.00 GHz | 1.1 | 1.1 | 1.2 | 1.3 | 1.4 | 1.3 | 1.4 | 1.3 |
| phi = 90 | 11.50 - 12.00 GHz | 1.5 | 2.5 | 3.3 | 2.9 | 2.5 | 3.8 | 3.8 | 4.9 |
| | 9.75 - 10.25 GHz | 1.1 | 1.8 | 1.7 | 3.2 | 3.3 | 5.9 | 5.3 | 3.5 |
| | 8.00 - 8.50 GHz | 1.2 | 1.7 | 2.0 | 2.5 | 2.9 | 4.6 | 4.0 | 3.9 |
| | 4.00 - 8.00 GHz | 1.8 | 2.5 | 3.3 | 3.3 | 3.8 | 4.8 | 7.5 | 10.8 |
| | 8.00 - 12.00 GHz | 2.7 | 4.3 | 6.4 | 9.0 | 10.3 | 18.1 | 19.9 | 29.8 |
| | 4.00 - 12.00 GHz | 4.1 | 6.9 | 9.3 | 10.9 | 12.8 | 18.7 | 22.8 | 35.0 |

Table 5 - EnR table under $f_{Bragg(predicted)} = 6$ GHz in Sinusoidal Model Setup with 1.5 square meter under deferent concentrations for $\varphi = 0°$, $\varphi = 45°$, and $\varphi = 90°$

The following figures Figure 25(a), Figure 26(a) and Figure 27(a), express the Energy in dB's along a plastic concentration increase performed on a sinusoidal synthetic sea model to induce a $f_{Bragg(predicted)} = 6$ GHz for $\varphi = 0°$, $\varphi = 45°$, and $\varphi = 90°$, respectively. The conclusions are the same already taken from the Table 4 analysis. In a same manner, Figure 25(b), Figure 26(b) and Figure 27(b) , express the EnR coefficient along a plastic concentration increase for $\varphi = 0°$, $\varphi = 45°$, and $\varphi = 90°$, respectively, assuring conclusions taken with Table 5.

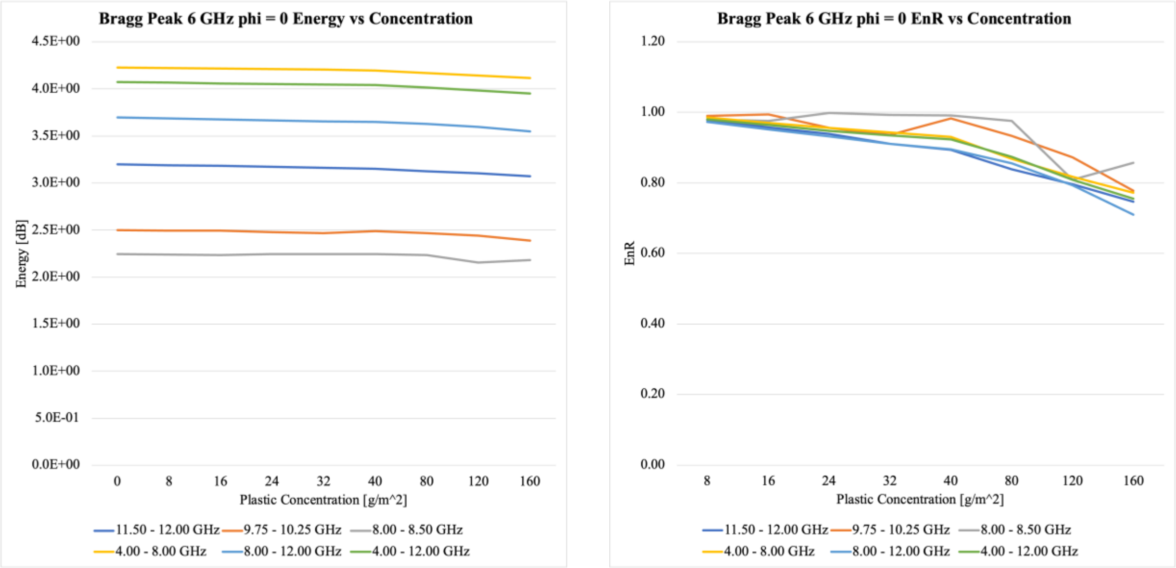

(a) (b)

Figure 25 - Energy over frequency for a $f_{Bragg(predicted)} = 6$ GHz under different litter concentrations in the Sinusoidal Model Setup with 1.5 square meter for $\varphi = 0°$. (a) Energy over plastic concentration; (b) EnR over plastic concentration

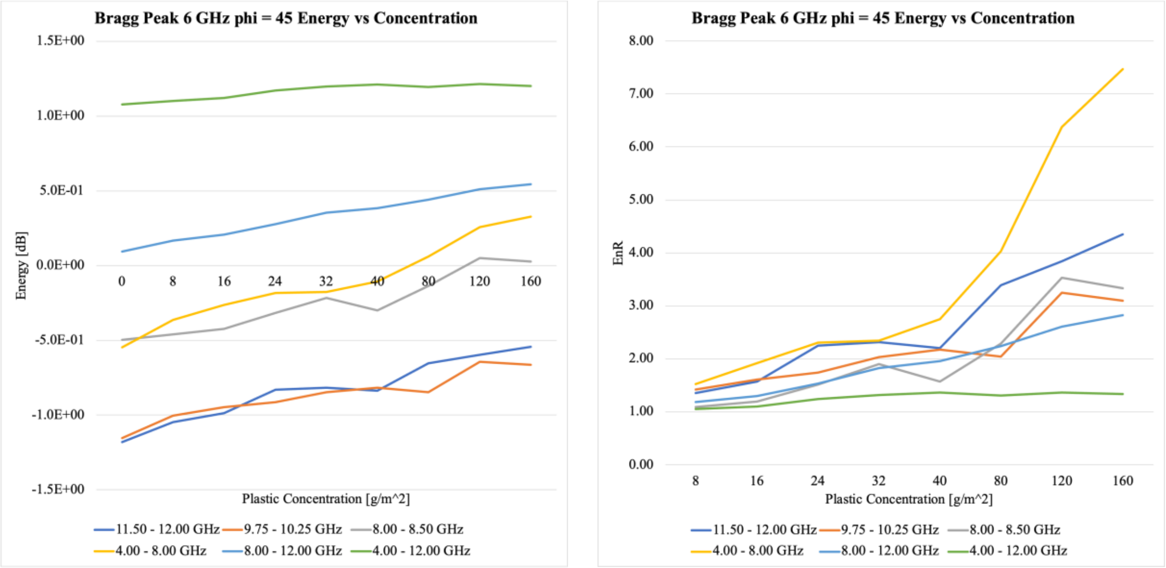

(a) (b)

Figure 26 - Energy over frequency for a $f_{Bragg(predicted)} = 6$ GHz under different litter concentrations in the Sinusoidal Model Setup with 1.5 square meter for $\varphi = 45°$. (a) Energy over plastic concentration; (b) EnR over plastic concentration

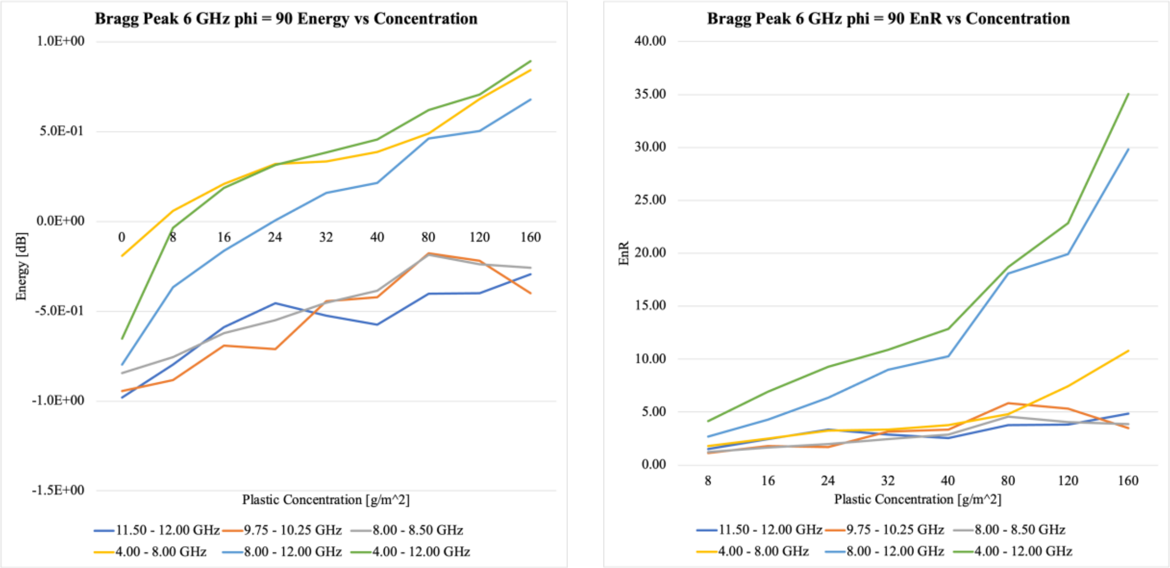

(a) (b)

Figure 27 - Energy over frequency for a $f_{Bragg(predicted)} = 6$ GHz under different litter concentrations in the Sinusoidal Model Setup with 1.5 square meter for $\varphi = 90°$. (a) Energy over plastic concentration; (b) EnR over plastic concentration.

Figure 28 contains the waterfalls for 20 plastic bottles. The dashed red zone identifies the location where the bottles are predicted to appear. In Figure 21(a) that zone is less intense than others, which is in line with the 'inverse' behaviour for a Bragg effect with $\varphi = 0°$. Also, the difference in the azimuth angles is clear. Bottles trace the waterfall with the distance, $d$ increasement. In Figure 28(a), for $\varphi = 0°$ bottles move towards the observation antenna faster they do in Figure 28(b), where $\varphi = 45°$, which make sense regarding the observation angle. In Figure 28(c), where $\varphi = 90°$, the bottles distance, $d$ from the observer is constant, as they move across the $x$ axis, in the negative direction, "to the left" from the antenna's point of view.

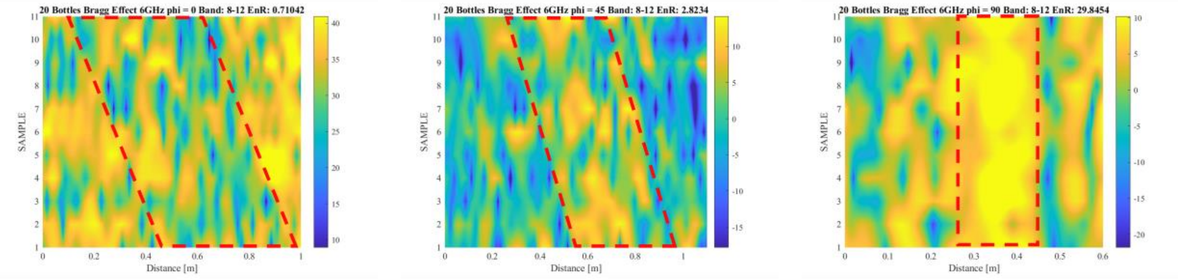

(a) (b) (c)

Figure 28 - Waterfalls $I_{ij}^{litter}(d,t)$ for a $f_{Bragg(predicted)} = 6$ GHz 20 plastic bottles [160 g/m2] in the Sinusoidal Model Setup with 1.5 square meter with the predicted location where the bottles should appear. (a) $\varphi = 0°$; (b) $\varphi = 45°$; (c) $\varphi = 90°$.

## 3.5. DETECTION UNDER A JONSWAP MODEL

The last section in Chapter 3 regards the use of SeaGen (Costa T. S., Felício, Matos, & Fernandes, 2023) to create a JONSWAP surface with floating plastic bottles. This setup was previously introduced in Section 3.1.8. JONSWAP with 100 square meter is closer to a scenario where the antenna is inhaled on an aircraft. The JONSWAP tests permit identify if the developed metrics are also applied to wider scaled environments.

The simulations in this section were limited to the capacity of the available hardware to deliver the results in an acceptable period of time. Therefore, the only simulation performed is a surface with 100 square meter simulated for $\varphi = 0°$, $\varphi = 45°$ and $\varphi = 90°$. For the reference 801 samples were acquired, while for the litter measurements 41 were considered. The simulation was performed with 40 bottles, which match a concentration is 4.8 g/m$^2$ and 0.35% of the model area, same as the footprint area, covered. The water height of $H_s = 9\ cm$.

| **Energy [dB]** | phi = 0 | phi = 45 | phi = 90 |
|---|---|---|---|
| Number of Bottles | 40 | 40 | 40 |
| Model Area [m^2] | 100 | 100 | 100 |
| Concentration [g/m^2] | 4.8 | 4.8 | 4.8 |
| Plastic Populated Area | 0.35% | 0.35% | 0.35% |
| 11.50 - 12.00 GHz | 1.7 | -2.4 | -0.9 |
| 9.75 - 10.25 GHz | 1.8 | -2.3 | -0.8 |
| 8.00 - 8.50 GHz | 1.9 | -2.5 | -0.8 |
| 4.00 - 8.00 GHz | 2.9 | -1.5 | -0.9 |
| 8.00 - 12.00 GHz | 2.7 | -1.4 | -0.6 |
| 4.00 - 12.00 GHz | 3.1 | -1.3 | -0.2 |

Table 6 - Energy of the simulation performed in JONSWAP Model SetupSinusoidal Model Setup with 100 square meter, plastic bottles [10g/m$^2$], $H_s = 9\ cm$, for $\varphi = 0°$, $\varphi = 45°$ and $\varphi = 90°$

| **EnR** | phi = 0 | phi = 45 | phi = 90 |
|---|---|---|---|
| Number of Bottles | 40 | 40 | 40 |
| Sin Model Sea Area [m^2] | 100 | 100 | 100 |
| Plastic Concentration [g/m^2] | 4.8 | 4.8 | 4.8 |
| Plastic Populated Area | 0.35% | 0.35% | 0.35% |
| 11.50 - 12.00 GHz | 9.5 | 115.1 | 12.0 |
| 9.75 - 10.25 GHz | 9.6 | 94.4 | 12.8 |
| 8.00 - 8.50 GHz | 9.7 | 80.0 | 13.5 |
| 4.00 - 8.00 GHz | 9.7 | 70.9 | 499.7 |
| 8.00 - 12.00 GHz | 9.6 | 87.9 | 832.8 |
| 4.00 - 12.00 GHz | 9.6 | 48.0 | 2009.6 |

Table 7 - EnR table of the simulation performed in JONSWAP Model SetupSinusoidal Model Setup with 100 square meter, plastic bottles [10g/m$^2$], $H_s = 9\ cm$, for $\varphi = 0°$, $\varphi = 45°$ and $\varphi = 90°$

The results in Table 6 and Table 7 are clear for $\varphi = 0°$. Wider bands mean more energy in the result, and the EnR values are approximately the same on every band and sub band. For $\varphi = 45°$ the energy lever is much lower than for $\varphi = 0°$, what is in line with the same observation in Section 3.2. $\varphi = 90°$ energy level is the lower, however the detection is very intensive. Again, the results are probably being influenced due to a corner effect on the bottles indentation, which is different from the Sinusoidal Model Setup, as seen in Figure 12(a) compared to Figure 17(b).

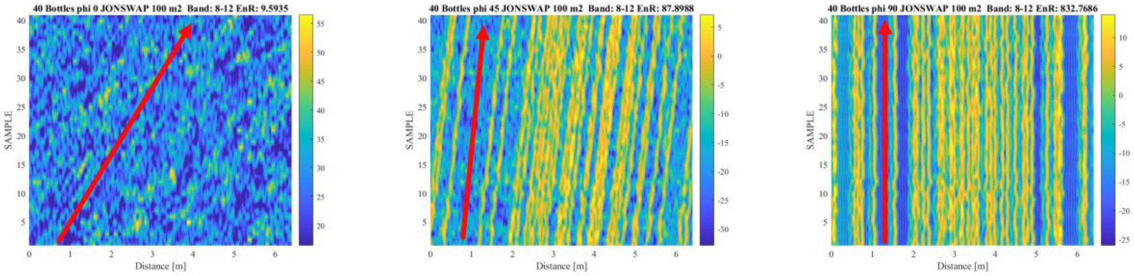

(a) (b) (c)

Figure 29 - Waterfalls $I_{ij}^{litter}(d, t)$ of the simulation performed in JONSWAP Model Setup with 100 square meter, plastic bottles [10g/m2], $H_s = 9\ cm$, X band. (a) $\varphi = 0°$; (b) $\varphi = 45°$; (c) $\varphi = 90°$. The red arrow predicts bottles' motion direction.

In Figure 29 there is a clear difference in the azimuth angles. Bottles trace the waterfall with the distance, $d$ increasement. The red arrow identifies the trace of bottles. In Figure 29(a), for $\varphi = 0°$ bottles move away from the observation antenna faster than in Figure 29(b) $\varphi = 45°$, which make sense regarding the observation angle. Also, in Figure 29(c), where $\varphi = 90°$, the bottles distance, $d$ from the observer is constant, as they move across the $x$ axis, in the positive direction, "to the right" from the antenna's point of view. These results are similar to the ones from Figure 28 in Section 3.4.

# 4. EXPERIMENTAL ANALYSIS AND DISCUSSION

After the discussion in Chapter 2, Chapter 4 discusses and introduce the results carried on the experimental setup in the Deltares' Flume. The setup is explained below, in Section 4.1. In Section 4.2, an analysis of multi-antenna performance is enrolled, and in Section 4.3, the polarimetry is discussed. This chapter assess if processing multiple antennas combinations and analysis of variations on the polarimetry emphasizes the litter response.

## 4.1. EXPERIMENTAL ANALYSIS INTODUCTION

Deltares is a research centre located in the Netherlands which is dedicated to works involving the most recent projects in the field of the water subsurface (Delft, 2022). The institute allowed "MARES" the use of the research facility named Atlantic Basin, under TUDelft's University recommendation (Van den Bremer T. , 2022), to pursue a possible solution for litter detection with remote sensing equipment. The facility, built in 2009, is a 650 square meters warehouse with a wave generator which is unique in the world. Figure 30 shows a view of the facility.

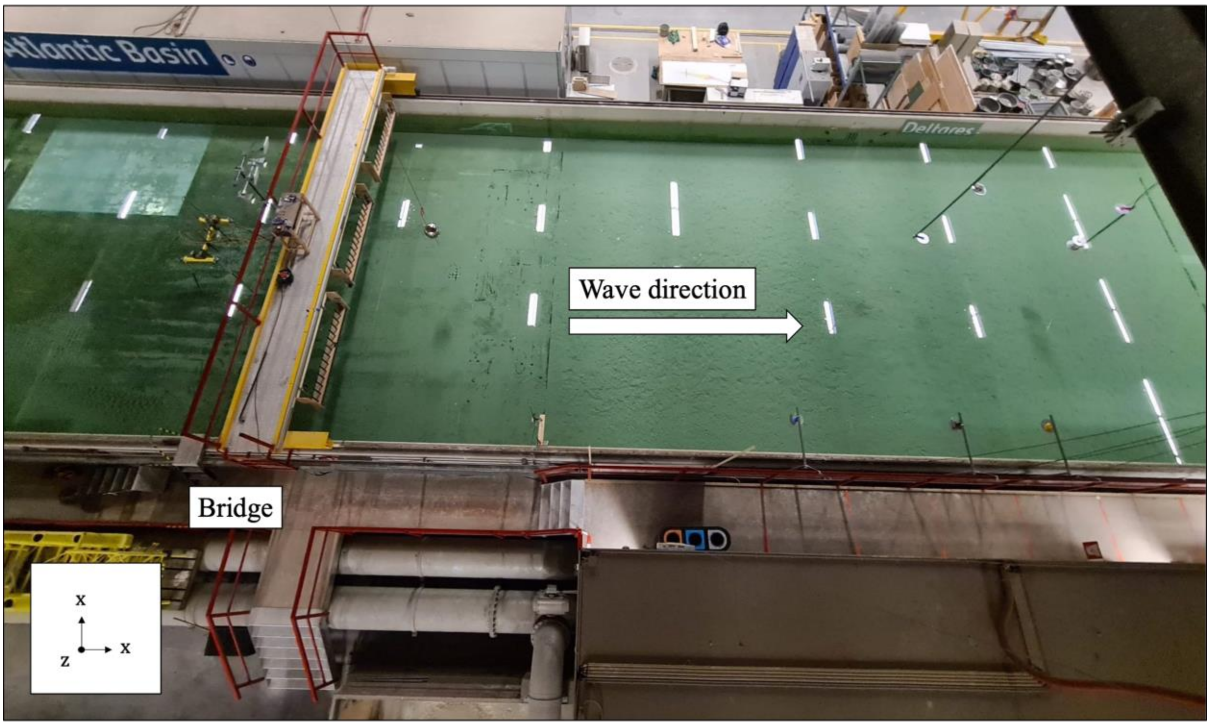

Figure 30 - Deltares wave facility ($xz$ view).

Deltares' flume is located on a covered facility which protects the experiments against external weather conditions. The water tank spans 75.0 x 8.5 meters, with a depth of 1 meter, filled with fresh water. The facility is equipped with a wave generator composed by twenty paddles which is programable via software. The waves propagate throughout the length of the water channel, throughout the $x$ axis. The wave generator is capable of source either irregular water waves up to a maximum significant height of 0.25 meters, or regular waves with a maximum wave height of 0.45 meters. At the end of the flume is found a structure that absorbs the waves generated so that destructive reflected water waves are prevented. The following figures show the setup in different views. A top view in Figure 31 and side views in Figure 32 and Figure 33.

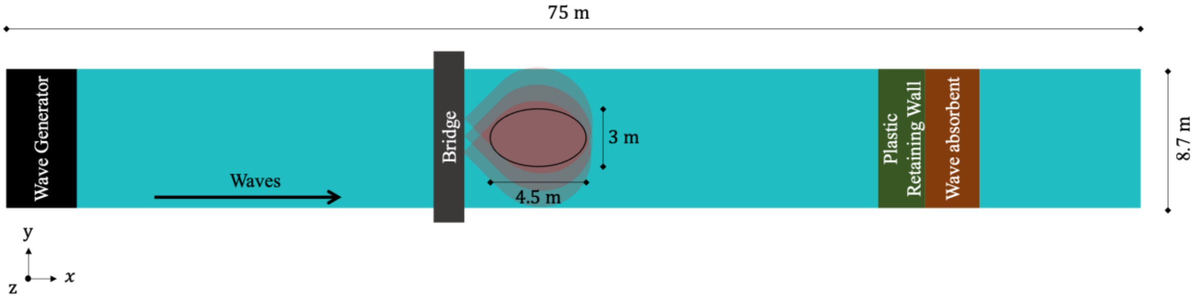

Figure 31 - Deltares wave facility setup ($xy$ view).

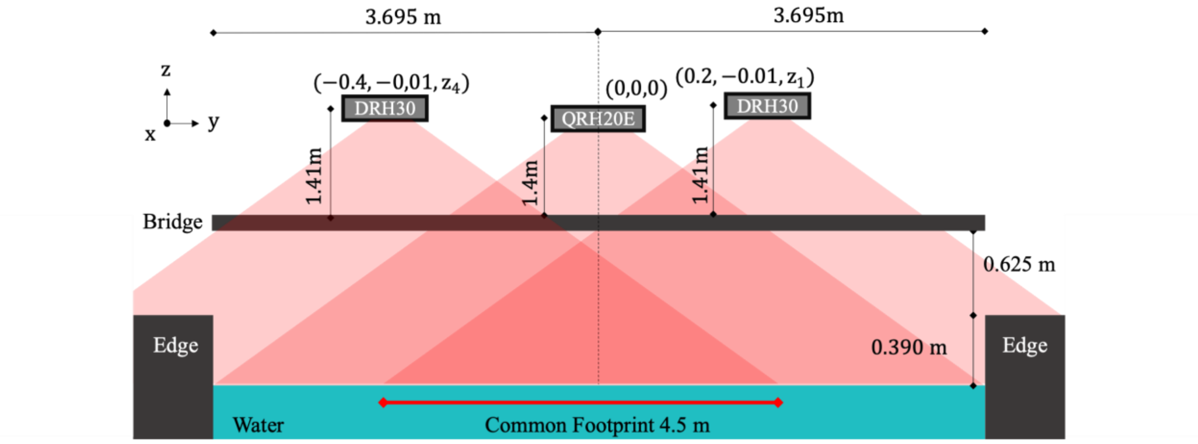

Figure 32 - Deltares wave facility setup ($yz$ view)

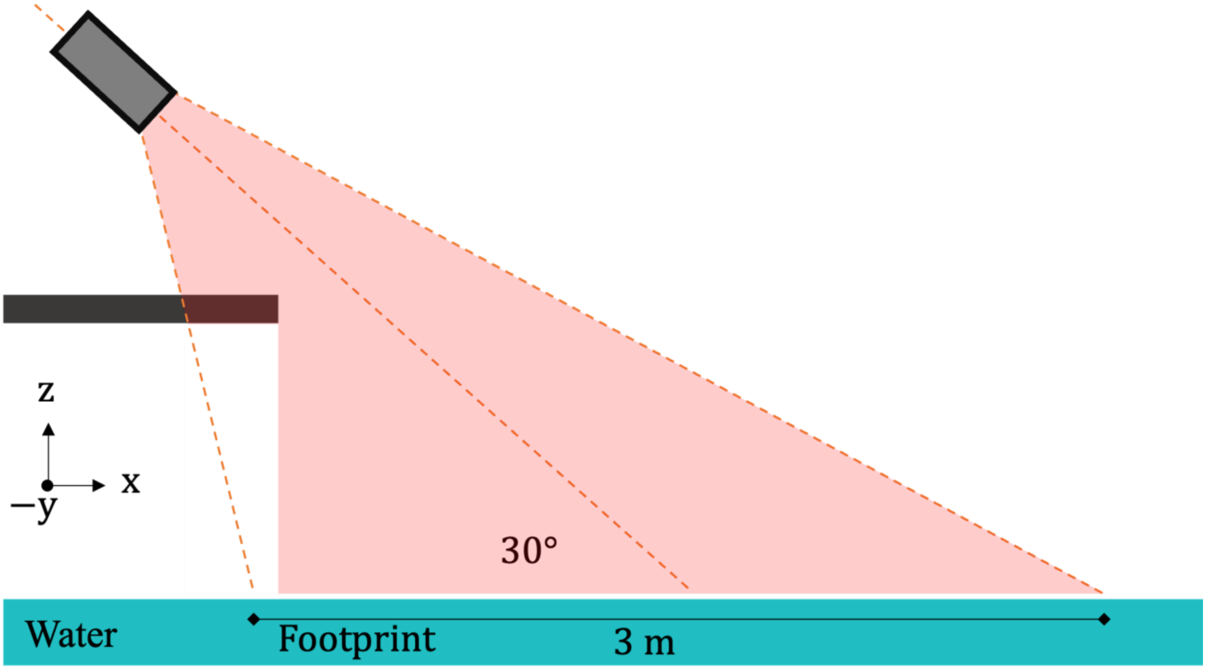

Figure 33 - Deltares wave facility setup ($yz$ view)

From an existing bridge across the flume (along the $y$ axis), 2.5 meters above the water mean level, three antennas were mounted, $N_a = 3$, arranged adjacent to each other, facing the length of the flume with $\theta = 30°$, connected to a four-port Cobalt C4420 VNA (Copper Mountain Technologies, 2022) as shown in Figure 32. The central antenna was a dual-polarization ultrawide band QRH20E (RF-SPIN, 2022), which was connected to VNA's ports 2 and 3. Two V-polarized DRH30 (RF-SPIN, 2022) antennas were also mounted according to Figure 32 and connected to the VNA ports 1 and 4. The three antennas create an elliptical footprint which dimensions are approximately 3 meters along the $y$ direction and 4.5 meters along the $x$ direction as shown in Figure 31 (Felício, et al., 2023).

Table 8 sum up the combinations of the port's configuration. Due to the BSA convention VH and HV images will always be the same, as the VNA is correctly calibrated.

| **S parameter** | **Polarization** | **Cross-pol / Co-pol** | **Antenna(s) in use** |
|---|---|---|---|
| **$S_{11}$** | **Vertical-Vertical (VV)** | **Co-pol** | **One DRH30** |
| **$S_{12}$** | **Vertical-Horizontal (VH)** | **Cross-pol** | **DRH30 and QRH20E** |
| **$S_{13}$** | **Vertical-Vertical (VV)** | **Co-pol** | **DRH30 and QRH20E** |
| **$S_{14}$** | **Vertical-Vertical (VV)** | **Co-pol** | **Two DRH30** |
| **$S_{21}$** | **Horizontal-Vertical (HV)** | **Cross-pol** | **QRH20E and DRH30** |
| **$S_{22}$** | **Horizontal-Horizontal (HH)** | **Co-pol** | **QRH20E** |
| **$S_{23}$** | **Horizontal-Vertical (HV)** | **Cross-pol** | **QRH20E** |
| **$S_{24}$** | **Horizontal-Vertical (HV)** | **Cross-pol** | **QRH20E and DRH30** |
| **$S_{31}$** | **Vertical-Vertical (VV)** | **Co-pol** | **QRH20E and DRH30** |
| **$S_{32}$** | **Vertical-Horizontal (VH)** | **Cross-pol** | **QRH20E** |
| **$S_{33}$** | **Vertical-Vertical (VV)** | **Co-pol** | **QRH20E** |
| **$S_{34}$** | **Vertical-Vertical (VV)** | **Co-pol** | **QRH20E and DRH30** |
| **$S_{41}$** | **Vertical-Vertical (VV)** | **Co-pol** | **Two DRH30** |
| **$S_{42}$** | **Vertical-Horizontal (VH)** | **Cross-pol** | **DRH30 and QRH20E** |
| **$S_{43}$** | **Vertical-Vertical (VV)** | **Co-pol** | **DRH30 and QRH20E** |
| **$S_{44}$** | **Vertical-Vertical (VV)** | **Co-pol** | **One DRH30** |

Table 8 - VNA ports configuration

The simulations frequency band, $\Delta f$, ranges from $f_{min} = 4\ GHz$ to $f_{max} = 12\ GHz$, with a step of $f_{step} = 0.04$ Hz. The simulation band contains all sub bands that will be analysed already mentioned in Table 2. Concerning the water height, both $H_s = 9\ cm$ and $H_s = 17\ cm$ irregular waves were performed with the wave generator with a period of 1.2 seconds. On the measurements a reference was recorded before.

The dataset collected in Deltares, at study, was recorded while a set of plastic polyethylene (PE) foam tubes cylinders ($\epsilon_r \sim 2.3$) that length 5 centimetres were floating on the water, the objects are in Figure 34.

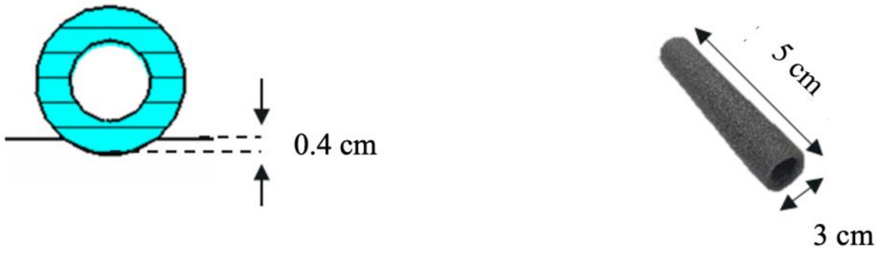

Figure 34 - PE foam tubes cylinders 5 centimetres

# 4.2. MULTI-ANTENNA PROCESSING

It was decided post process the data collected at Delft through waterfalls, as referred on Section 2.3, in an attempt of enhancing the EnR by combining the information of different antennas. Table 9 shows the backscattered energy of floating 5 cm PE tubes [10g/m$^2$], in logarithmic units. In that table, besides the single antenna's configurations, the energy of all antennas, $E_{ALL}$, the energy of a full polarization, $E_{POL}$, and the energy of only the VV antennas, $E_{ALL_{VV}}$, were added in three different columns.

| | | Energy (log) different antennas configurations 5 cm PE tubes [10g/m2], H_s= 9 cm | | | | | | | | | | | | | | | | | | |
|---|---|---|---|---|---|---|---|---|---|---|---|---|---|---|---|---|---|---|---|---|
| | S of antenna: | S11 | S12 | S13 | S14 | S21 | **S22** | **S23** | S24 | S31 | **S32** | **S33** | S34 | S41 | S42 | S43 | S44 | E All | E Pol | E VV |
| | Polarisation: | VV | VH | VV | VV | HV | **HH** | **HV** | HV | VV | **VH** | **VV** | VV | VV | VH | VV | VV | Normalized to Na | | |
| Hs = 9 cm | S: 2 - 9 | -4.3 | -5.3 | -4.5 | -4.5 | -5.3 | -4.5 | -5.1 | -5.2 | -4.5 | -5.1 | -4.4 | -4.5 | -4.6 | -5.2 | -4.5 | -4.4 | -4.6 | -4.6 | -4.5 |
| | Cu: 4 - 6 | -4.4 | -5.4 | -4.5 | -4.5 | -5.4 | -4.6 | -5.5 | -5.4 | -4.5 | -5.5 | -4.5 | -4.5 | -4.5 | -5.4 | -4.5 | -4.4 | -4.7 | -4.8 | -4.5 |
| | Ca: 6 - 8 | -4.5 | -5.5 | -4.5 | -4.5 | -5.5 | -4.7 | -5.5 | -5.5 | -4.5 | -5.5 | -4.3 | -4.5 | -4.6 | -5.6 | -4.5 | -4.5 | -4.7 | -4.7 | -4.5 |
| | Xu: 8 - 10 | -4.7 | -5.6 | -4.6 | -4.7 | -5.6 | -4.6 | -5.5 | -5.6 | -4.6 | -5.5 | -4.4 | -4.6 | -4.7 | -5.6 | -4.6 | -4.6 | -4.8 | -4.8 | -4.6 |
| | Xa: 10 - 12 | -4.9 | -5.6 | -4.9 | -4.9 | -5.6 | -4.7 | -5.6 | -5.6 | -4.9 | -5.6 | -4.8 | -4.9 | -4.9 | -5.6 | -4.9 | -4.8 | -5.0 | -5.0 | -4.9 |
| | KUu: 12 - 15 | -4.6 | -5.4 | -4.7 | -4.7 | -5.4 | -4.5 | -5.4 | -5.4 | -4.7 | -5.4 | -4.6 | -4.7 | -4.7 | -5.5 | -4.7 | -4.6 | -4.8 | -4.8 | -4.7 |
| | KUa: 15 - 18 | -4.8 | -5.4 | -4.9 | -4.9 | -5.4 | -4.6 | -5.5 | -5.4 | -4.9 | -5.6 | -4.8 | -4.9 | -4.9 | -5.5 | -4.9 | -4.7 | -5.0 | -4.9 | -4.8 |
| | K: 18 - 20 | -5.2 | -5.8 | -5.2 | -5.3 | -5.7 | -4.8 | -5.8 | -5.8 | -5.2 | -5.8 | -5.1 | -5.3 | -5.3 | -5.8 | -5.3 | -5.1 | -5.3 | -5.2 | -5.2 |
| | X: 8 -12 | -4.3 | -5.2 | -4.3 | -4.4 | -5.2 | -4.3 | -5.2 | -5.2 | -4.3 | -5.2 | -4.2 | -4.3 | -4.4 | -5.2 | -4.3 | -4.3 | -4.5 | -4.5 | -4.3 |
| | ALL: 2 - 20 | -3.6 | -4.5 | -3.6 | -3.6 | -4.5 | -3.6 | -4.5 | -4.5 | -3.6 | -4.5 | -3.5 | -3.6 | -3.7 | -4.5 | -3.6 | -3.5 | -3.8 | -3.8 | -3.6 |
| Hs = 17 cm | S: 2 - 9 | -4.4 | -5.4 | -4.6 | -4.6 | -5.4 | -4.6 | -5.2 | -5.3 | -4.6 | -5.2 | -4.4 | -4.6 | -4.6 | -5.3 | -4.6 | -4.5 | -4.7 | -4.7 | -4.5 |
| | Cu: 4 - 6 | -4.7 | -5.8 | -4.8 | -4.9 | -5.8 | -4.9 | -5.8 | -5.8 | -4.8 | -5.8 | -4.8 | -4.8 | -4.8 | -5.8 | -4.8 | -4.7 | -5.0 | -5.1 | -4.8 |
| | Ca: 6 - 8 | -4.7 | -5.8 | -4.7 | -4.8 | -5.8 | -4.9 | -5.7 | -5.8 | -4.7 | -5.7 | -4.6 | -4.7 | -4.8 | -5.8 | -4.7 | -4.8 | -4.9 | -5.0 | -4.7 |
| | Xu: 8 - 10 | -5.0 | -5.9 | -4.9 | -5.0 | -5.9 | -4.9 | -5.7 | -5.9 | -4.9 | -5.8 | -4.8 | -5.0 | -5.0 | -5.9 | -5.0 | -5.0 | -5.1 | -5.1 | -4.9 |
| | Xa: 10 - 12 | -5.2 | -5.9 | -5.2 | -5.3 | -5.9 | -5.1 | -5.8 | -5.9 | -5.2 | -5.8 | -5.2 | -5.2 | -5.2 | -5.9 | -5.3 | -5.2 | -5.3 | -5.3 | -5.2 |
| | KUu: 12 - 15 | -5.0 | -5.7 | -5.0 | -5.0 | -5.7 | -4.8 | -5.7 | -5.8 | -5.0 | -5.7 | -5.0 | -5.1 | -5.0 | -5.7 | -5.1 | -4.9 | -5.1 | -5.1 | -5.0 |
| | KUa: 15 - 18 | -5.2 | -5.8 | -5.3 | -5.3 | -5.7 | -4.9 | -5.8 | -5.8 | -5.3 | -5.8 | -5.1 | -5.3 | -5.3 | -5.8 | -5.3 | -5.1 | -5.3 | -5.2 | -5.2 |
| | K: 18 - 20 | -5.5 | -6.0 | -5.7 | -5.7 | -6.0 | -5.1 | -6.1 | -6.1 | -5.6 | -6.1 | -5.5 | -5.7 | -5.6 | -6.1 | -5.7 | -5.4 | -5.6 | -5.5 | -5.6 |
| | X: 8 -12 | -4.7 | -5.5 | -4.7 | -4.8 | -5.5 | -4.7 | -5.5 | -5.5 | -4.7 | -5.5 | -4.6 | -4.7 | -4.7 | -5.5 | -4.7 | -4.7 | -4.9 | -4.9 | -4.7 |
| | ALL: 2 - 20 | -4.0 | -4.8 | -4.0 | -4.1 | -4.8 | -3.9 | -4.8 | -4.8 | -4.0 | -4.8 | -3.9 | -4.0 | -4.0 | -4.8 | -4.0 | -4.0 | -4.2 | -4.2 | -4.0 |

Table 9 - Energy values collection for floating 5 cm PE tubes [10g/m$^2$], in logarithmic units.

In Table 9 we observe that a higher energy level depends mainly on the chosen band, as wider bands contain more energy. If comparing both $Hs = 9\ cm$ and $Hs = 17\ cm$, the lower water level is the one which is more energetic, what was expected since lower water levels are closer to the "ideal" situation of a flat scattering reflector. It is also possible to notice that co-polarisations have more energy than cross-polarisations what can be confirmed in Figure 35, where the energy information is plotted over the frequency. Also, to retain that single VV polarisations showed the more energetic, which justifies the mentioned $E_{ALL_{VV}}$ column.

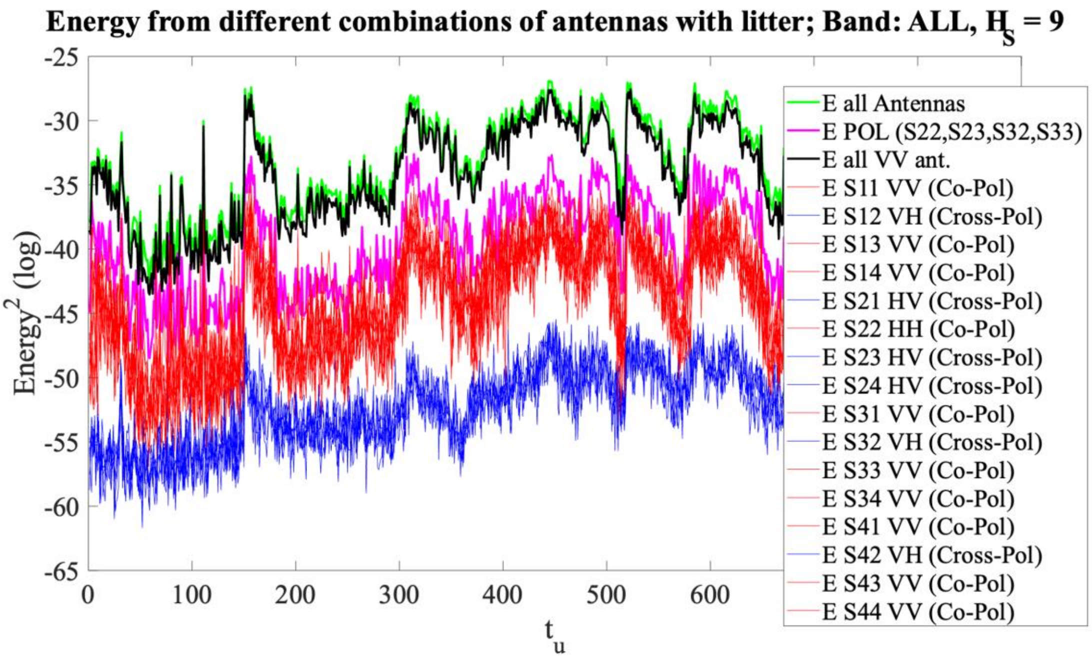

Figure 35 - Energy level comparison in the presence of litter, 5 cm PE tubes [10g/m$^2$], in logarithmic units.

Similarly, to the previous energy analysis is possible to make an overview at the EnR coefficients. Also, the coefficients that are useful for the analysis taking place in Section 4.3.1 are, from now, highlighted as the colours there in use.

| | EnR different antennas configurations 5 cm PE tubes [10g/m2], H_s= 9 cm | | | | | | | | | | | | | | | | | | | |
|---|---|---|---|---|---|---|---|---|---|---|---|---|---|---|---|---|---|---|---|---|
| | S of antenna: | S11 | S12 | S13 | S14 | S21 | **S22** | **S23** | S24 | S31 | **S32** | **S33** | S34 | S41 | S42 | S43 | S44 | All | Pol | VV |
| | Polarisation: | VV | VH | VV | VV | HV | **HH** | **HV** | HV | VV | **VH** | **VV** | VV | VV | VH | VV | VV | Normalized to Na | | |
| Hs = 9 cm | S: 2 - 9 | 1.1 | 1.0 | 1.1 | 1.1 | 1.1 | 1.1 | 1.1 | 1.1 | 1.1 | 1.0 | 1.1 | 1.0 | 1.1 | 1.0 | 1.1 | 1.0 | 1.1 | 1.1 | 1.1 |
| | Cu: 4 - 6 | 2.3 | 2.0 | 2.6 | 2.5 | 2.1 | 1.6 | 2.3 | 2.1 | 2.7 | 2.2 | 2.5 | 2.6 | 2.3 | 2.2 | 2.8 | 2.1 | 2.4 | 2.0 | 2.5 |
| | Ca: 6 - 8 | 5.3 | 2.8 | 6.6 | 6.1 | 2.8 | 2.7 | 2.7 | 2.7 | 7.2 | 2.5 | 5.0 | 6.0 | 5.6 | 2.5 | 5.9 | 4.9 | 5.1 | 3.8 | 5.7 |
| | Xu: 8 - 10 | 6.6 | 5.0 | 9.0 | 9.9 | 4.5 | 5.1 | 4.6 | 4.2 | 10.0 | 4.8 | 9.0 | 11.0 | 10.1 | 4.3 | 9.8 | 6.2 | 7.9 | 6.7 | 8.8 |
| | Xa: 10 - 12 | 4.8 | 4.0 | 6.7 | 7.0 | 4.2 | 6.6 | 4.0 | 4.5 | 6.2 | 4.0 | 5.3 | 7.9 | 7.6 | 4.4 | 7.7 | 4.8 | 5.9 | 5.6 | 6.1 |
| | KUu: 12 - 15 | 5.5 | 2.6 | 6.4 | 7.3 | 2.7 | 3.9 | 2.3 | 2.8 | 6.6 | 2.5 | 4.6 | 6.9 | 7.0 | 2.9 | 6.9 | 5.5 | 5.1 | 3.8 | 6.0 |
| | KUa: 15 - 18 | 4.6 | 2.2 | 4.6 | 5.4 | 1.8 | 3.5 | 2.2 | 2.5 | 4.7 | 1.9 | 3.4 | 5.0 | 5.1 | 2.0 | 4.8 | 4.2 | 3.8 | 3.2 | 4.5 |
| | K: 18 - 20 | 2.5 | 2.0 | 3.3 | 3.4 | 2.0 | 4.3 | 2.1 | 1.7 | 3.4 | 2.0 | 2.3 | 3.5 | 3.5 | 2.1 | 3.0 | 2.6 | 2.9 | 3.1 | 2.9 |
| | X: 8 -12 | 7.5 | 5.2 | 11.4 | 11.5 | 4.8 | 6.5 | 5.4 | 4.8 | 10.3 | 4.8 | 9.1 | 11.7 | 10.2 | 4.8 | 12.0 | 7.1 | 8.7 | 7.3 | 9.7 |
| | ALL: 2 - 20 | 6.5 | 3.8 | 8.6 | 8.6 | 3.8 | 5.4 | 3.7 | 3.8 | 8.5 | 3.7 | 6.9 | 9.0 | 8.2 | 3.9 | 9.0 | 6.4 | 6.9 | 5.8 | 7.8 |
| Hs = 17 cm | S: 2 - 9 | 1.0 | 1.0 | 1.1 | 0.9 | 1.0 | 1.1 | 1.1 | 1.0 | 1.0 | 1.1 | 1.0 | 1.1 | 1.1 | 1.1 | 1.1 | 1.0 | 1.0 | 1.1 | 1.0 |
| | Cu: 4 - 6 | 1.7 | 1.7 | 1.6 | 1.5 | 1.5 | 1.6 | 1.6 | 1.5 | 1.7 | 1.7 | 1.7 | 1.6 | 1.7 | 1.6 | 1.9 | 1.5 | 1.6 | 1.7 | 1.7 |
| | Ca: 6 - 8 | 3.7 | 2.6 | 4.4 | 4.4 | 2.2 | 2.4 | 2.2 | 2.2 | 4.9 | 2.4 | 4.2 | 4.5 | 4.7 | 2.6 | 4.8 | 3.0 | 3.8 | 3.2 | 4.2 |
| | Xu: 8 - 10 | 4.6 | 3.8 | 6.3 | 6.6 | 3.9 | 4.1 | 3.7 | 4.0 | 6.3 | 3.8 | 5.4 | 6.1 | 6.6 | 3.8 | 6.2 | 4.6 | 5.3 | 4.6 | 5.7 |
| | Xa: 10 - 12 | 4.0 | 3.7 | 4.7 | 5.2 | 3.8 | 5.1 | 3.2 | 3.5 | 5.7 | 3.9 | 3.7 | 5.4 | 5.4 | 3.7 | 5.1 | 3.6 | 4.5 | 4.2 | 4.6 |
| | KUu: 12 - 15 | 4.2 | 2.9 | 4.7 | 6.2 | 2.7 | 3.6 | 1.9 | 2.7 | 5.9 | 2.3 | 3.1 | 5.1 | 6.1 | 3.1 | 5.3 | 4.5 | 4.2 | 3.1 | 4.7 |
| | KUa: 15 - 18 | 2.7 | 2.2 | 3.9 | 4.2 | 2.5 | 4.0 | 2.0 | 2.5 | 3.7 | 2.3 | 2.5 | 4.1 | 4.2 | 2.4 | 3.8 | 3.2 | 3.3 | 3.1 | 3.4 |
| | K: 18 - 20 | 2.2 | 2.2 | 2.6 | 2.7 | 2.2 | 3.4 | 1.8 | 2.2 | 3.0 | 1.7 | 1.8 | 2.6 | 3.0 | 2.0 | 2.6 | 2.6 | 2.5 | 2.5 | 2.5 |
| | X: 8 -12 | 4.5 | 3.9 | 6.4 | 6.3 | 4.2 | 4.8 | 4.0 | 4.3 | 6.7 | 3.7 | 5.2 | 6.7 | 7.2 | 4.0 | 6.4 | 4.4 | 5.5 | 4.8 | 5.8 |
| | ALL: 2 - 20 | 3.8 | 3.1 | 4.9 | 5.1 | 3.3 | 3.7 | 3.0 | 3.4 | 5.0 | 2.9 | 4.0 | 5.3 | 5.1 | 3.4 | 5.4 | 3.8 | 4.3 | 3.7 | 4.6 |

Table 10 - EnR values collection for floating 5 cm PE tubes [10 g/m$^2$]

In Table 10 the conclusions are in line to previous the conclusions of Table 9. Comparing both $Hs = 9\ cm$ and $Hs = 17\ cm$, the lower water height, $Hs = 9\ cm$ delivers higher EnR results. The highest EnR values are in VV polarisation and in band X. The sub band Xu also has solid results, highlighting the $S_{34}$, the S parameter with best performance in terms of EnR.

The following figures of the waterfalls are some examples of the performed tests. Figure 36 is the sum of all antennas, $I_{ALL}^{litter}(d,t)$ in one of its best performed sub bans, band Xu, for $Hs = 9\ cm$. Figure 37 is a waterfall of all VV antennas, $I_{ALL_{VV}}^{litter}(d,t)$ in band Xu. Figure 38 is the waterfall of $S_{34}$, $I_{34}^{litter}(d,t)$ in band Xu, for $Hs = 9\ cm$.

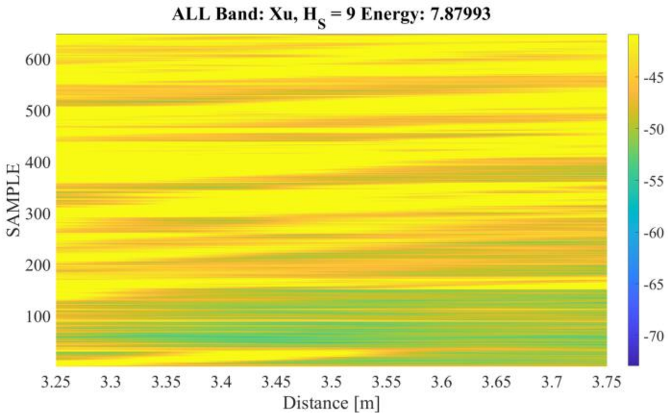

Figure 36 – $I_{ALL}^{litter}(d,t)$ backscatter in the presence of floating 5 cm PE tubes [10 g/m$^2$], $H_s = 9\ cm$.

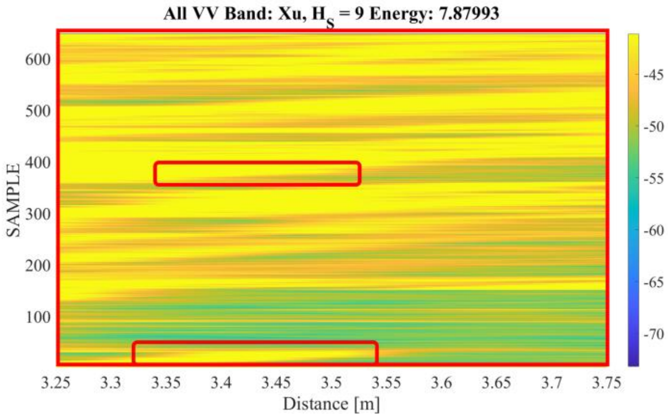

Figure 37 - $I_{ALL_{VV}}^{litter}(d,t)$ backscatter in the presence of floating 5 cm PE tubes [10 g/m$^2$], $H_s = 9\ cm$.[11]

---

[11] Red highlighted zones for further reference on an analysis in Section 4.3.

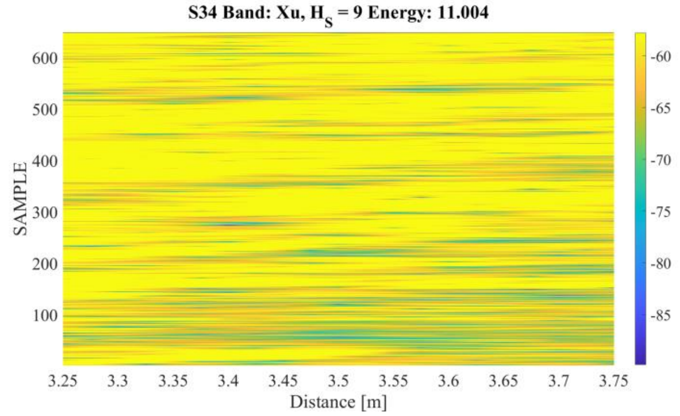

Figure 38 – $I_{34}^{litter}(d,t)$ backscatter in the presence of floating 5 cm PE tubes [10 g/m$^2$], $H_s = 9\ cm$.

Summing all antennas does not show a significant increase in the EnR metric as the EnR acquired by this method is lower than some EnR of some S matrixes. A possible explanation is that in the process of adding S parameters, not only the well performed parameters are added, but also those which EnR is lower. The same goes with the VV configuration. $I_{ALL_{VV}}^{litter}(d,t)$ performs better than $I_{ALL}^{litter}(d,t)$ configuration but it is still worse than some VV coefficients included into that configuration such as the $I_{34}^{litter}(d,t)$.

## 4.3. POLARIMETRIC ANALYSIS

As mentioned earlier, the setup in the Netherlands offers a broad range of analysis opportunities due to the extensive variety of available antenna configurations. In this section concerns two distinct polarisation analysis, leading to different results. First, in Topic 4.3.1 a polarisation analysis using a linear basis, as described in Topic 2.5.1. Secondly, in Topic 4.3.2 an approach using the Pauli decomposition is addressed, as described in Topic 2.5.2.

The S parameters at use in the following topics are all from the same device, the QRH20E antenna, as mentioned in Section 4.1. In Table 8, $S_{22}$ corresponds to HH, $S_{23}$ to HV, $S_{32}$ to VH and $S_{33}$ to VV. In this section was decided to display the results in the Xu band due to its relevance in Section 4.2 and still is one of the narrower bands presented.

### 4.3.1. LINEAR DECOMPOSITION

The first analysis regarding different polarimetry is a linear analysis which was presented previously in Topic 2.5.1. The colours are associated to each state were also defined in that topic.

The waterfalls images regard each polarisation state, created from $I_{\mathrm{VV}}^{litter}(d,t)$, $I_{\mathrm{HV+VH}}^{litter}(d,t)$, and $I_{\mathrm{HH}}^{litter}(d,t)$. To better quantify the dominance of each coefficient in the final RGB image, a histogram was added. In Table 9 and in Table 10 the coefficients' energy and EnR were previously highlighted with the RGB colour they represent in Figure 39, to facilitate its interpretation.

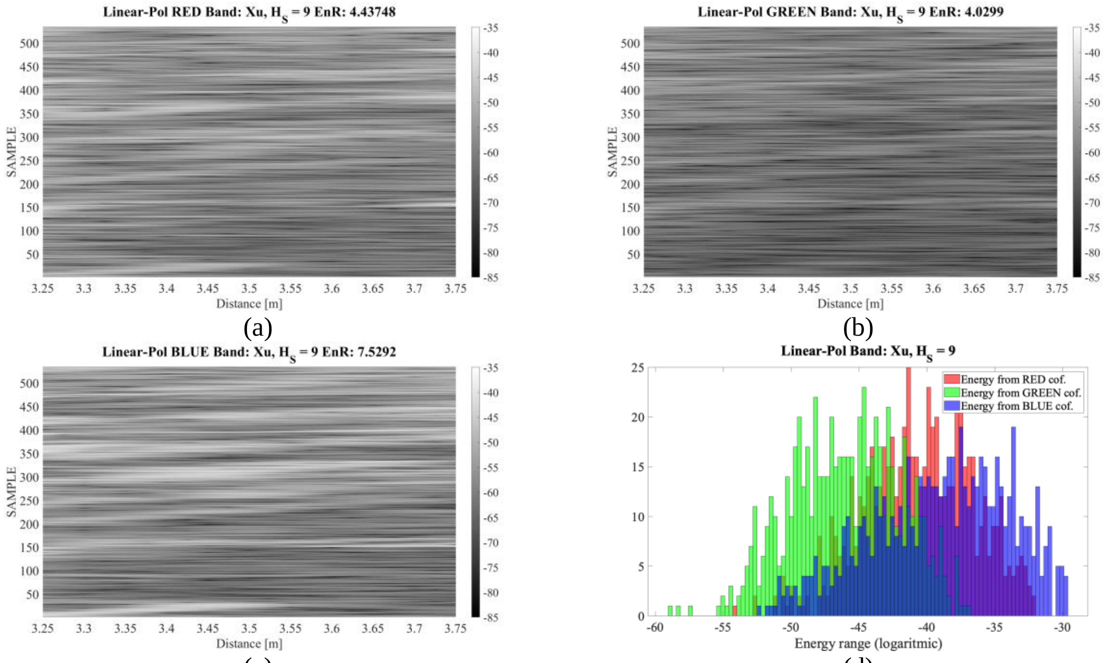

(a) (b) (c) (d)

Figure 39 – Linear decomposition of the polarisation in RGB in the presence of floating 5 cm PE tubes [10 g/m²], $H_s = 9\ cm$. (a) Red linear coefficient (HH) $I_{\mathrm{VV}}^{litter}(d,t)$; (b) Green linear coefficient (HV and VH) $I_{\mathrm{HV+VH}}^{litter}(d,t)$; (c) Blue linear coefficient (VV) $I_{\mathrm{HH}}^{litter}(d,t)$; (d) Predominance of each coefficient.

In Figure 39 the predominant coefficient in terms of energy in the blue coefficient, which was previously connected to the VV polarization state. This conclusion is in line to the previous mentioned in Section 4.2. The same happens in Figure 41 where $H_s = 17\ cm$.

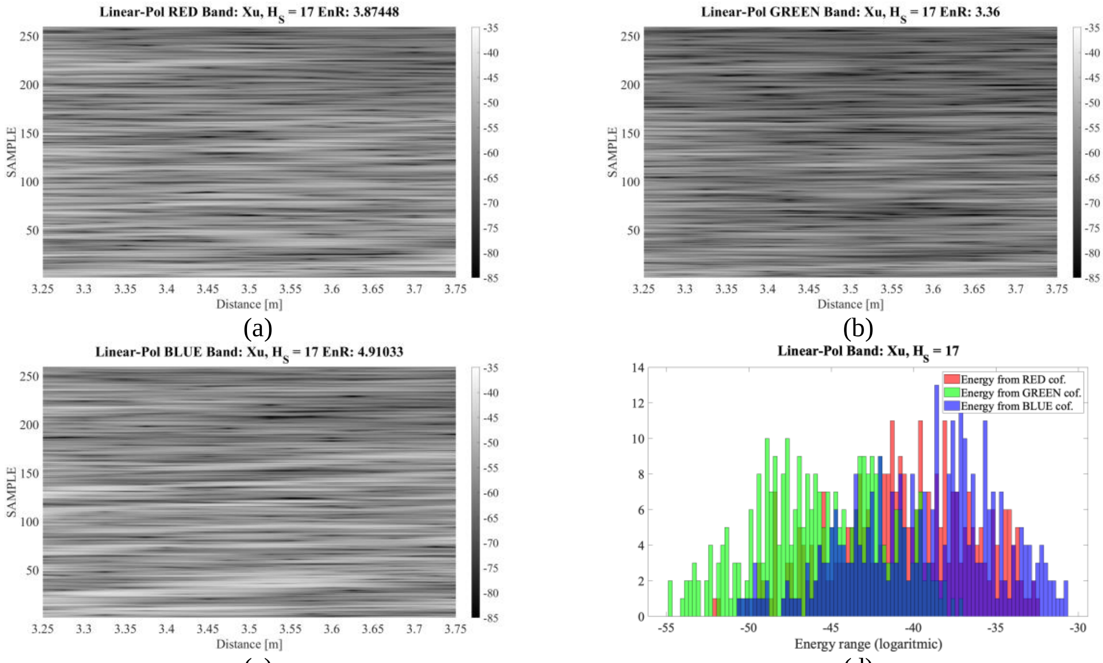

(a) (b) (c) (d)

Figure 40 – Linear decomposition of the polarisation in RGB in the presence of floating 5 cm PE tubes [10 g/m²], $H_s = 9\ cm$. (a) Red linear coefficient (HH) $I_{\mathrm{VV}}^{litter}(d,t)$; (b) Green linear coefficient (HV and VH) $I_{\mathrm{HV+VH}}^{litter}(d,t)$; (c) Blue linear coefficient (VV) $I_{\mathrm{HH}}^{litter}(d,t)$; (d) Predominance of each coefficient.

Figure 41 is created by the overlap of individual polarizations waterfalls which contain $I_{\mathrm{VV}}^{litter}(d,t)$, $I_{\mathrm{HV+VH}}^{litter}(d,t)$, and $I_{\mathrm{HH}}^{litter}(d,t)$. The distinction between litter and its absence is not clear. It is therefore more confusing than waterfalls which just contain a single polarisation. In some zones of Figure 41 the waterfall is whitish, meaning all colours of the RGB spectrum are at its maximum bright. Some of those zones were highlighted in red and match with the ones with litter, also highlighted in Figure 37. In darker areas of the figure, the predominance of each polarization coefficient is weaker.

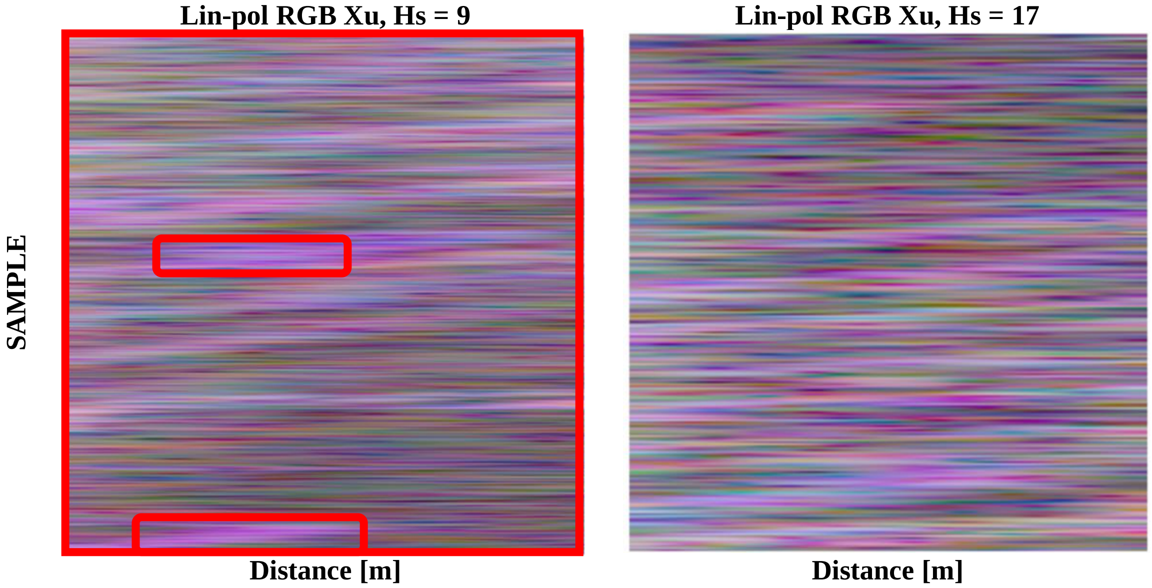

(a) (b)

Figure 41 - Linear decomposition of the polarisation in RGB in the presence of floating 5 cm PE tubes [10 g/m2]. (a) for $H_s = 9\ cm$ and (b) for $H_s = 17\ cm$

### 4.3.2. PAULI DECOMPOSITION

Besides the linear decomposition previously discussed, an alternative use for the polarimetry data is to decompose it in a Pauli basis as presented in Topic 2.5.2. The colours of each Pauli coefficient were defined in that topic along with the coefficients themselves. The S parameters in use to create the Pauli basis $\{\boldsymbol{S_a}, \boldsymbol{S_b}, \boldsymbol{S_c}\}$ are all from the same device, the QRH20E antenna.

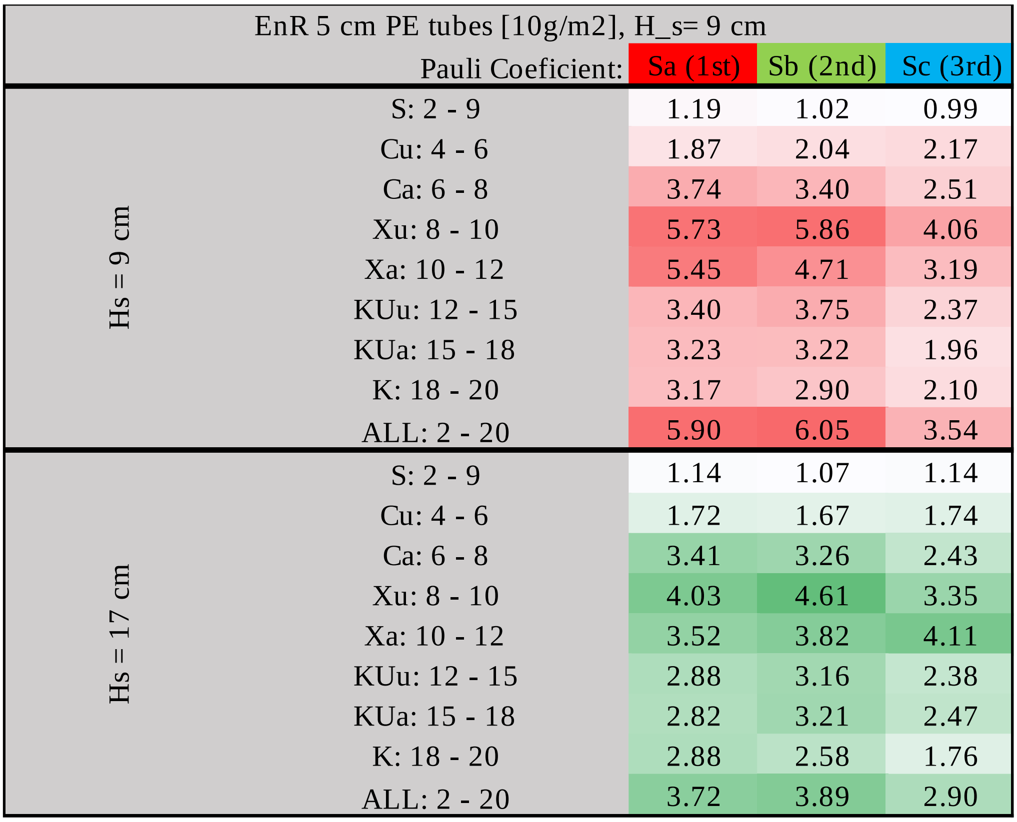

| EnR 5 cm PE tubes [10g/m2], H_s= 9 cm | | | | |
|---|---|---|---|---|
| | Pauli Coeficient: | Sa (1st) | Sb (2nd) | Sc (3rd) |
| Hs = 9 cm | S: 2 - 9 | 1.19 | 1.02 | 0.99 |
| | Cu: 4 - 6 | 1.87 | 2.04 | 2.17 |
| | Ca: 6 - 8 | 3.74 | 3.40 | 2.51 |
| | Xu: 8 - 10 | 5.73 | 5.86 | 4.06 |
| | Xa: 10 - 12 | 5.45 | 4.71 | 3.19 |
| | KUu: 12 - 15 | 3.40 | 3.75 | 2.37 |
| | KUa: 15 - 18 | 3.23 | 3.22 | 1.96 |
| | K: 18 - 20 | 3.17 | 2.90 | 2.10 |
| | ALL: 2 - 20 | 5.90 | 6.05 | 3.54 |
| Hs = 17 cm | S: 2 - 9 | 1.14 | 1.07 | 1.14 |
| | Cu: 4 - 6 | 1.72 | 1.67 | 1.74 |
| | Ca: 6 - 8 | 3.41 | 3.26 | 2.43 |
| | Xu: 8 - 10 | 4.03 | 4.61 | 3.35 |
| | Xa: 10 - 12 | 3.52 | 3.82 | 4.11 |
| | KUu: 12 - 15 | 2.88 | 3.16 | 2.38 |
| | KUa: 15 - 18 | 2.82 | 3.21 | 2.47 |
| | K: 18 - 20 | 2.88 | 2.58 | 1.76 |
| | ALL: 2 - 20 | 3.72 | 3.89 | 2.90 |

Table 11 - Pauli decomposition's EnR values collection for floating 5 cm PE tubes [10 g/m$^2$]

Similarly, to tables presented previously, Table 11 contain the EnR values for each Pauli basis coefficient. In Table 11 the second Pauli coefficient, $\boldsymbol{S_b}$ stands out from its counterparts, which mean that the double bounce scattering is predominant. A corner effect caused by the bottles' indentation on the water might be linked to that phenomenon. Also, with an increase of the water heigh $H_s = 17\ cm$, all the coefficients maintain its proportion between themselves, despite all reducing the EnR while compared to lower water level of $H_s = 9\ cm$.

Figure 42 contains the results of a waterfall analysis of each of the Pauli's coefficients for $H_s = 9\ cm$. A histogram was added to better quantify the dominance of each coefficient. Figure 43 contains the same type of information for $H_s = 17\ cm$.

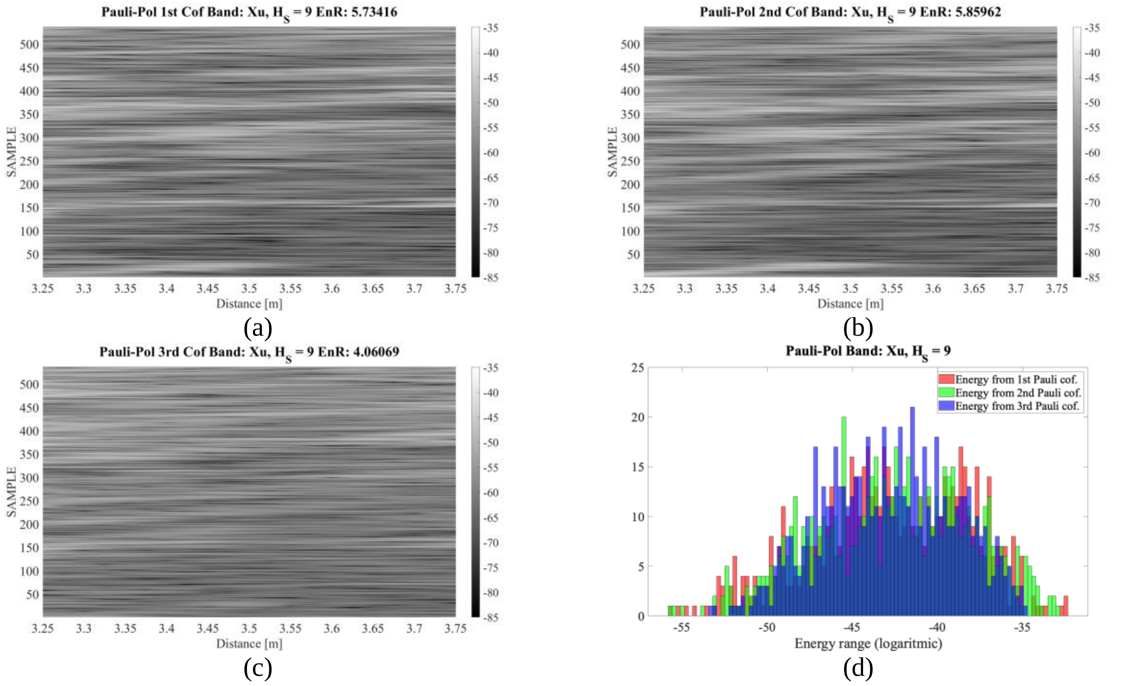

(a) (b) (c) (d)

Figure 42 – Pauli decomposition of the polarisation in RGB in the presence of floating 5 cm PE tubes [10 g/m2], $H_s = 9\ cm$. (a) Red Pauli coefficient (first Pauli coefficient, $\boldsymbol{S_a}$), $I_{\mathrm{S_a}}^{litter}(d,t)$; (b) Green Pauli coefficient (second Pauli coefficient, $\boldsymbol{S_b}$), $I_{\mathrm{S_b}}^{litter}(d,t)$; (c) Blue Pauli coefficient (third Pauli coefficient, $\boldsymbol{S_c}$), $I_{\mathrm{S_c}}^{litter}(d,t)$; (d) Predominance of each coefficient.

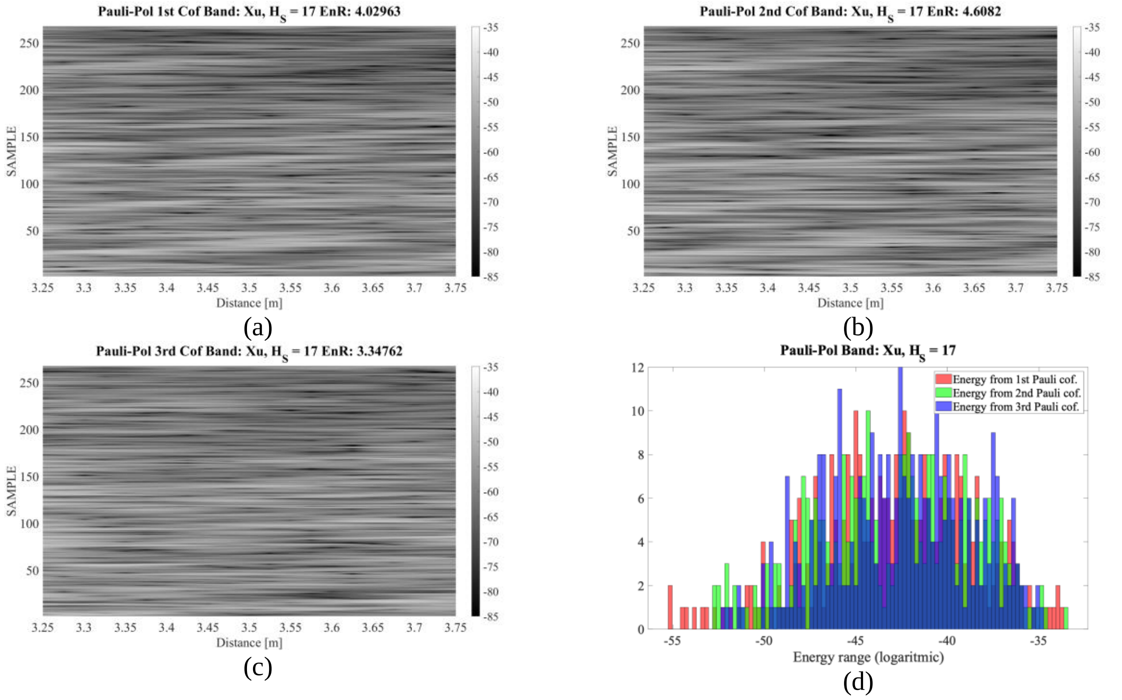

(a) (b) (c) (d)

Figure 43 – Pauli decomposition of the polarisation in RGB in the presence of floating 5 cm PE tubes [10 g/m2], $H_s = 17\ cm$. (a) Red Pauli coefficient (first Pauli coefficient, $\boldsymbol{S_a}$), $I_{\mathrm{S_a}}^{litter}(d,t)$; (b) Green Pauli coefficient (second Pauli coefficient, $\boldsymbol{S_b}$), $I_{\mathrm{S_b}}^{litter}(d,t)$; (c) Blue Pauli coefficient (third Pauli coefficient, $\boldsymbol{S_c}$), $I_{\mathrm{S_c}}^{litter}(d,t)$; (d) Predominance of each coefficient.

The following Figure 44 overlaps each RGB coloured coefficients into a single waterfall, for $H_s = 9\ cm$ and for $H_s = 17\ cm$. In that figure is possible to see whitish zones. The highlighted examples in red appear to be close to those previous identified in Figure 37 waterfall. In the whitish zones all the scattering mechanisms are present in their maximum intensity.

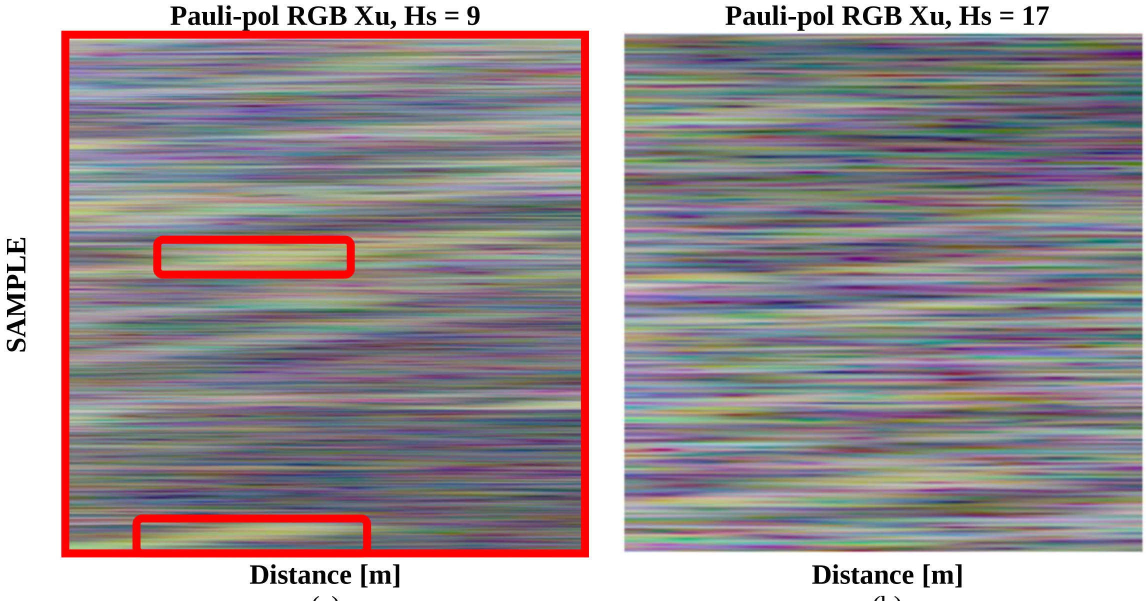

(a)

(b)

Figure 44 - Pauli decomposition of the polarisation in RGB in the presence of floating 5 cm PE tubes [10 g/m2]. (a) for $H_s = 9\ cm$ and (b) for $H_s = 17\ cm$

To characterize the scattering mechanism behaviour through Pauli Analysis, a set of histograms were created, with the energy levels of each coefficient. Various distributions were tried, however the one displayed in Figure 45 and in Figure 46 fitted the best, the Burr Type XII Distribution, which was introduced in Section 2.6. The distributions were therefore applied to logarithmic values and normalized to the median of its energy with litter. The displayed functions are a numeric fitting of the PDF and CDF. The PDF provides a relative likelihood that the value of the random variable would be equal to that sample, while the CDF is the probability that a real-valued random variable will take a value less than or equal to value where are evaluated. These functions are used to characterize the radar cross section of targets or the received power in mobile communications. These plots are useful because they show that the scattered energy increases when the litter is floating, as the median value is larger for this case.

Table 12 contains the parameters from the distribution over the Pauli's coefficients, $c$ and $k$ are the shape parameters and α is the scale parameter.

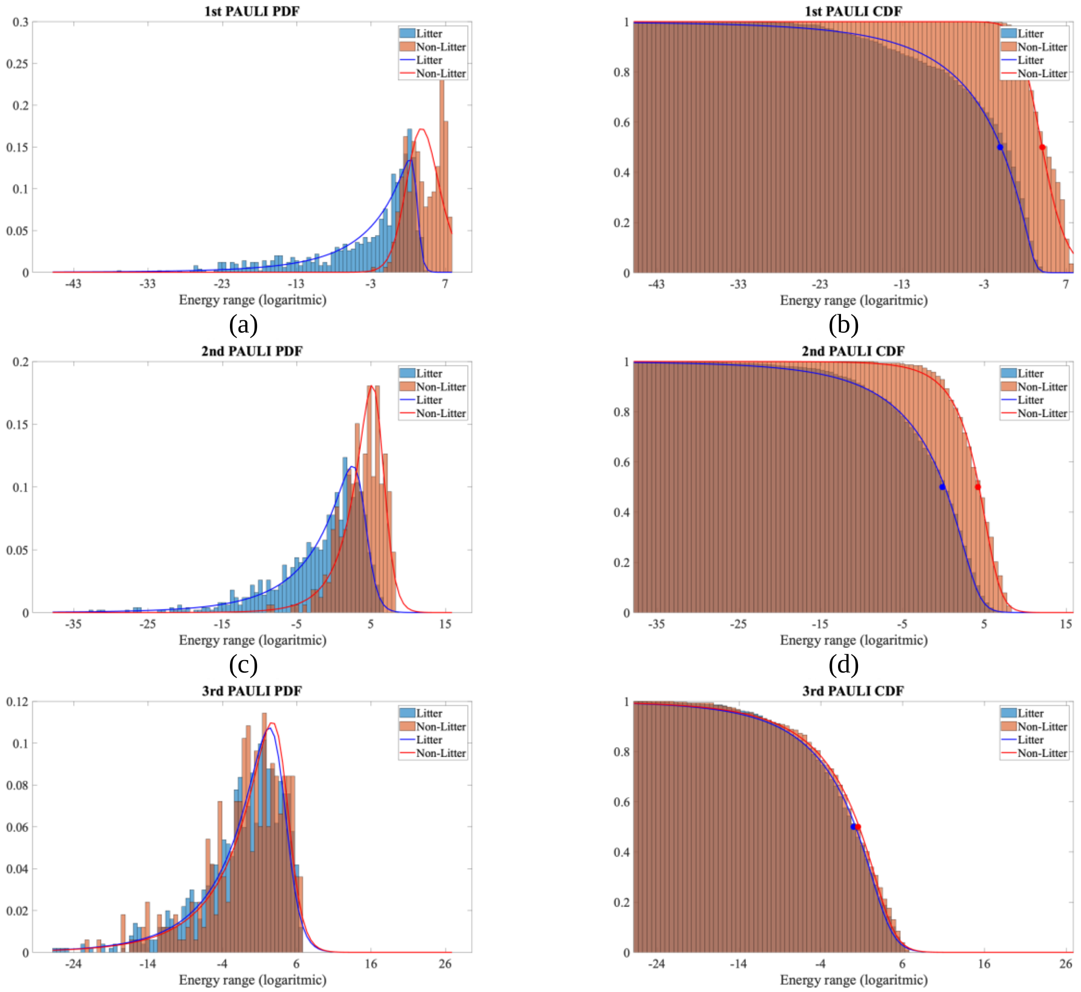

(a) (b)

(c) (d)

(e) (f)

Figure 45 – Burr Type XII Distribution applied to the Pauli decomposition data in the presence of floating 5 cm PE tubes [10 g/m2], $H_s = 9\ cm$. (a) Burr Type XII PDF applied to Pauli first coefficient; (b) Burr Type XII CDF applied to Pauli first coefficient; (c) Burr Type XII PDF applied to Pauli second coefficient; (d) Burr Type XII CDF applied to Pauli second coefficient; (e) Burr Type XII PDF applied to Pauli third coefficient; (f) Burr Type XII CDF applied to Pauli third coefficient. Histograms are normalized to the median of the correspondent Pauli coefficient with litter.

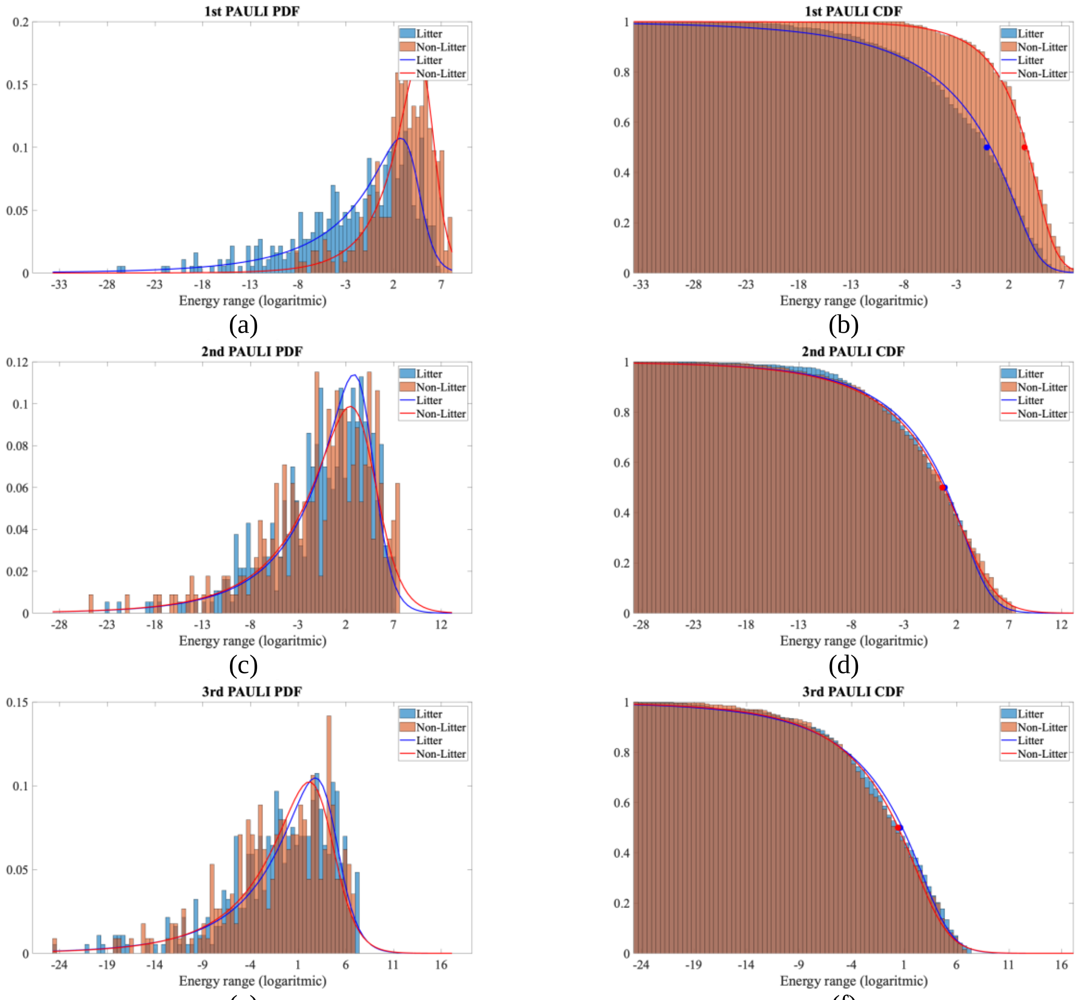

(a) (b) (c) (d) (e) (f)

Figure 46 – Burr Type XII Distribution applied to the Pauli decomposition data in the presence of floating 5 cm PE tubes [10 g/m2], $H_s = 17\ cm$. (a) Burr Type XII PDF applied to Pauli first coefficient; (b) Burr Type XII CDF applied to Pauli first coefficient; (c) Burr Type XII PDF applied to Pauli second coefficient; (d) Burr Type XII CDF applied to Pauli second coefficient; (e) Burr Type XII PDF applied to Pauli third coefficient; (f) Burr Type XII CDF applied to Pauli third coefficient. Histograms are normalized to the median of the correspondent Pauli coefficient with litter.

|  |  |  | Log-Burr Type XII Distribution |  |  |  |  |  |
|---|---|---|---|---|---|---|---|---|
| Freq. Band [GHz] | Water Height | Pauli Coeficient | Alpha_Litter | Alpha_NonLitter | C_Litter | C_NonLitter | K_Litter | K_NonLitter |
| Xu: 8 - 10 | Hs = 9 cm | 1st Pauli-cof. | 33.8 | 35.1 | 96.4 | 18.5 | 0.1 | 2.6 |
|  |  | 2nd Pauli-cof. | 41.1 | 39.0 | 50.2 | 45.6 | 0.2 | 0.3 |
|  |  | 3rd Pauli-cof. | 52.1 | 51.7 | 47.6 | 48.8 | 0.2 | 0.2 |
|  | Hs = 9 cm | 1st Pauli-cof. | 42.7 | 41.4 | 47.4 | 48.9 | 0.2 | 0.3 |
|  |  | 2nd Pauli-cof. | 47.7 | 48.0 | 45.0 | 32.4 | 0.2 | 0.3 |
|  |  | 3rd Pauli-cof. | 51.6 | 52.3 | 43.4 | 38.1 | 0.2 | 0.3 |

Table 12 - Logarithmic Burr parameters

# 5. CONCLUSIONS

The intent of this chapter is to summarize the document into final conclusions. Also, to define possible future work paths following this thesis.

## 5.1. A SUMMARY OF THE CONCLUSIONS

This thesis main objective was to improve litter detection on water, what was fulfilled by the caried analysis which enhanced the comprehension of phenomena under study. Therefore, based on the insights from this chapter, techniques can evolve, and investigation proceed.

Chapter 3 shows that, with a Bragg peak in the frequency band of analysis, is still possible to detect litter. However, the EnR appears to behave in a contrary manner when compared to a situation without Bragg interference. A concentration increase tends to reduce the EnR. Under Bragg, the PR appears to have a relation to the concentration at play, however not clear enough to have a direct impact on litter detection, at least with the tools used so far. The azimuth angle $\varphi$ also influence $f_{Bragg}$, which is not contemplated in equitation [1]. The increasement of $\varphi$, also increased the frequency of constructive interference, $f_{Bragg}$, and reduced the energy of the measurement significantly. Simulations on a wider JONSWAP model were also performed, which is a situation more close to the desired scenario of an antennas placed on an aircraft or on a satellite.

Chapter 4 addresses the question, if combining multiple antennas will improve detection, which does not, as the quality will always be reduced by the worst performer combined antenna. Also, expanding the analyses for multi polarimetry does not improve results. However, the Pauli analysis conclusions are useful to identify the bounce number of a simulation. The Pauli analysis also pointed that double bounce is predominant to other scattering mechanisms in the performed simulations.

The results from both Chapter 3 and Chapter 4 also point that litter detection is generally enhanced in the X-band.

## 5.2. FUTURE WORK

This thesis is a small contribution to project “MARES” which started when the problem was addressed by first time, two years ago in a master thesis (Figueira, 2021). The matters here addressed are far from finished, and with more research, simulation and outdoor campaigns, they can be insighted.

In Chapter 3 JONSWAP under the Bragg effect simulations were not performed successfully, mostly due to hardware and software simulations, but different attempts with the CST and SeaGen may lead to the completion of that task. Also, JONSWAP simulations can be performed on more realistic scenarios, with the wave spectrum varying, not only across the $x$ axis, but also across $y$ axis, which SeaGen is already capable of. SeaGen is also capable of performing results in more than a single polarimetry state. The polarimetric analysis from Chapter 4 can be extended to CST simulations, with and without the Bragg effect under lager JONSWAP realistic models. It may be relevant to also perform SAR tests to explore techniques as the reduction of the peak relation to the concentration analyzed in Section 3.3

Outdoor measurement campaigns on larger areas, with a drone or an aircraft, would also be a significative contribution since allows a scenario closer to the desired satellite-based measurements. Satellite data can also be processed and therefore analyzed, which requires time-based ground truth, a challenge not easy to overcome. Also, besides macro plastics, microplastics can be measured and analyzed.

# REFERENCES

Autoridade Marítima Nacional. (2023). *Direção de Combate à Poluição do Mar, Missão e Competências*. Retrieved August 2023, from Autoridade Marítima Nacional: https://www.amn.pt/DCPM/Paginas/Missao.aspx

Biermann, L., Clewley, D., Martinez-Vicente, V., & Topouzelis, K. (2020). *Finding Plastic Patches in Coastal Waters using Optical Satellite Data.* Springer Nature. doi:10:5364

Boerner, W.-M. (2004). *Basics of SAR Polarimetry.* Brussels: NATO STO.

Borrelle, S. B., Ringma, J., Law, K. L., Monnahan, C. C., Lebreton, L., McGivern, A., . . . Gerber, L. (2020). Predicted growth in plastic waste exceeds efforts to mitigate plastic pollution. *Science, 369*(1515). doi:10.1126/science.aba3656

Boyle, L. (2023, April 19). The Great Pacific Garbage Patch is so large that tiny creatures are making it home. *The Independent*. Retrieved from https://www.independent.co.uk/climate-change/news/pacific-ocean-garbage-patch-plastic-b2321349.html

Bragg, W. L., Bragg, W. H., & Wolff, C. (1912). *Bragg-Scattering*. Retrieved April 27, 2023, from www.radartutorial.eu: https://www.radartutorial.eu/07.waves/wa52.en.html

Burr, I. W. (1942). Cumulative Frequency Functions. *The Annals of Mathematical Statistics, vol. 13*(no. 2), pp. 215–32.

Cassidy, E. (2021, December 3). Tracking Ocean Plastic From Space. *Earth Data, NASA*. Retrieved from https://www.earthdata.nasa.gov/learn/articles/ocean-plastic

Chaturvedi, S. K., Banerjee, S., & Lele, S. (2019). *An assessment of oil spill detection using Sentinel 1 SAR-C images.* Elsevier. doi:https://doi.org/10.1016/j.joes.2019.09.004

Copper Mountain Technologies. (2022, April). C4420 4-Port 20 GHz Analyzer Frequency Extension Compatible. Retrieved from https://coppermountaintech.com/vna/c4420-cobalt-4-port-vna/

Costa, T. S., Felício, J. M., Vala, M., Leonor, N., Costa, J. R., Marques, P., . . . de Maagt, P. (2023). *Detection of Low Permittivity Floating Plastic Sheets at Microwave Frequencies.* European Conference on Antennas and Propagation (EuCAP). IEEE Xplore.

Costa, T. S., Felício, M. J., Matos, S. A., & Fernandes, C. A. (2023). *Emulating Macroplastic Litter Detection Scenarios using SeaGEN: a Hybrid PO-GO Backscattering Simulation Tool.* (awaiting for submission).

Dalponte, M., Bruzzone, L., & Gianelle, D. (2012). *Remote Sensing of Environment.* Elsevier.

Dassault Systèmes. (2002 - 2023). CST STUDIO SUITE. Retrieved from https://www.3ds.com/products-services/simulia/products/cst-studio-suite/

Delft. (2022, December). DELTARES Wave Facility. Atlantic Basin, Delft, Netherlands. Retrieved from https://www.deltares.nl/en/

Earth Data, NASA. (2021, April 8). *Physical Oceanography DAAC (PO.DAAC)*. Retrieved from www.earthdata.nasa.gov: https://www.earthdata.nasa.gov/eosdis/daacs/podaac

Eguchi, R. T., Huyck, C. K., Ghosh, S., & Adams, B. J. (2008). *The Application of Remote Sensing Technologies for Disaster Management.* Beijing: The 14th World Conference on Earthquake Engineering.

ESA. (2012, June 29). *ESA Satellite Missions Catalogue*. Retrieved from eoportal: https://www.eoportal.org/satellite-missions/prisma-hyperspectral#eop-quick-facts-section

ESA. (2020). *Detection of Ocean Litter Plastics with Hyper-to-multispectral Infrared Neural Networks (DOLPHINN)*. Retrieved from Nebula Public Library: https://nebula.esa.int/content/detection-ocean-litter-plastics-hyper-multispectral-infrared-neural-networks-dolphinn

Evans, M. C., & Ruf, C. S. (2022). *Toward the Detection and Imaging of Ocean Microplastics With a Spaceborne Radar*. IEEE. Retrieved from https://ieeexplore.ieee.org/stamp/stamp.jsp?tp=&arnumber=9449485

Evers, J. (2023, April 3). Great Pacific Garbage Patch. *National Geographic Society*. Retrieved from https://education.nationalgeographic.org/resource/great-pacific-garbage-patch/

Felício, J. M., Costa, T. S., Vala, M., Leonor, N., Costa, J. R., Marques, P., . . . de Maagt, P. (2023). *Feasibility of Radar-based Detection of Floating Macroplastics at Microwave Frequencies.* (awaiting for submission).

Figueira, B. S. (2021). *Microwave Detection and Characterization of Floating Plastic.* Instituto Superior Técnico, Lisboa.

Gade, M., Alpers, W., Ermakov, S. A., Hühnerfuss, H., & Lange, P. A. (1998). Wind-wave tank measurements of bound and freely propagating short gravity-capillary waves. *Journal of Geophysical Research, 103*(C10), 21697– 21709.

Gamarro, E. G., Ryder, J., Elvevoll, E. O., & Olsen, R. L. (2020). *Microplastics in Fish and Shellfish – A Threat to Seafood Safety?* Journal of Aquatic Food Product Technology. doi:10.1080/10498850.2020.1739793

Ge, Z., Shi, H., Mei, X., Dai, Z., & Li, D. (2016). *Semi-automatic recognition of marine debris on beaches.* Scientific Reports. doi:10.1038/srep25759

Gonga, A., Pérez-Portero, A., Camps, A., Pascual, D., de Fockert, A., & de Maagt, P. (2023). *GNSS-R Observations of Marine Plastic Litter in a Water Flume: An Experimental Study.* Remote Sensing. doi:https://doi.org/10.3390/rs15030637

Hajnsek, I., & Desnos, Y.-L. (2021). *Polarimetric Synthetic Aperture Radar - Principles and Aplication.* Springer. doi:10.1007/978-3-030-56504-6

HALL, A., LAMB, D., HOLZAPFEL, B., & LOUIS, J. (2002). *Optical remote sensing applications in viticulture – a review.* Australian Journal of Grape and Wine Research.

Haram, L. E., Carlton, J. T., Centurioni, L., Choong, H., Cornwell, B., Crowley, M., . . . Ruiz, G. M. (2023). *Extent and reproduction of coastal species on plastic debris in the North Pacific on plastic debris in the North Pacific.* Nature Ecology & Evolution. doi:https://doi.org/10.1038/s41559-023-01997-y

Hasselmann, K., Barnett, T. P., Bouws, E., Carlson, H., Cartwright, D. E., Enke, K., . . . Walden, H. (1973, January). *Measurements of wind-wave growth and swell decay during the Joint North Sea Wave Project (JONSWAP).* Deutches Hydrographisches Institut. Retrieved from http://resolver.tudelft.nl/uuid:f204e188-13b9-49d8-a6dc-4fb7c20562fc

Instituto de Telecomunicações. (2023). *IT – LISBOA.* Retrieved from www.it.pt: https://www.it.pt/ITSites/Index/1

Jambeck, J. R. (2015). *Plastic waste inputs from land into the ocean.* Science. doi:10.1126/science.1260352

Kampes, B. M. (2006). *Radar Interferometry - Persistent Scatterer Technique.* The Netherlands: Springer.

Kremezi, M., Kristollari, V., Karathanassi, V., Topouzelis, K., Kolokoussis, P., Taggio, N., . . . Corradi, P. (2022). Increasing the Sentinel-2 potential for marine plastic litter monitoring through image fusion techniques. *Marine Pollution Bulletin*(182). doi:10.1016/j.marpolbul.2022.113974

Lopez-Sanchez, J. n., & Fortuny-Guasch, J. (2000). 3-D Radar Imaging Using Range Migration Techniques. *IEEE TRANSACTIONS ON ANTENNAS AND PROPAGATION, 48*(5).

Martínez-Vicente, V., Clark, J. R., Corradi, P., Aliani, S., Arias, M., Bochow, M., . . . Goddijn-Murphy. (2019). Measuring Marine Plastic Debris from Space: Initial Assessment of Observation Requirements. *Remote Sensing.*

Martins, R. d., Felício, J. M., Matos, S. d., da Costa, J. R., & Fernandes, C. C. (2021, February). Preliminary Characterization of Microwave Backscattering of Floating Plastic. *Telecoms Conference ConfTELE, Conference Online*, pp. Vol. , pp. 1 - 4.

MathWorks. (2019/2023). MATLAB. Retrieved from www.mathworks.com

Meijer, L., Emmerik, T. V., Der Ent, R. V., Schmidt, C., & Lebreton, L. (2021). More than 1000 rivers account for 80% of global riverine plastic emissions into the ocean. *Science.* Retrieved from https://www.science.org/doi/10.1126/sciadv.aaz5803

Meissner, T., & Wentz, F. J. (2004, September). The Complex Dielectric Constant of Pure and Sea Water From Microwave Satellite Observations. *IEEE Transactions on Geoscience and Remote Sensing, 42*(9).

Munk, H. W. (1951). *Origin and Generation of Waves.* University of California. La Jolla, California: Institute of Geographysics and scripps Institution of Oceanography.

National Aeronautics and Space Administration. (2019, December 12). *CYGNSS*. Retrieved from www.nasa.gov: https://www.nasa.gov/cygnss

National Oceanic and Atmosferic Administration. (2023, January 1). *What are microplastics?* Retrieved April 17, 2023, from NOSS Ocean Service: https://oceanservice.noaa.gov/facts/microplastics.html#:~:text=Plastic%20debris%20can%20come%20in,)%20are%20called%20%E2%80%9Cmicroplastics.%E2%80%9D

National Oceanic and Atmospheric Administration. (2023). What is a gyre? *National Ocean Service*. Retrieved from https://oceanservice.noaa.gov/facts/gyre.html

NOAA. (2023, April 17). *Garbage Patches*. Retrieved April 17, 2023, from Marine Debris Program: https://marinedebris.noaa.gov/info/patch.html

OECD iLibrary. (2023). *Global Plastics Outlook.* Retrieved August 2023, from OECD iLibrary: https://www.oecd-ilibrary.org/environment/data/global-plastic-outlook_c0821f81-en

Organisation for Economic Co-operation and Development. (2022, February 22). *Plastic pollution is growing relentlessly as waste management and recycling fall short, says OECD*. Retrieved August 2023, from OECD.org: https://www.oecd.org/environment/plastic-pollution-is-growing-relentlessly-as-waste-management-and-recycling-fall-short.htm

Palombi, L., & Raimondi, V. (2022). *Experimental Tests for Fluorescence LIDAR Remote Sensing of Submerged Plastic Marine Litter.* Remote Sensing. doi:https://doi.org/10.3390/rs14235914

PlasticsEurope. (2020). *Plastics – the Facts 2020.* Brussels: PlasticsEurope. Retrieved from https://plasticseurope.org/

Pozar, D. M. (2011). *Microwave Engineering.* Wiley.

RF-SPIN. (2022, April). DRH30 Double Ridged Horn Antenna. Retrieved from https://www.rfspin.com/product/drh30/

RF-SPIN. (2022, April). QRH20E Quad Ridged Horn Antenna. Retrieved from https://www.rfspin.com/product/qrh20e/

Richards, M. A., Scheer, J. A., & Holm, W. A. (2010). *Principles of Modern Radar, Basic Principles.* Edison: SciTech Publishing.

Ritchie, H. (2021). Where does the plastic in our oceans come from? *Our World in Data*. Retrieved from https://ourworldindata.org/ocean-plastics#:~:text=Most%20of%20the%20plastic%20in,%2C%20ropes%2C%20and%20abandoned%20vessels.

Sheng, X.-Q., & Song, W. (2012). Method of Moments. *IEEE Xplore*, 29 - 151. doi:10.1002/9780470829646.ch2

Shi, D., Tang, X., & Wang, C. (2017). *The acceleration of the shooting and bouncing ray tracing method on GPUs.* Montreal, QC, Canada: IEEE. doi:10.23919/URSIGASS.2017.8105251

Shi, W., Goodchild, M. F., Batty, M., Kwan, M.-P., & Zhang, A. (2021). *Urban Informatics*. Springer.

Simpson, M. D., Marino, A., de Maagt, P., Gandini, E., de Fockert, A., Hunter, P., . . . Tyler, A. (2023). Investigating the Backscatter of Marine Plastic Litter Using a C- and X-Band Ground Radar, during a Measurement Campaign in Deltares. *Remote Sensing*.

Sun, Y., Bakker, T., Ruf, C., & Pan, Y. (2023). *Efects of microplastics and surfactants on surface roughness of water waves.* Nature Portfolio. Scientifc Reports. doi:https://doi.org/10.1038/s41598-023-29088-9

Taggio, N., Aiello, A., Ceriola, G., Kremezi, M., Kristollari, V., Kolokoussis, P., . . . Barbone, E. (2022). *A Combination of Machine Learning Algorithms for Marine.* Remote Sensing. doi:https://doi.org/10.3390/rs14153606

Takagaki, N., Komori, S., Iwano, K., Suzuki, N., & Kumamaru, H. (2018). Generation method of wind waves under long-fetch conditions over a broad range of wind speeds. *Procedia IUTAM, 26*, 184-193.

Tekman, M. B., Walther, B. A., Peter, C., Gutow, L., & Bergmann, M. (2022). *Impacts of plastic pollution in the oceans on marine.* Berlin: WWF. doi:10.5281/zenodo.5898684

Topouzelis, K., Papageorgiou, D., Karagaitanakis, A., Papakonstantinou, A., & Ballesteros, M. A. (2020). *Remote Sensing of Sea Surface Artificial Floating Plastic Targets with Sentinel-2 and Unmanned Aerial Systems (Plastic Litter Project 2019).* Basel: MDPI. doi:10.3390/rs12122013

Topouzelis, K., Papageorgiou, D., Suaria, G., & Aliani, S. (2021). Floating marine litter detection algorithms and techniques using optical remote sensing data: A review. *Marine Pollution Bulletin*(170).

Van den Bremer, T. (2022, May). *Tracing waves to find phantom plastic.* Retrieved from udelft.nl: https://www.tudelft.nl/en/ceg/research/stories-of-science/tracing-waves-to-find-phantom-plastic

Van den Bremer, T. S., & Breivik, Ø. (2017, December 11). Stokes drift. *Philosophical Transactions of the Royal Society A: Mathematical, Physical and Engineering Sciences, 376*(2111).

Werner, S., Budziak, A., van Franeker, J., Galgani, F., Hanke, G., Maes, T., & Matiddi, M. (2016). *Harm caused by Marine Litter. MSFD GES TG Marine Litter - Thematic Report.* JRC Science Hub. doi:10.2788/690366

Woodhouse, I. H. (2006). *Introduction to Microwave Remote Sensing.* The University of Edinburgh, Scotland: Taylor & Francis Group.